Innovative Utilization of Waste Heat in Enhancing Hydrogen Liquefaction Efficiency Using Heat Recovery: Comparative Analysis of ABR, DAR, and ORC/Kalina Cycles

by

Seyed Masoud BANIJAMALI

THESIS PRESENTED TO ÉCOLE DE TECHNOLOGIE SUPÉRIEURE
IN PARTIAL FULFILLMENT FOR A MASTER'S DEGREE WITH THESIS
IN RENEWABLE ENERGY AND ENERGY EFFICIENCY
M.A.Sc.

MONTREAL, OCTOBER 23, 2024

ÉCOLE DE TECHNOLOGIE SUPÉRIEURE
UNIVERSITÉ DU QUÉBEC

BOARD OF EXAMINERS (THESIS M.SC.A.)

THIS THESIS HAS BEEN EVALUATED

BY THE FOLLOWING BOARD OF EXAMINERS

Mr. Adrian Ilinca, Thesis Supervisor
Department of Mechanical Engineering at École de technologie supérieure

Mr. Ricardo Izquierdo, President of the jury
Department of Electrical Engineering at École de technologie supérieure

Mr. Daniel R. Rousse, Member of the jury
Department of Mechanical Engineering at École de technologie supérieure

THIS THESIS WAS PRESENTED AND DEFENDED

IN THE PRESENCE OF A BOARD OF EXAMINERS AND PUBLIC

OCTOBER 22, 2024

AT ÉCOLE DE TECHNOLOGIE SUPÉRIEURE

ACKNOWLEDGMENT

I want to express my sincere gratitude to all those who have contributed to the successful completion of my master's thesis.

First, I extend my heartfelt thanks to my thesis advisor, professor Ilinca, whose guidance, expertise, and support have been invaluable throughout this research journey. Your mentorship has been instrumental in shaping the direction of this thesis.

I also deeply appreciate my professors and the academic staff at École de technologie supérieure for providing a stimulating learning environment and access to valuable resources that enriched my academic experience.

Finally, I thank my family for their unconditional support and endless love. I want to extend my gratitude to my mother (Fatemeh) and father (Sadegh). Despite being away from you while I was studying at École de technologie supérieure, I have always felt your spiritual support and encouragement in my life. I am also pleased to thank my brothers, Majid and Vahid, who have supported me during difficult times and significantly contributed to my success.

UTILISATION INNOVANTE DE LA CHALEUR RÉSIDUELLE POUR AMÉLIORER L'EFFICACITÉ DE LA LIQUÉFACTION DE L'HYDROGÈNE À L'AIDE DE LA RÉCUPÉRATION DE CHALEUR : ANALYSE COMPARATIVE DES CYCLES ABR, DAR ET ORC/KALINA

Seyed Masoud BANIJAMALI

RÉSUMÉ

Diverses méthodes ont été proposées et développées pour réduire l'énergie nécessaire à la liquéfaction de l'hydrogène et améliorer son efficacité thermodynamique et exergétique. Une stratégie efficace consiste à utiliser la chaleur résiduelle des centrales électriques. Cette thèse examine trois scénarios novateurs pour utiliser 2 MW de chaleur excédentaire dans un cycle de liquéfaction de l'hydrogène. Le premier scénario intègre un cycle de réfrigération par absorption à eau-ammoniac (ABR) pour absorber la chaleur résiduelle et fournir une partie du prérefroidissement nécessaire. Le deuxième scénario dirige la chaleur résiduelle vers un cycle de réfrigération par diffusion-absorption (DAR) pour aider au prérefroidissement de l'hydrogène. Le troisième scénario utilise une combinaison de cycle de Rankine organique (ORC) et de cycle Kalina pour convertir la chaleur résiduelle en énergie électrique, complétant ainsi l'énergie nécessaire à la liquéfaction. Les simulations énergétiques ont révélé que le scénario basé sur l'ORC/Kalina atteignait la plus faible consommation d'énergie spécifique à 4.306 kWh/kg LH_2, surpassant légèrement les scénarios basés sur DAR et ABR. Tous les scénarios ont montré des coefficients de performance améliorés, environ 2% plus élevés que la base de référence et significativement meilleurs que les valeurs de référence. L'analyse du pincement a démontré une haute performance dans tous les scénarios, avec des différences de températures minimales entre les courbes chaudes et froides, indiquant une utilisation efficace de l'énergie. L'analyse exergétique a identifié les échangeurs de chaleur comme les principaux contributeurs à la destruction d'exergie, représentant près de la moitié du total dans chaque scénario. Le cycle basé sur ABR a présenté la plus haute efficacité exergétique totale à 52.47%, tandis que le scénario basé sur ORC/Kalina a montré la plus haute efficacité exergétique pour le processus de prérefroidissement de l'H_2 à 70.84% et la plus faible destruction exergétique globale. Ces résultats soulignent le potentiel d'intégration des systèmes de récupération de chaleur résiduelle pour améliorer l'efficacité de la liquéfaction de l'hydrogène.

Mots-clés : Liquéfaction de l'hydrogène, Cycle de réfrigération par absorption eau-ammoniac, Cycle de Rankine organique, Cycle de puissance Kalina, Cycle de réfrigération par diffusion-absorption

INNOVATIVE UTILIZATION OF WASTE HEAT IN ENHANCING HYDROGEN LIQUEFACTION EFFICIENCY USING HEAT RECOVERY: COMPARATIVE ANALYSIS OF ABR, DAR, AND ORC/KALINA CYCLES

Seyed Masoud BANIJAMALI

ABSTRACT

Various methods have been proposed and developed to reduce the energy required for hydrogen liquefaction and improve its thermodynamic and exergy efficiency. One effective strategy involves utilizing waste heat from power plants. This thesis investigates three novel scenarios for using 2000 kilowatts of excess heat in a hydrogen liquefaction cycle. The first scenario integrates an Ammonia-Water Absorption Refrigeration (ABR) Cycle to absorb waste heat and provide part of the required precooling. The second scenario directs waste heat to a Diffusion-Absorption Refrigeration (DAR) Cycle to aid hydrogen precooling. The third scenario employs a combination of Organic Rankine Cycle (ORC) and Kalina Cycle to convert waste heat into electrical power, supplementing the energy needed for liquefaction. Energy simulations revealed that the ORC/Kalina-based scenario achieved the lowest specific power consumption at 4.306 kWh/kg LH_2, slightly outperforming the DAR-based and ABR-based scenarios. All scenarios showed improved coefficients of performance, approximately 2% higher than the baseline and significantly better than reference values. Pinch analysis demonstrated high performance across all scenarios, with minimal temperature differences between hot and cold curves, indicating efficient energy utilization. Exergy analysis identified heat exchangers as the primary contributors to exergy destruction, accounting for nearly half of the total in each scenario. The ABR-based cycle exhibited the highest total exergy efficiency at 52.47%. The ORC/Kalina-based scenario showed the highest exergy efficiency for the H_2 pre-cooling process at 70.84% and the lowest overall exergy destruction. These findings underscore the potential of integrating waste heat recovery systems to enhance hydrogen liquefaction efficiency.

Keywords: Hydrogen liquefaction, Ammonia-Water Absorption Refrigeration Cycle, Organic Rankine Cycle, Kalina Power Cycle, Diffusion-Absorption Refrigeration Cycle

TABLE OF CONTENTS

Page

LIST OF TABLES

Page

LIST OF FIGURES

LIST OF ABREVIATIONS

ABR	Absorption Refrigeration
ACC	Absorption Cooling Cycle
BFD	Block Flow Diagram
CC	Composite Curve
COP	Coefficient of Performance
DAR	Diffusion-Absorption Refrigeration
FT	Fischer-Tropsch
IBOG	Inevitable Boil-Off Gas
IPCC	Intergovernmental Panel on Climate Change
KC	Kalina Cycle
L−H	Lindee Hampson
LHV	Lower Heating Value
LNG	Liquefied Natural Gas
LOHCs	Liquid Organic Hydrogen Carriers
LPG	Liquefied Petroleum Gas
MHs	Metal Hybrids
MR	Mixture of Refrigerants
MRC	Mixed Refrigerant Cycle
NG	Natural Gas
ORC	Organic Rankine Cycle
SEC	Specific Energy Consumption
SMR	Single Mixed Refrigeration

TPD	Tons Per Day
US DoE	U.S. Department of Energy

LIST OF SYMBOLS

γ_i	Activity coefficient of the ith component
NH3	Ammonia
CO_2	Carbon dioxide
CO	Carbon monoxide
cP	Centipoise
C	Compressor
°C	Degrees Celsius
DT	Distillation tower
$/h	Dollar per hour
D	Drum
eV	Electron volt
Z	Elevation from a reference position
H	Enthalpy
S	Entropy
Ex	Exergy
ΔG	Gibbs free energy alteration
g/mol	Grams per mole
g	Gravitational acceleration
Q	Heat
HX	Heat exchanger
H_2	Hydrogen
I	Irreversibility or exergy destruction

K	Kelvin
Kg	Kilogram
Kg/m3	Kilograms per cubic meter
kg/s	Kilograms per second
kJ/kg	Kilojoules per kilogram
kW	Kilowatt
kW/kg LH2	Kilowatt per kilogram of liquid hydrogen
kWh	Kilowatt-hour
LCO_2	Liquid carbon dioxide
LH_2	Liquid hydrogen
LiBr	Lithium bromide
$\dot{m}$	Mass flow rate
MJ	Mega joules
MPa	Mega Pascals
CH_3OH	Methanol
M	Mixer
$\dot{Q}_{Cv}$	Net heat transfer rate
PV	Photovoltaic
P	Pump
h	Specific enthalpy
s	specific entropy
SO_2	Sulfur Dioxide
$\dot{W}_{Cv}$	Total work

T	Turbine
V	Valve
v	velocity of the working fluid
W/cm K	Watts per centimeter Kelvin
Xt.%	Weight percent
W	Work

INTRODUCTION

The energy demand has increased drastically due to population expansion and industrial improvements. Fossil fuels, as the most significant part of energy sources in the world, have side effects that threaten our lives and planet. Fossil fuels have brought about numerous challenges, including air pollution (pollutants such as Carbon Monoxide (CO), Sulfur Dioxide (SO_2), and Dioxins), global warming, and climate change (Manisalidis et al., 2020; Rastegari et al., 2019).

While these emissions' consequences are already evident in global warming, snow patterns, the acidity of oceans' water, and polar ice coverage, even more significant concerns are ahead. We should expect more emissions without major changes to the world's energy system. Based on the Intergovernmental Panel on Climate Change (IPCC) estimation, we must significantly reduce the current CO_2 level by 2050 to maintain the global temperature augmentation below 2 degrees Celsius (Orr, Jr., 2009).

Renewable energies are a sustainable potential alternative to address the challenges of fossil fuels, including pollution and growing demand. In this regard, hydrogen has attracted the attention of researchers and industry as an exceptional option to increase the use and overcome the intermittency of renewable energies. Different hydrogen production processes have been proposed based on energy consumption (Azarpour et al., 2022; Ghazvini et al., 2019).

By 2050, it is estimated that renewable energy will make up 63% of all primary energy needed, while it contributed only 14% in 2015. Similarly, the power domain is predicted to jump from 25% in 2015 to 85% in 2050 (Gielen et al., 2019). Renewable energies, however, still face some obstacles, including inaccessibility because of weather conditions, average efficiency, significant space for installation, and expensive initial costs. Energy storage is a suitable way of tackling the weather conditions effect on renewable energy production and also a way to produce energy from the waste heat of different processes (Azarpour et al., 2022; Ghorbani, Zendehboudi, et al., 2021; Hassan et al., 2021).

The thesis is structured into five main chapters, followed by a conclusion.

- Chapter 1 provides fundamentals aspects and an overview of the thesis topic, focusing on hydrogen storage techniques and introducing the concept of hydrogen liquefaction.
- Chapter 2 is dedicated to the literature review, offering valuable insights into state-of-the-art research while identifying key research questions and objectives.
- Chapter 3 describes the three processes utilized in the thesis: ABR, DAR, and ORC/Kalina processes.
- Chapter 4 outlines the thesis methodology.
- Chapter 5 presents the results and discussion, followed by a separate conclusion section.

The study also includes recommendations for future research, highlighting potential exploration areas for advancing upcoming projects.

CHAPTER 1

FUNDAMENTALS OF HYDROGEN PRODUCTION

1.1 Introduction

This chapter provides fundamentals aspects and an overview of the thesis topic, focusing on hydrogen storage techniques and introducing the concept of hydrogen liquefaction.

1.2 The necessity of hydrogen storage

Hydrogen, a primary or secondary product of various industrial processes, may be used in different industries, including petroleum, petrochemicals, aerospace, and military, and has different applications as a refrigerant, fuel, feedstock, or power source in fuel cells. Apart from fossil fuels as the initial production method of hydrogen, other methods include fuel processing, thermochemical cycles, electrolysis, and renewable energies. Hydrogen can be produced in water electrolysis and thermos-electrochemical processes using the energy generated by nuclear power plants or renewable sources like solar, biomass, geothermal, or wind. End-users of hydrogen are not always near the production sites; therefore, a system of hydrogen storage is required to tackle the challenge since transferring hydrogen via pipelines might not always be practical (Ghorbani, Zendehboudi, Saady, & Dusseault, 2023a). Moreover, hydrogen production and consumption rates may differ over time. As a result, stationary and mobile hydrogen storage helps for more reliable and efficient energy production and transformation. One effective method for reducing energy consumption and greenhouse gas emissions in power generation is peak shaving, which is the short-term storage of hydrogen (Y. Zhang et al., 2017).

1.3 Hydrogen storage techniques

As different application-based storage methods demonstrate, hydrogen has an invaluable characteristic: its versatility. These methods of storing must be selected considering a various

number of critical considerations, including storage duration and scale, temperature, safety, mobility, pressure, physical state, volumetric and gravimetric densities, price, resources, and available technologies (Madadi Avargani et al., 2022)

Three main methods of H_2 storage were mentioned by (Ghorbani, Zendehboudi, Saady, Duan, et al., 2023a): The first method is physical-based, including compressed gas, liquid, and two phases. The second method is material-based, which can be physical or chemical adsorption-based. The third method is chemical-based with two subcategories: reformed organic fuels and liquid organic H_2 carriers (LOHCs). Figure 1-1 illustrates these methods and subcategories.

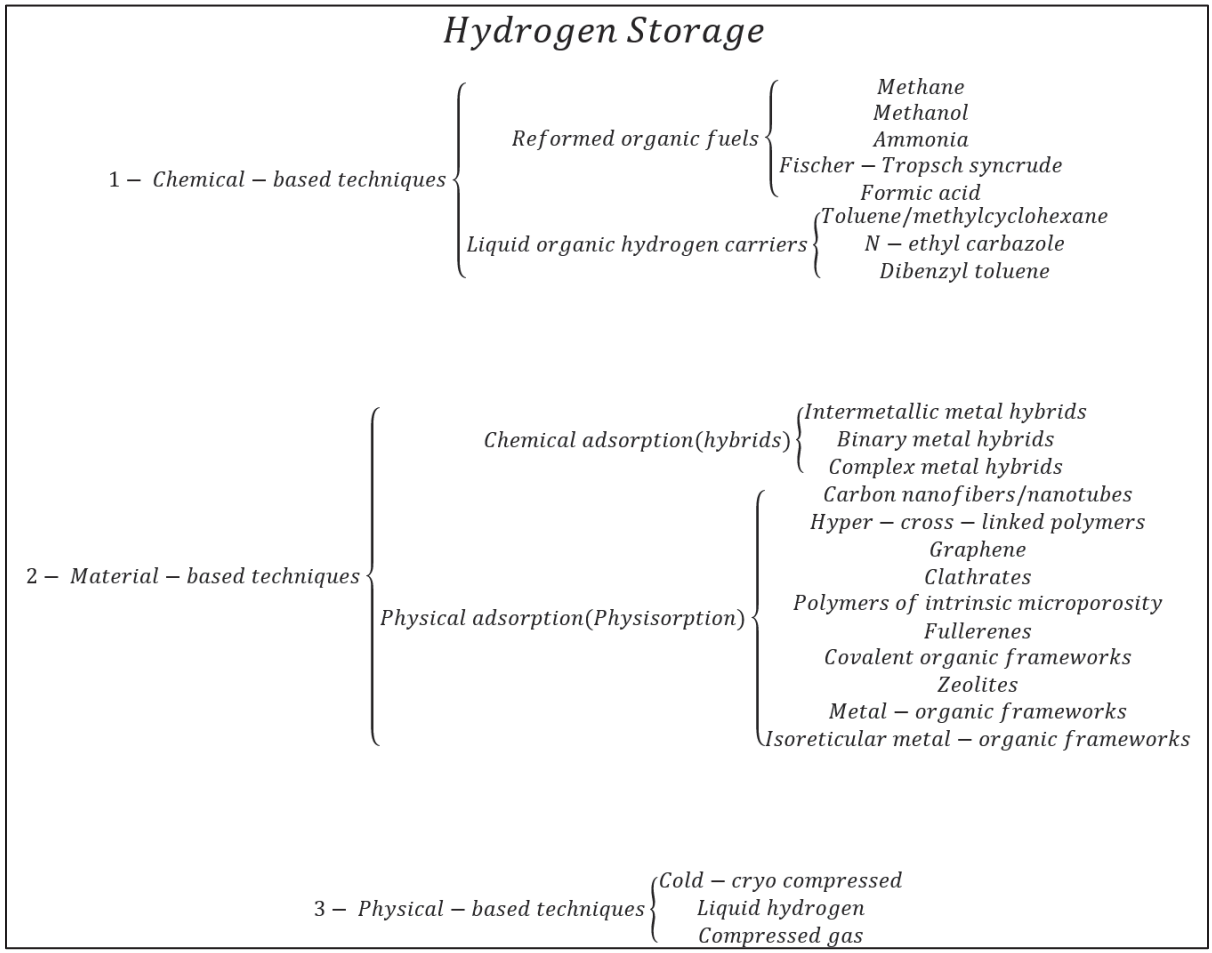

Figure 1-1 Different techniques of hydrogen storage

1.3.1 Physical-based techniques

Physical-based techniques are more practical than other methods. Without utilizing chemical reactions and sorbent materials, physical-based methods do not change the natural state of hydrogen. This technique encompasses hydrogen compression, H_2 liquefaction, and two-phase hydrogen storage systems. The ultimate goal introduced by the U.S. Department of Energy (US DoE) for hydrogen storage is to achieve a gravimetric density of 7.5 wt.% and a volumetric density of 7.0 wt.% while the price must be under 8 $/kWh per kilogram of hydrogen (Ghorbani, Zendehboudi, Saady, & Dusseault, 2023a; F. Zhang et al., 2016).

1.3.1.1 Compressed hydrogen gas storage

To achieve low volume and high pressure, it is widely common to use gas compression techniques for gaseous fuels such as hydrogen, natural gas, and town gas. However, it is more energy-consuming for a specific mass and compression ratio in the hydrogen case due to its lower specific gravity than in other cases. Due to their simplicity, pressure vessels are suitable options for small-scale storage via frequent charge and discharge cycles. Research on creating low-weight, high-strength vessels must consider chemical inertness with hydrogen to prevent hydrogen embrittlement (Ni, 2006). For small to medium-sized applications, hydrogen storage can be achieved using gasometers (gasholders) and spherical or cylindrical vessels for both stationary and mobile uses. Gasometers are large containers that store gas under near-ambient pressure and temperature, primarily for short-term storage, and they help balance the demand for gaseous fuels. However, underground storage — whether in natural or artificial reservoirs — is more suitable for large-scale applications, typically at lower to moderate pressures (Elberry et al., 2021). While liquefaction of hydrogen takes around 30% of the energy stored in it, called the lower heating value (LHV), compression hydrogen, if imagined as an ideal gas, takes about 7% of the energy, equal to around 8 MJ per kg H_2. However, in reality, it is calculated to be approximately 15% of LHV to achieve 700 bar or 12% to achieve 350 bar pressure, which is still significantly less than the required energy for hydrogen liquefaction (Felderhoff et al., 2007).

1.3.1.2 Liquid hydrogen storage

Hydrogen can be stored as a liquid in an insulated container to have higher volumetric and gravimetric densities than compressed hydrogen gas. The process involves compressing and cooling hydrogen gas below the boiling point of hydrogen (-253 °C), causing it to liquefy. It requires about 11.88 MJ of energy per kilogram for hydrogen liquefaction, approximately 64% more than the energy needed for making hydrogen into a high-pressure gas. As this method is more expensive than high-pressure storage, the researchers focus on improving the efficiency of liquefaction processes (Ni, 2006). Hydrogen molecules exist in two forms: para-hydrogen and ortho-hydrogen (Figure 1-2). Both forms share the same chemical composition, consisting of two protons and two electrons, but differ in the spin direction of their electrons, which influences their mechanical properties. Ortho-hydrogen, which has a lower energy state, features anti-parallel electron spins and is three times more abundant than para-hydrogen under atmospheric conditions. However, at lower temperatures, the proportion of para-hydrogen increases. The conversion from ortho-hydrogen to para-hydrogen occurs slowly and requires specific catalysts to accelerate the process. It is crucial to convert hydrogen from ortho to para to minimize hydrogen losses during long-term storage, though this process releases heat and can lead to boil-off (Ghorbani, Zendehboudi, Saady, & Dusseault, 2023a).

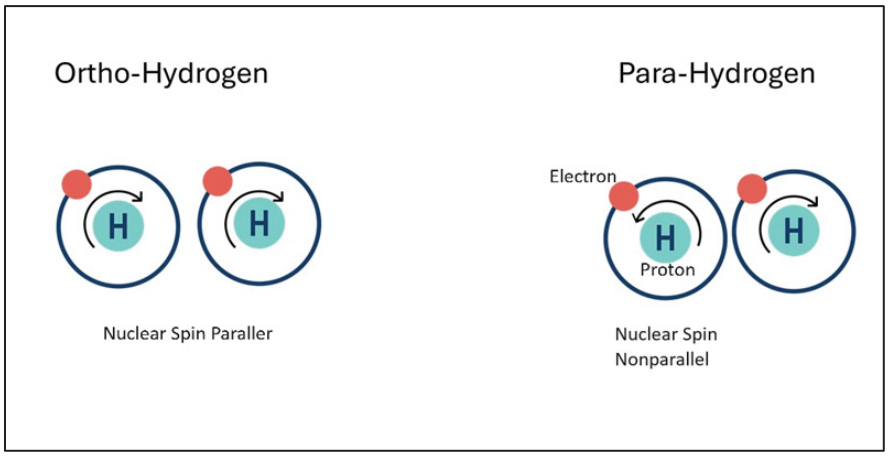

Figure 1-2 Two forms of Hydrogen molecule

1.3.1.3 Cryo-compressed

Cryo-compressed hydrogen storage offers the highest density among all available storage technologies, enabling vehicles to achieve ranges comparable to today's gasoline-powered vehicles. While this storage method has safety and cost advantages over other techniques, it still requires further development for commercial use. The design and application of these vessels necessitate thermodynamic considerations, including usage patterns, insulation effectiveness, the efficiency of liquid hydrogen pumps, vessel properties, and the conversion between para- and ortho-hydrogen (Moreno-Blanco et al., 2019).

Based on the cryo-compressed hydrogen storage method, BMW has introduced a system where pressure vessels can operate at cryogenic temperatures (around 20 K) and high pressures (approximately 35 MPa). This innovation allows for high-density hydrogen storage, similar to liquid hydrogen, but with minimal evaporative losses during regular use. This method benefits from reduced power consumption by avoiding the energy-intensive liquefaction process. While latent heat accounts for about 41% of the total energy consumption, it contributes only 10% to the overall thermal load. Therefore, the cryo-compressed hydrogen (CcH2) technique achieves higher volumetric density and lower energy consumption than the hydrogen liquefaction process by simultaneously compressing and cooling the hydrogen (Yanxing et al., 2019).

1.3.2 Hydrogen material-based storage

One of the most promising hydrogen storage methods for volume is material-based techniques, in which hydrogen atoms and molecules bond strongly with other elements. This technique has two main types (F. Zhang et al., 2016):

1- Physisorption (Physical adsorption): In this technique, hydrogen atoms or molecules adhere to other materials' surfaces.
2- Chemisorption (Chemical adsorption): In this method, hydrogen atoms form chemical bonds with other elements, allowing storage at low volumes and pressures at atmospheric temperatures. This approach offers high gravimetric capacity with low

volume, reversible hydriding and dehydriding, a favorable temperature-to-pressure ratio, insensitivity to impurities, and stable hybrid formation, making it an ideal technique for hydrogen storage. However, in practice, no single material has yet been found that possesses all the necessary properties for optimal hydrogen storage.

1.3.2.1 Physical adsorption

Gas molecule physisorption on a solid surface arises from resonant fluctuations in charge distribution, known as dispersive or van der Waals interactions. In this process, a gas molecule interacts with several atoms on the solid's surface, seeking to minimize potential energy at a distance roughly equal to the molecule's radius from the adsorbate. The binding energy in these interactions typically ranges from 0.01 to 0.1 eV. Due to their weak nature, these interactions occur primarily at low temperatures, usually below 100 K. Once the adsorbate monolayer forms, additional gas molecules interact with the adsorbate surface, which can be either solid or liquid. The binding energy of the second adsorbate layer becomes similar to the latent heat of sublimation or vaporization of the adsorbate. Consequently, the adsorption of a single monolayer is possible at a specific pressure when the temperature exceeds the adsorbate's boiling point. (Züttel et al., 2010).

Supercritical gases' adsorption adheres the two fundamental principles: the monolayer mechanism of adsorption and the adsorption exponential reduction when temperatures rise. As a consequence, the ability of hydrogen to adsorb onto a material relies on the material's specific area and the higher temperatures decrease this capacity. In addition to adsorption capacity other factors namely the solid surface's adsorption and compression affect the overall storage capacity (Zhou, 2005). A group of carbon-based materials including nanoporous activated carbon (AC), metal-organic frameworks (MOFs), and also single-walled carbon nanotubes (SWNTs) are being considered as potential options for hydrogen adsorption. Physisorption of these materials brings about rapid kinetics, and also low pressure. However, their drawbacks are highly dependent on temperature and need cryogenic conditions to reach the storage goals. Nanotubes have not yet met the DOE's targets despite their potential. To enhance their

performance, structural optimization may be done which should be tested experimentally (Bénard et al., 2007).

1.3.2.2 Chemical adsorption

Metal hydrides (MHs) offer practical advantages over traditional hydrogen storage methods such as compressed gas and liquefaction due to their high volumetric density and safe operational characteristics. These materials, made from various metals and alloys, can absorb and release hydrogen at different pressures and near-ambient temperatures. Three main types of MHs are used for chemical adsorption: intermetallic metal hydrides, binary metal hydrides, and complex metal hydrides. While MHs have lower gravimetric storage capacity, this limitation is not a significant challenge for stationary applications. The optimal operating conditions for MHs typically fall between 0 and 10 bar of pressure and 0 to 100°C, with decomposition enthalpies ranging from 15 to 24 kJ/mol (Ghorbani, Zendehboudi, Saady, & Dusseault, 2023a).

1.3.3 Hydrogen chemical-based storage

Chemical-based hydrogen storage systems use lightweight compounds, often in liquid form, to facilitate the transport and storage of mass and heat through hydrogenation and dehydrogenation processes. The most commonly known chemical-based components include methane, formic acid, liquid organic hydrogen carriers (LOHCs), ammonia, Fischer-Tropsch syncrude, and methanol. These components can also be synthesized from natural gas (NG) into bulk chemicals (Olabi et al., 2021).

Methane is not a viable direct method for hydrogen storage due to the high cost and complexity of extracting hydrogen from it. However, it is a potential portable fuel produced from hydrogen and CO_2 (Abbas & Wan Daud, 2010). Fischer-Tropsch (FT) can generate long-chain hydrocarbons from combinations of hydrogen and CO_2 to achieve a product resembling crude oil called syncrude. This product faces competition in the market and has low value. FT

synthesis is not yet optimized and cannot be considered a practical option in intermittent consumption (Preuster et al., 2017).

In industrial usages, methanol (CH_3OH) is usually generated from syngas, which is a blend of carbon monoxide (CO), carbon dioxide (CO_2), and hydrogen under a pressure of 50 to 100 bar and temperatures between 250 to 300°C. The process uses copper and zinc-based materials as a catalyst (Leonzio, 2018).

Ammonia (NH_3), a substance that can be found naturally, is known for its eco-friendly, thermodynamic and thermophysical characteristics. Ammonia possesses moderate toxicity and flammability. The Haber-Bosch process, which produces ammonia from hydrogen and nitrogen, is widely used. For large-scale hydrogen storage, ammonia dehydrogenation requires temperatures exceeding 650°C (Moradi et al., 2021; Mukherjee et al., 2018).

Liquid organic hydrogen carriers (LOHCs) are reversible energy carriers that transition between energy-lean and energy-rich states through hydrogenation and dehydrogenation. This process uses a liquid carrier that can undergo multiple cycles without being consumed (Teichmann et al., 2012).

1.4 The strengths and weaknesses of liquid hydrogen

Hydrogen is an abundant source of clean energy, making it an attractive option for energy storage and transfer. Compared to conventional fuels, hydrogen has a lower flash point, a higher octane number, and emits no greenhouse gases while being both colorless and odorless (Ghorbani, Zendehboudi, Saady, & Dusseault, 2023a). The physical properties of hydrogen are listed in Table 1-1 as follows (Ghorbani, Zendehboudi, Saady, Duan, et al., 2023a):

Table 1-1 Physical Properties of Hydrogen

Properties	Values	Units
Molecular weight	2.016	g/mol

Properties	Values	Units
Lower heating value	119.9	MJ/Kg
Higher heating value	141.6	MJ/Kg
Viscosity, 25 °C	0.000892	cP
Boiling temperature, 1 atm	-253	°C
Melting temperature	-259.1	°C
Critical temperature	-240.1	°C
Critical pressure	1.29	Mpa
Density of gaseous H_2, 0 °C	0.0898	Kg/m^3
Density of liquid H_2, -253 °C	70.85	Kg/m^3
Density of solid H_2, -259 °C	858	Kg/m^3
Critical density	31.2	Kg/m^3
Heat capacity of gaseous H_2, 0 °C	14.3	kJ/kg0 °C
Heat capacity of liquid H_2, -256 °C	8.1	kJ/kg0 °C
Heat capacity of solid H_2, -259.8 °C	2.63	kJ/kg0 °C
Heat of vaporization, -253 °C	0.447	MJ/Kg
Heat of fusion, -259 °C	0.058	MJ/Kg
Thermal conductivity, 25 °C	0.018	W/cm K
Ionization energy	13.59	eV
Flame emissivity	17-25	%
Liquid-to-gas expansion ratio at atmospheric conditions	1:848	
Flame temperature in air	2045	°C
Adiabatic flame temperature	2107	°C
Research octane number	>130	
Thermal conductivity, 20 °C, 1 atm	0.1825	
Specific gravity of gas H_2, 20 °C, 1 atm	0.0696	
Specific gravity of liquid H_2, -253 °C, 1 atm	0.0710	
Latent heat of vaporization	0.461	MJ/Kg

The main problem in storing and transporting hydrogen is its low energy density in the gaseous state. It is possible to increase the energy density of the hydrogen from 0.01 MJ/l in the gas phase to 8.50 MJ/l in the saturated liquid state. Liquid hydrogen has privileges over gaseous hydrogen as the liquid hydrogen has lower weight and volume and enhanced energy density (Aasadnia & Mehrpooya, 2018b; Naquash et al., 2022).

Hydrogen production and storage can be effectively combined with renewable energy sources. Storing excess energy produced from renewables creates opportunities to enhance the utilization of clean energy, thereby reducing environmental impacts. When renewable energy sources are insufficient to meet demand, such as during peak consumption, the stored hydrogen can generate electricity. Additionally, cogeneration systems integrating hydrogen production with waste heat from industries, renewable sources, nuclear power plants, and LNG production plants offer significant opportunities for various sectors.

Compared to conventional energy storage systems, hydrogen storage can be used for more extended periods, such as for seasonal energy requirements, and in situations requiring high storage capacity due to its ability to support high power rates (i.e., in the range of 10 MW) (Aasadnia & Mehrpooya, 2018b; Ghorbani, Zendehboudi, Saady, Duan, et al., 2023a; Kharel & Shabani, 2018). However, despite the advantages of liquefaction-based hydrogen storage, the related technologies remain expensive, and the system efficiency is not yet optimal (Ghorbani, Ebrahimi, et al., 2021).

One of the main challenges associated with hydrogen fuel is improving hydrogen storage systems (Rusman & Dahari, 2016). Key obstacles include low exergy efficiency, high specific energy consumption (SEC), and inevitable boil-off gas (IBOG) losses (Taghavi et al., 2022; J. Zhang et al., 2005). Boil-off losses during the storage, handling, and transportation of liquid hydrogen can account for up to 40% of its available combustion energy (Al Ghafri et al., 2022a).

From an economic perspective, hydrogen liquefaction is expensive due to the inefficiency of current equipment and processes (Aasadnia & Mehrpooya, 2018c), coupled with high maintenance costs for hydrogen production and storage systems. A potential solution proposed by Al Ghafri and co-workers to reduce the energy intensity of hydrogen liquefaction is to scale up production capacities to 100 tons per day (TPD) or more. Increasing production volumes can lower both the SEC and the cost of liquefied hydrogen (Al Ghafri et al., 2022a; Ghorbani, Zendehboudi, Saady, & Dusseault, 2023b). However, this approach requires significant financial investment and adds system complexity. Furthermore, producing hydrogen in such large quantities is not always feasible in specific regions, and transportation costs remain high (Ghorbani, Zendehboudi, Saady, Duan, et al., 2023b).

1.5 Enhancing the performance of hydrogen liquefaction systems.

Hydrogen liquefaction can be designed in countless ways, but the process generally involves four stages: gas compression at ambient temperature, precooling to around 80 K, cryogenic cooling from 80 K to 30 K, and finally, liquefaction of hydrogen at 30 K under a pressure of 1 atm (Quack, 2002).

Liquefaction cycles are the core of hydrogen liquefaction systems, and they are of three main types: the Lind-Hampson cycle, the Claude cycle, and the Brayton refrigeration cycle. The Lind-Hampson cycle, developed in 1895, is one of the earliest methods for gas liquefaction. Due to its relatively low efficiency, it is best suited for small-scale applications (less than 2 tons per day, or TPD). This cycle begins with gas compression, followed by cooling at nearly constant pressure through two heat exchangers, and then Joule-Thomson expansion. The Claude cycle improves the cooling process by using an expander to cool part of the feed, increasing hydrogen flow in the second heat exchanger. This cycle, suitable for large-scale operations (around 42 TPD), has undergone several industrial and research modifications. Typical improvements include adding more heat exchangers or using nitrogen for precooling. The Brayton refrigeration cycle uses a closed-loop refrigeration system with helium, nitrogen, or a mixed refrigerant (MR) as the working fluid to cool hydrogen vapor. Initially considered

more suitable for small-scale applications, recent research suggests it could be adapted for large-scale systems (Al Ghafri et al., 2022b).

Several methods have been proposed to reduce the specific energy consumption (SEC) of the hydrogen liquefaction process, with many focusing on optimizing the precooling stage before the ortho-to-para hydrogen conversion. In the cryogenic section, the use of a cascade liquefaction process can help lower SEC. Figure 1-3 provides a schematic of various precooling methods to reduce SEC.

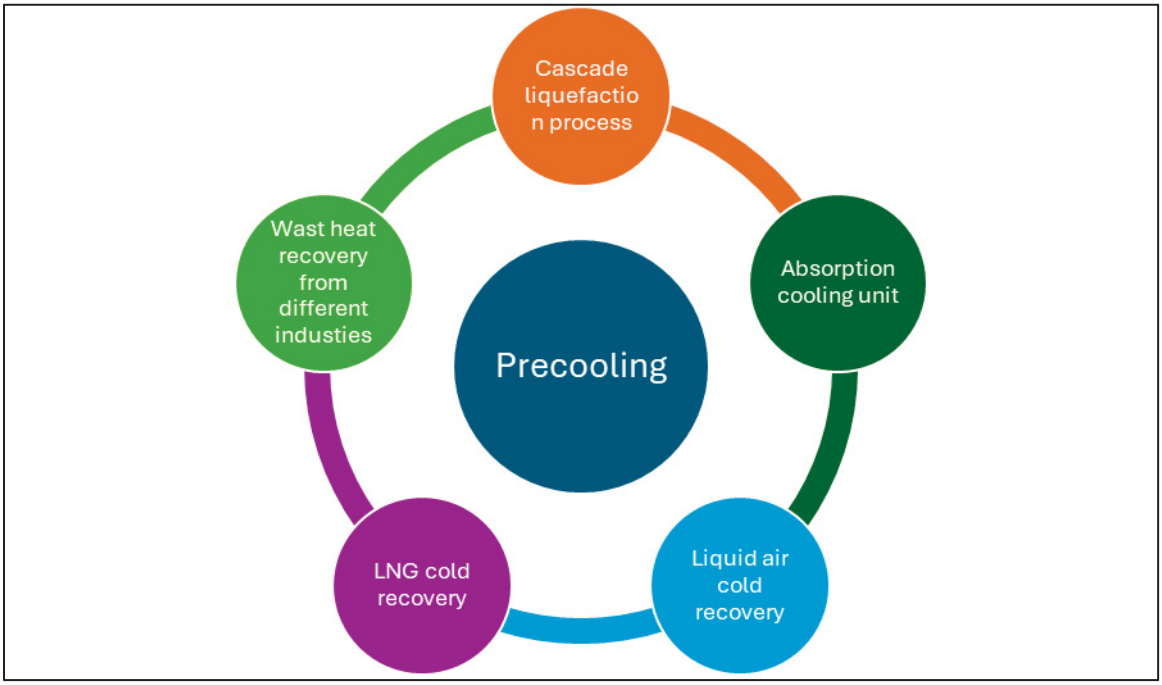

Figure 1-3 Different precooling methods for optimizing the hydrogen liquefaction systems

Examples of techniques to reduce SEC in hydrogen liquefaction include absorption cooling cycles, ejector cooling systems, energy recovery from LNG, cascade liquefaction processes, multi-refrigerant cycles, integrated process combinations, algorithmic optimization, pinch analysis, and the use of renewable energy sources. Research shows that replacing hydrogen refrigerants with multi-refrigerant systems like helium and neon can significantly reduce energy consumption. Additionally, absorption-compression refrigeration cycles, LNG

regasification cycles, and recovering cold energy from liquid air and nitrogen during the precooling stage also contribute to SEC reduction. By employing these advanced methods, the cost of liquefying hydrogen for a plant with a 100 TPD capacity can be reduced by about 67% compared to a conventional plant with a capacity of 5 TPD (Ghorbani, Zendehboudi, Saady, Duan, et al., 2023b; Ghorbani, Zendehboudi, Saady, & Dusseault, 2023a).

CHAPTER 2

LITERATURE REVIEW AND PROBLEM DESCRIPTION

2.1 Introduction

There are different ways to increase the efficiency of the hydrogen liquefaction process, including refrigeration and power optimization methods.

1- Absorption refrigeration: Ammonia-water
2- Diffusion-absorption refrigeration: Ammonia-water-helium
3- Organic Rankine cycle and Kalina power cycle

With this, there is a literature review of the works on these three promising techniques.

2.2 Absorption cooling cycle

Absorption cooling systems can be used instead of compression cooling systems in H_2 liquefaction processes to save energy. Consequently, the H_2 liquefaction cycles can benefit from removing some parts of the condensation cooling systems. As a result, the whole system benefits from less investment required and less probable maintenance expenses. In this regard, different refrigerants may be utilized in absorption cooling systems. Among different types of working fluids in absorption cooling cycles (ACCs), water-lithium bromide (LiBr-H_2O) and ammonia-water (NH_3–H_2O) are the most common (Ghorbani, Zendehboudi, Saady, Duan, et al., 2023a; Srikhirin et al., 2001).

Geothermal energy has been utilized in hydrogen liquefaction by (Kanoglu et al., 2007) across three main applications. In the first case, geothermal energy was harnessed in a power plant. In the second, it was used for an absorption cooling cycle to precool hydrogen. In the third case, geothermal energy contributed to both work production and hydrogen precooling in the liquefaction process. Notably, using geothermal energy for absorption cooling is more

beneficial than for power generation, as it reduces the specific energy consumption (SEC) required for hydrogen liquefaction.

Ratlamwala, Dincer, Gadalla, et al., (2012) conducted evaluations of exergy and energy for an integrated hydrogen liquefaction system. Their study proposed a triple-effect absorption cooling cycle (ACC) integrated with geothermal and solar photovoltaic/thermal (PV/T) energy alongside a Lindee Hampson (L−H) cycle. The authors found that increasing geothermal energy reduced the exergy utilization factor from 0.21 to 0.013 and the energy utilization factor from 0.059 to 0.037. Additionally, with increased geothermal input, the values for precooling and hydrogen liquefaction decreased from 0.42 to 0.27 and from 0.088 to 0.066. A similar study (Ratlamwala, Dincer, & Gadalla, 2012) investigated the effects of geothermal energy, ammonia-water concentration, and ambient temperature on system efficiency. They demonstrated that higher ammonia-water concentration improved hydrogen liquefaction rates from 0.07 kg/s to 0.11 kg/s.

In another study, (Kanoglu et al., 2016) examined an integrated system using an ammonia-water (NH3–H2O) refrigeration cycle for hydrogen precooling. This system utilized the Claude cycle for hydrogen liquefaction, drawing on a geothermal energy source with a heat rate of 100 kg/s at 200 °C for the absorption system generator. This approach reduced work consumption in the liquefaction process by 25.4%. Hydrogen was cooled to -26.9 °C at a rate of 29.53 kg/s in the absorption system. The coefficients of performance (COP) for the absorption refrigeration and Claude cycles were determined to be 0.556 and 0.0120, respectively. The exergy efficiencies based on the fuel-product approach were 67.0% and 67.3% for these cycles. The entire system's COP and exergy efficiency were recorded as 0.162 and 67.9%, respectively.

In two similar integrated systems, (Yilmaz & Kaska, 2018) and (Yilmaz, 2018) investigated the effects of using ammonia-water absorption refrigeration for precooling in hydrogen liquefaction. In both studies, the energy required for the absorption cycle was supplied by geothermal energy. The base cases for hydrogen liquefaction were designed using LN_2 and the

Claude liquefaction cycle, with ammonia-water employed in the absorption cycle and an evaporator temperature calculated at -26.9 °C. Optimization calculations using a genetic algorithm in the first study indicated that hydrogen could be precooled to -30 °C, resulting in a relative cost saving (RCS) of 11.4%, while the second study achieved an RCS of 32.4%.

Aasadnia & Mehrpooya (2018a) proposed a hydrogen liquefaction cycle that combined a new mixed refrigerant (MR) refrigeration cycle with the Joule-Brayton cycle. This study aimed to optimize energy savings through absorption refrigeration precooling. The results showed a reduction in specific energy consumption (SEC) from 7.69 kWh/kg LH_2 to 6.47 kWh/kg LH_2, while exergy efficiency increased from 39.5% to 45.5% with the absorption precooling cycle. The process was simulated using the Aspen HYSYS simulator, demonstrating a production rate of liquid hydrogen (LH_2) of 90 tons per day.

In a subsequent study, Aasadnia et al. (2019) performed exergy, exergoeconomic, and exergoenvironmental analyses of a proposed hydrogen liquefaction process integrated with absorption refrigeration systems. This cycle combined a simple Claude cycle with two ammonia-water absorption refrigeration systems and utilized renewable solar energy. The study presented the highest and lowest exergy, exergoeconomic, and exergoenvironmental performance coefficients for different equipment. Pumps and heat exchangers were recommended to be modified to enhance the cycle's overall exergy efficiency. The proposed system was estimated to produce approximately 260 tons per day of liquid hydrogen (LH_2), consume 2.7 kWh for each kilogram of LH_2, and achieve an exergy efficiency of 31.6%.

Ghorbani et al. (2019) modified and thermodynamically analyzed a system for producing liquid hydrogen, anticipating an output of approximately 290 tons of liquid hydrogen (LH_2) per day. The modified system incorporated a basic hydrogen liquefier, an organic Rankine cycle, a renewable solar energy resource, and a precooling absorption refrigeration system. This configuration was found to reduce exergy consumption and enhance exergy efficiency from 55.47% to 73.75%. The organic Rankine cycle utilized a two-stage mixed refrigerant

cycle (MRC), where the first stage cooled hydrogen from 25 °C to -195 °C before passing it to the second MRC for further cooling to -254.5 °C (LH_2).

Rezaie Azizabadi et al. (2021) introduced a framework using waste heat from a gas turbine exhaust in an ammonia-water absorption cycle to produce liquid hydrogen, explicitly analyzing the Parand gas power plant. The system was designed to produce 4 kilograms of liquid hydrogen per second, with the exhaust gases entering the absorption cycle at 546 °C, allowing hydrogen to be precooled from 25 °C to -30 °C before liquefaction. The cycle achieved a coefficient of performance (COP) of 0.271 and a specific energy consumption (SEC) of 4.54 kWh per kilogram of liquid hydrogen. The authors noted several advantages of using waste exhaust gases over geothermal and solar energy for the absorption cycle. The exhaust gases have a higher temperature (around 550 °C) than the typical solar supply temperature of about 200 °C. Economically, utilizing waste heat is more cost-effective since it requires less equipment. Additionally, locating the proposed structure near the power plant minimizes distribution losses, facilitating hydrogen liquefaction and storage during off-peak hours.

Naquash et al. (2022) implemented the ammonia-water absorption cooling cycle in an integrated hydrogen liquefaction system, coupled with a liquid air energy storage system to precool hydrogen to -180°C before it entered the organic Rankine cycle, which also utilized waste heat from air combustion. The total SEC of the system was measured at 6.71 kWh/kg, with an exergy efficiency of 35.7%. An economic analysis revealed that compressors and multi-stream heat exchangers accounted for 88.5% of the total project budget. Notably, while the exergy destruction of the absorption cycle constituted only 3.67% of the total exergy destruction in the system, the liquid air energy storage unit contributed significantly at 94.16%.

Another study (S. Zhang et al., 2023) utilized a two-stage ammonia-water absorption refrigeration system for precooling hydrogen liquefaction. This integrated system harnessed waste heat from both geothermal and solar energy sources, where solar power and thermal energy storage provided the necessary energy and contributed waste heat to the absorption refrigeration cycle. The hydrogen liquefaction base cycle included a closed Claude precooling

and a Joule-Brayton refrigeration cycle. The system was projected to produce 367.2 tons of LH_2 per day, achieving a minimum SEC of 5.413 kWh/kg LH_2, a maximum COP of 0.1433, and a maximum exergy efficiency of 86.99%. The study also detailed various components' exergy destruction and efficiency, including compressors, pumps, heat exchangers, and solar heaters.

2.3 Diffusion-absorption refrigeration (DAR)

Diffusion-absorption refrigeration (DAR) is an absorption refrigeration technique that generates cooling using renewable energy sources or waste heat, rather than electrical power. DAR systems are commonly employed in various applications, including domestic refrigeration, hotel freezers, and supermarket chillers. A notable advantage of DAR, patented by Von Platen and Munters, is its operation at a single pressure level, unlike traditional ammonia-water (NH_3-H_2O) absorption cycles. The system primarily utilizes NH_3 as the refrigerant, water as the absorbent, and either helium or hydrogen as an inert gas, which is essential for reducing the partial pressure of the refrigerant in low-temperature evaporators. Recent studies have increasingly focused on integrating DAR cycles with renewable energy sources (Mousavi et al., 2022). For instance, Mousavi et al. (2022) examined a structure combining an organic Rankine cycle with solar-based DAR in remote settings.

In another study, (Mehrpooya et al., 2021) designed and evaluated a hydrogen purification process using DAR. Their analysis included exergoeconomic and exergy evaluations, with helium as the inert gas. They found that helium yielded the most optimal refrigeration duty and lowest temperature compared to neon and hydrogen. The DAR system achieved a cooling capacity of 7.125 kW at -32.61°C, with a coefficient of performance (COP) of 0.424, requiring 16.81 kW of thermal energy. The system produced a hydrogen stream with approximately 88% purity from an inlet stream of 55% purity. The authors proposed two new exergy efficiency indices, recording values of 93.825% and 35.053% for their study's first and second criteria, respectively. They also noted that the exergoeconomic factor (F-factor) decreased by an

average of 23.6% with a 50% increase in electricity costs, attributing 32% of the total exergy destruction (45.764 kW) to the air cooler.

Yildiz et al. (2014) investigated the impact of insulation on the exergy and energy coefficients in DAR systems. They found that insulating both the solution heat exchanger and part of the rectifier enhanced energy and exergy performance by 26% and 21%, respectively. Using helium, Yildiz (2016) compared the performance of electricity-driven and LPG-driven DAR systems. The exergy and energy efficiencies for the electricity system were 0.1008 and 0.393, while the LPG system showed 0.1067 and 0.432, respectively. The exergy cost rates were reported at 2.111 $/h for LPG and 1.284 $/h for the electricity system, highlighting a 64% higher exergy cost for the LPG system.

Mehrpooya, Amirhaeri, et al. (2022) aimed to reduce energy consumption in small-scale natural gas liquefaction using DAR and single mixed refrigeration (SMR). Using HYSYS software for simulations, they analyzed system performance under the weather conditions of Yazd, Iran. The structure produced approximately 57,850 kg/h of LNG using 12,440.35 kW of power. The exergy efficiencies were 0.09 for the DAR cycle and 0.083 for the SMR cycle, with a total exergy efficiency of 0.38. The DAR and SMR COPs were found to be 0.9 and 0.48, respectively. Notably, the DAR generator was identified as the primary exergy destructor, while using the DAR cycle reduced coal consumption by 19.36% and CO_2 emissions by 17.85%.

In a subsequent study, Mehrpooya, Mousavi, et al. (2022) thermodynamically assessed a combined SMR and DAR system for optimizing LNG production. The system produced 57,850 kg/h of LNG from a 63,850 kg/h natural gas feed at 6,650 kPa, with the DAR system providing 139,306 kW of cooling duty at -29.62°C. Exergy destruction contributions from the SMR and DAR systems were 51.46% and 48.54%, respectively, with heat exchangers being the most significant exergy destructors (around 30%).

Amirhaeri et al. (2024) designed a multi-generation system for producing biomass-based methanol LNG and liquid hydrogen to improve fuel production efficiency in forest-rich areas with LNG liquefaction plants. DAR utilized waste heat from methanol synthesis to optimize overall exergy and energy efficiency. Among the three hydrogen liquefaction processes evaluated, the combined mixed refrigerant cycle (CMRC) emerged as the most efficient option, achieving a specific energy consumption (SEC) of 5.462 kWh/kg LH_2. The DAR cooling temperature, required power, cooling power, and COP were -29.62 °C, 40,877.907 kW, 19,713.334 kW, and 0.157, respectively.

Taghavi & Lee (2024) explored two scenarios for reducing the SEC of hydrogen liquefaction. In the first scenario, a DAR cycle produced cooling duty from waste heat, achieving a hydrogen production rate of 0.5786 kg/s LH_2. The second scenario used waste heat for electricity generation. The evaluations showed that the DAR integrated system performed better thermodynamically, with an SEC of 4.320 kW/kg and exergy efficiency of 53.35%, compared to 4.359 kW/kg and 50.82% for the second scenario.

2.4 Organic Rankine Cycle and Kalina power cycle

The Organic Rankine Cycle (ORC) and Kalina Cycle (KC) are effective techniques for utilizing low-grade heat sources and generating power from waste heat and renewable energy. These methods find applications in power generation, desalination, and cooling, offering cost-effective alternatives to traditional fossil fuel systems. The ORC is recognized for converting sensible heat into mechanical power. In waste heat recovery, both ORC and KC are considered efficient means of harnessing low-temperature heat sources. While the simplicity of ORC's configuration enhances its reliability and flexibility, the KC can outperform it based on second law thermodynamics principles.

Research on waste heat recovery via ORC has identified the working fluid as a crucial factor affecting cycle performance. Studies have focused on optimizing working fluid selection and

comparing various ORC configurations to clarify their respective advantages and disadvantages (Nemati et al., 2017).

Ghorbani, Zendehboudi, et al. (2021) proposed an integrated configuration using the KC for liquefying hydrogen and oxygen, powered by wind turbines and an electrolyzer. The KC was chosen due to its superior performance under low-temperature conditions, utilizing a water-ammonia mixture that efficiently absorbs thermal energy for power generation. The flexible composition of the NH_3-H_2O mixture enhances the cycle's adaptability. In contrast to the Rankine cycle, where the output can transition from gas to a two-phase fluid (risking corrosion), the KC maintains a saturated mixture. The hydrogen and oxygen liquefaction simulation was performed for Newfoundland and Labrador, Canada, using HYSYS, TRNSYS, and MATLAB. This setup generates 2,100 kgmol/h of LH_2 powered by 264.1 MW from wind turbines, resulting in an 8.61% reduction in power consumption. The specific energy consumption (SEC) and coefficient of performance (COP) for hydrogen liquefaction were 5.462 kWh/kg H_2 and 0.1384, respectively, with KC's energy efficiency at 14.06%. The overall exergy efficiency was 58.73%, with significant exergy destruction attributed to electrolyzers (83.13%) and heat exchangers (5.93%).

In another study, Jouybari et al. (2022) integrated the KC into a hydrogen liquefaction system with a compression-ejector unit and six cascade multi-component refrigerant cycles for pre-cooling and liquefaction. The Kalina cycle utilized waste heat from the integrated system for power generation. The system required 595.6 MW to produce 22.34 kg/s of liquid H_2, with a SEC of 7.405 kWh/kg LH_2 and a COP of 0.103 for the liquefaction process. The thermal efficiency of the KC was determined to be 0.1228, with heat exchangers (39.55%), gas turbines (27.92%), and compressors (21.81%) contributing most to exergy destruction. A sensitivity analysis showed that increasing pressure in the KC initially reduced SEC to a minimum of 7.4135 kW/kg LH_2 at 26 bar before increasing again. The overall exergy efficiency of the integrated system was 0.2359.

Ebrahimi et al. (2022) implemented ORC and Kalina power systems using geothermal heat to cogenerate liquid CO_2 and biomethane ($bioCH_4$). The system captured CO_2 from the output fumes of power plants. In addition to ORC and KC, an absorption compression cycle operated with geothermal heat was used to cool unrefined biogas. This integrated structure produced 0.08434 kg/s of biomethane and 2.631 kg/s of LCO_2, with unrefined biogas and geothermal energy input rates of 2.368 kg/s and 7,922 kW, respectively. The overall exergy and thermal efficiencies were 73.10% and 59.94%, with 39.12% of total exergy destruction attributed to heat exchangers and distillation columns.

In a recent study, Liu et al. (2023) proposed an innovative biomass-based design for generating power, LH_2, heating, and cooling capacity. This integrated structure involved various cycles, including a Brayton and modified Kalina cycles. The Brayton cycle, powered by municipal solid waste, was used for cooling and power generation, while hydrogen from the evaporator of the Kalina cycle was utilized to meet cooling demands before entering the Claude cycle. The study evaluated performance based on the first and second thermodynamic laws, yielding output power of 5,225 kW, a cooling load of 73.34 kW, and LH_2 production of 0.0380 kg/s.

2.5 Research questions

The following research questions shape the research path and highlight the research constraints:

- How does integrating various waste heat recovery cycles impact a hydrogen liquefaction process's overall efficiency and energy consumption?

- What are the comparative benefits and drawbacks of different waste heat recovery cycles in hydrogen precooling applications, such as ABR, DAR, and ORC/Kalina?

- What are the key factors contributing to exergy destruction in hydrogen liquefaction cycles utilizing waste heat recovery, and how can these be minimized?

2.6 Research objectives

After looking into the relevant literature, the objectives of the thesis are:

- Evaluate the Impact of Waste Heat Recovery: Assess how integrating various waste heat recovery cycles influences energy efficiency and specific power consumption in hydrogen liquefaction processes.

- Comparative Analysis of Recovery Cycles: Perform a comparative study of different waste heat recovery cycles (including Absorption Refrigeration, Diffusion-Absorption Refrigeration, and Organic Rankine/Kalina cycles) specifically for hydrogen liquefaction, focusing on metrics such as specific power consumption, exergy efficiency, and overall process performance.

- Identify Sources of Exergy Destruction: Analyze the primary sources of exergy destruction in hydrogen liquefaction cycles that utilize waste heat recovery and explore strategies to minimize these losses.

CHAPTER 3

PROCESS DESCRIPTION

3.1 Hydrogen liquefaction process

Figure 3-1 presents the schematic of the various scenarios considered for the hydrogen liquefaction process. The core of the integrated system is designed to produce 4167 kg/h of liquid hydrogen at a temperature of -253.5 °C and a pressure of 1.3 bar (Figure 3-2). The process flow diagram (Figure 3-3) outlines a consistent liquefaction process across all three scenarios under investigation.

Process Description

Here, a brief description of this process is presented. The hydrogen enters the system as stream H1 at a pressure of 21 bar and a temperature of 25 °C. It passes through multiple multi-flow heat exchangers: H6, H7, and H8. This network of heat exchangers performs precooling, reducing the hydrogen's temperature to -45.0 °C after HX6, -105.0 °C after HX7, and -195.0 °C at stream H4 after HX8.

In the process, hydrogen exists in two isomeric forms: ortho-hydrogen and para-hydrogen. Ortho-hydrogen features hydrogen molecules with parallel spins, while para-hydrogen has antiparallel spins. The conversion from ortho-hydrogen to para-hydrogen is essential, as para-hydrogen has a lower thermal energy and boiling point, facilitating liquefaction.

Following the heat exchangers, the hydrogen passes through two conversion reactors (CR1 and CR2). After CR1, the concentration of para-hydrogen reaches 28%, and it reaches 100% after CR2. Before entering CR2, the hydrogen's temperature is lowered to -239.5 °C using cascaded Claude cycles, which provide the necessary cryogenic cooling.

After passing through HX13, the hydrogen reaches -253.0 °C. At this stage, the hydrogen pressure is still at 21 bar, so turbine T7 is employed to reduce the pressure of stream H13 to

1.3 bar, making it ready for storage and transportation. The Peng-Robinson equation of state is utilized in Aspen HYSYS V10 to simulate this liquefaction process.

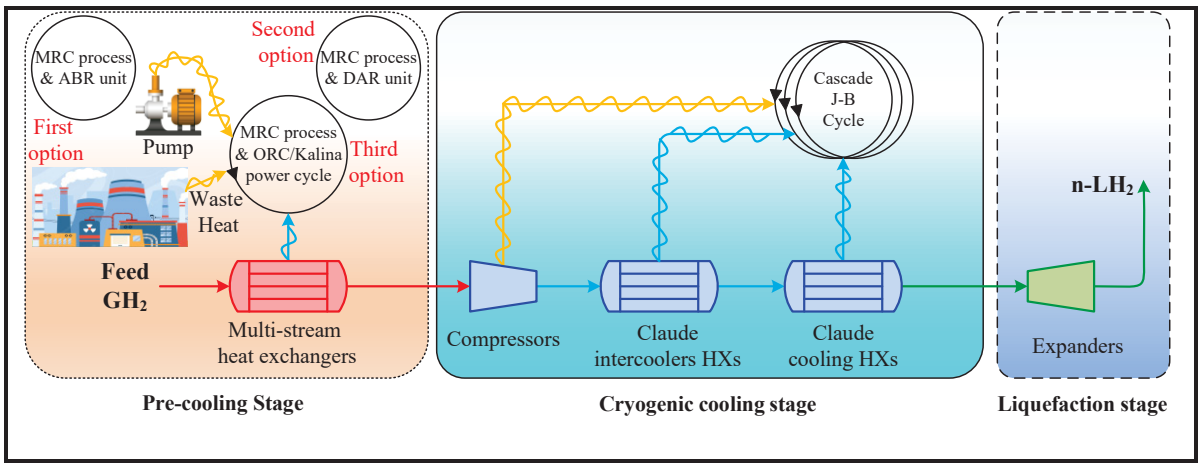

Figure 3-1 The schematic of the different scenarios considered for the hydrogen liquefaction process

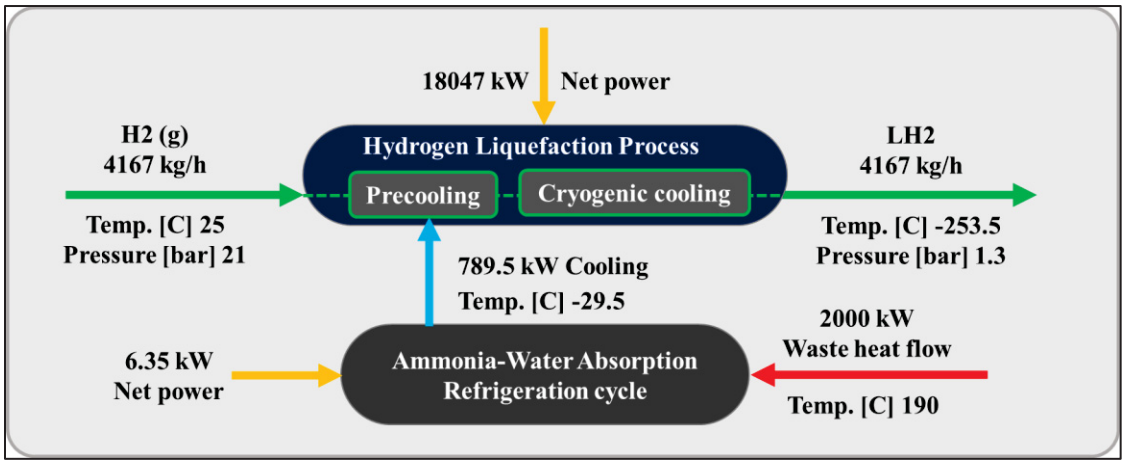

Figure 3-2 Block Flow Diagram (BFD) of the hydrogen liquefaction process by the implementation of the Ammonia-Water Absorption Refrigeration Cycle

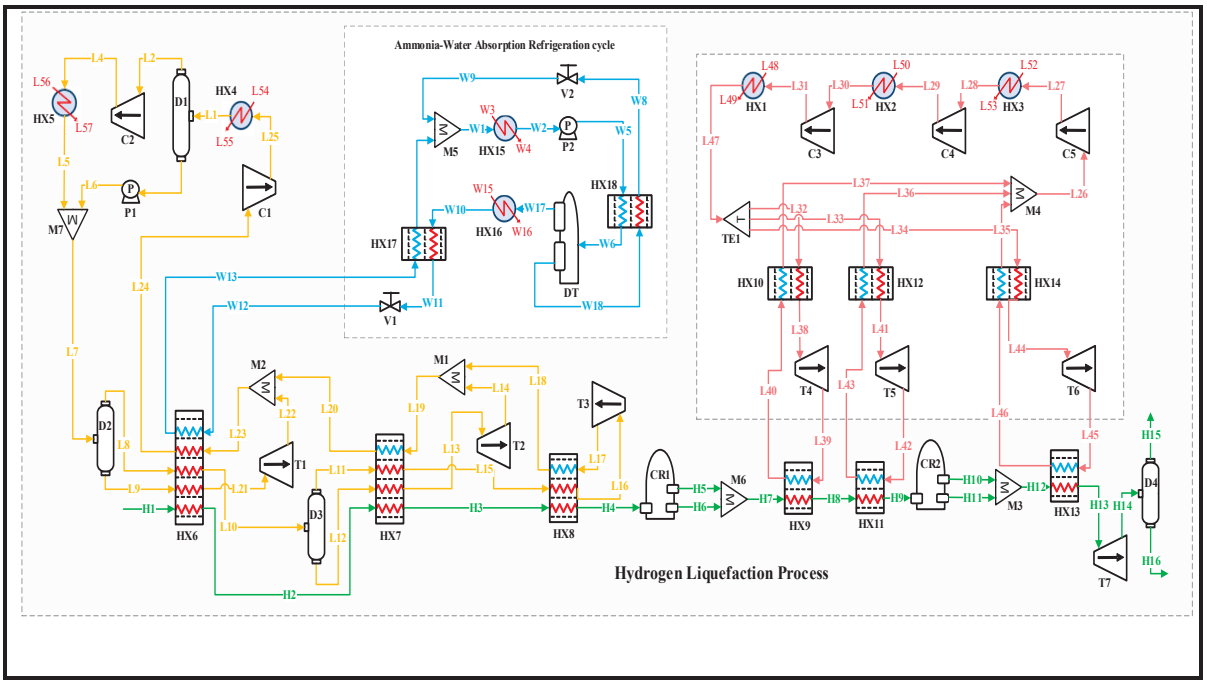

Figure 3-3 Process Flow Diagram (PFD) of the hydrogen liquefaction process by the implementation of the Ammonia-Water Absorption Refrigeration Cycle

Precooling Stage Overview

In the precooling phase, the multi-component refrigerant stream (L7) enters the D2 flash drum, where it separates into liquid and vapor phases. These phases then flow into the HX6 heat exchanger, providing part of the cooling required to reduce the hydrogen temperature to -45°C. A similar process occurs with the L10 stream. After passing through heat exchangers HX6, HX7, and HX8, the gaseous phases of the coolant streams enter the T1, T2, and T3 turbo expanders to decrease pressure. These expanded gases are collected through mixers M1 and M2. The returning stream L24, following two stages of compression and cooling to 25 °C, enters mixer M7 before proceeding to the D2 flash drum.

Claude Cryogenic Refrigeration Cycle

The Claude cryogenic refrigeration cycle further lowers the hydrogen temperature to -239.5 °C. Renowned for its high thermodynamic efficiency, the Claude cycle is particularly effective in large-scale liquefaction plants and is adaptable to various gases, including hydrogen, helium, nitrogen, oxygen, and natural gas.

This cycle utilizes a multi-component refrigerant comprising hydrogen, helium, and neon. It captures heat from the hydrogen stream in heat exchangers HX9, HX11, and HX13. After collecting the refrigerant streams in mixer M4, the combined stream (L26) undergoes three compression stages in compressors C3, C4, and C5, increasing its pressure from 1 to 10 bar. Following compression, the stream is cooled in heat exchangers HX1, HX2, and HX3 to maintain a temperature of 25 °C.

The L47 stream, at 25 °C and 10 bar, is divided into three streams: L32, L33, and L34. These streams pass through heat exchangers HX10, HX12, and HX14, as well as turbo expanders T4, T5, and T6, where they lose pressure and temperature, preparing them to provide cooling for the hydrogen cryogenic cycle in HX9, HX11, and HX13.

Throughout this process, the Peng-Robinson equation of state is utilized within Aspen HYSYS V10 software to determine the thermodynamic characteristics of the various streams.

3.2 Ammonia-Water Absorption Refrigeration Cycle (First Scenario)

In this scenario, an Ammonia-Water Absorption Refrigeration Cycle (ABR) is incorporated to provide part of the precooling required for the hydrogen liquefaction process. The system utilizes 2000 kW of waste heat recovered from an external unit, which is directed to the generator for ammonia-water separation.

The ABR operates based on the principle of absorption refrigeration, typically consisting of an evaporator, absorber, generator, and condenser. This system relies on ammonia being absorbed into water at low pressure, followed by the release of ammonia vapor at high pressure to generate the necessary cooling effect. The ABR is particularly suitable for industrial applications where waste heat is available, making it an energy-efficient choice for large-scale refrigeration systems. The Block Flow Diagram (BFD) and the Process Flow Diagram (PFD) of this ABR-based hydrogen liquefaction process are presented in Figure 3-2 and Figure 3-3, respectively.

Process Description

In the ABR cycle, the liquid ammonia stream (W12) enters the HX6 heat exchanger at a temperature of -29.55 °C and a pressure of 1.2 bar and exits at -29.50 °C. This process provides 789.48 kW of cooling for the hydrogen precooling stage. After passing through the H17 heat exchanger, stream W13, containing both ammonia and water, enters the absorber. In the absorption process, simulated in Aspen HYSYS as Mixer M5, ammonia is absorbed into the water.

The stream (W1), containing 0.74 mol% ammonia and 0.26 mol% water, undergoes temperature and pressure adjustments before entering the generator (simulated as a distillation tower, DT) at 126.7 °C and 13 bar (stream W6). Ammonia is separated from the water in the generator, with the gaseous ammonia (stream W17) leaving the top of the distillation tower. After undergoing phase change to a liquid in heat exchanger HX16, the ammonia's temperature is reduced to -29.55 °C, and its pressure is lowered to 1.2 bar using expansion valve V1. The liquid ammonia is then directed to the HX6 heat exchanger to provide cooling in the precooling stage of the hydrogen liquefaction process. The characteristics of the streams and equipment used in this scenario are detailed in Table 3-1, Table 3-2, Table 3-3, and Table 3-4. These streams and equipment are presented in the Figure 3-3. Like for example, HX6 is the heat exchanger number 6 that precool the hydrogen by ABR cycle.

Table 3-1 Characteristics of the main streams in the ABR-based scenario

Stream	Temperature (°C)	Pressure (kPa)	Molar enthalpy (kJ/kmol)	Molar entropy (kJ/kmol °C)	Mass flow (kg/h)	Exergy (kW)
L1	25.0	700.0	-124459.3	163.8	100833.3	994814.1
L2	25.0	700.0	-121010.2	171.1	86958.8	810201.2
L3	25.0	700.0	-161438.5	85.0	13874.6	184612.9
L4	69.6	1600.0	-118732.6	171.8	86958.8	811506.7
L5	25.0	1600.0	-123476.7	156.8	86958.8	811340.6
L6	25.4	1600.0	-161329.6	85.0	13874.6	184618.4

Stream	Temperature (°C)	Pressure (kPa)	Molar enthalpy (kJ/kmol)	Molar entropy (kJ/kmol °C)	Mass flow (kg/h)	Exergy (kW)
L7	27.0	1600.0	-126706.1	150.7	100833.3	995946.4
L8	27.0	1600.0	-120790.4	164.5	71711.5	613094.1
L9	27.0	1600.0	-150858.4	94.4	29121.8	382852.2
L10	-43.0	1600.0	-129599.4	130.9	71711.5	613756.7
L11	-43.0	1600.0	-128504.1	152.8	42051.9	250363.8
L12	-43.0	1600.0	-131716.1	88.7	29659.6	363392.9
L13	-105.0	1600.0	-137147.2	61.3	29659.6	363906.3
L14	-107.7	200.0	-137239.7	61.4	29659.6	363885.4
L15	-105.0	1600.0	-136127.8	113.8	42051.9	251820.4
L16	-195.0	1600.0	-143755.2	52.1	42051.9	255726.0
L17	-196.4	200.0	-143824.7	52.2	42051.9	255689.9
L18	-110.5	200.0	-132654.2	146.3	42051.9	249559.1
L19	-106.1	200.0	-134217.7	117.5	71711.5	613411.0
L20	-47.5	200.0	-125625.4	161.8	71711.5	610877.4
L21	-45.0	1600.0	-160283.0	58.6	29121.8	383018.5
L22	-49.3	200.0	-160434.8	58.7	29121.8	382995.0
L23	-46.2	200.0	-132474.0	141.5	100833.3	993864.8
L24	11.1	200.0	-123018.6	178.4	100833.3	992798.6
L25	70.7	700.0	-119525.4	179.5	100833.3	994987.9
L26	23.5	100.0	-32.6	92.8	41804.6	87029.2
L27	138.8	215.4	2420.3	93.4	41804.6	91801.5
L28	25.0	215.4	-1.0	86.5	41804.6	91024.2
L29	140.8	464.2	2464.3	87.1	41804.6	95822.7
L30	25.0	464.2	-2.2	80.1	41804.6	95019.3
L31	140.8	1000.0	2463.3	80.7	41804.6	99818.1
L32	25.0	1000.0	-4.6	73.7	8151.9	19307.8
L33	25.0	1000.0	-4.6	73.7	20693.3	49012.2

Stream	Temperature (°C)	Pressure (kPa)	Molar enthalpy (kJ/kmol)	Molar entropy (kJ/kmol °C)	Mass flow (kg/h)	Exergy (kW)
L34	25.0	1000.0	-4.6	73.7	12959.4	30694.5
L35	23.9	100.0	-23.8	92.8	12959.4	26979.0
L36	23.4	100.0	-35.3	92.8	20693.3	43079.5
L37	23.2	100.0	-39.5	92.8	8151.9	16970.7
L38	-194.0	1000.0	-4676.4	45.4	8151.9	20851.9
L39	-236.5	100.0	-5562.7	48.3	8151.9	20138.5
L40	-196.5	100.0	-4711.3	64.0	8151.9	18569.2
L41	-219.0	1000.0	-5216.4	37.2	20693.3	54912.1
L42	-248.2	100.0	-5813.1	40.0	20693.3	53412.2
L43	-221.7	100.0	-5247.1	55.5	20693.3	49207.5
L44	-245.0	1000.0	-5792.6	22.7	12959.4	36835.8
L45	-255.0	100.0	-6128.0	24.8	12959.4	36208.0
L46	-248.2	100.0	-5811.9	40.1	12959.4	33441.6
L47	25.0	1000.0	-4.6	73.7	41804.6	99014.6
L48	24.0	101.1	-285672.3	55.2	60153.9	10861.3
L49	99.0	101.1	-280190.8	71.6	60153.9	11397.9
L50	24.0	101.1	-285672.3	55.2	61276.5	11064.0
L51	99.0	101.1	-280190.8	71.6	61276.5	11610.6
L52	24.0	101.1	-285672.3	55.2	61309.3	11069.9
L53	99.0	101.1	-280190.8	71.6	61309.3	11616.8
L54	24.0	101.1	-285672.3	55.2	143763.8	25957.8
L55	45.0	101.1	-284143.8	60.2	143763.8	26061.0
L56	24.0	101.1	-285672.3	55.2	102123.8	18439.3
L57	50.0	101.1	-283779.9	61.3	102123.8	18552.8
H1	25.0	2100.0	8475.5	116.9	4166.7	141251.6
H2	-45.0	2100.0	6472.0	109.2	4166.7	141411.6
H3	-105.0	2100.0	4822.9	100.9	4166.7	141898.4

Stream	Temperature (°C)	Pressure (kPa)	Molar enthalpy (kJ/kmol)	Molar entropy (kJ/kmol °C)	Mass flow (kg/h)	Exergy (kW)
H4	-195.0	2100.0	2579.5	81.9	4166.7	143853.9
H5	-195.0	2100.0	2291.9	81.8	4166.6	143156.1
H7	-195.0	2100.0	2291.9	81.8	4166.6	143156.2
H8	-219.0	2100.0	1684.8	72.5	4166.6	144402.0
H9	-239.5	2100.0	660.2	47.3	4166.6	148118.3
H10	-240.0	2100.0	-120.6	28.4	4166.4	147975.8
H12	-240.0	2100.0	-120.6	28.4	4166.4	149483.0
H13	-253.0	2100.0	-479.0	15.2	4166.4	151540.9
H14	-253.5	130.0	-528.2	15.5	4166.4	151464.5
H16	-253.5	130.0	-528.2	15.5	4166.4	151464.5
W1	54.1	120.0	-225213.2	80.6	14356.9	21783.8
W2	31.9	120.0	-230824.9	62.9	14356.9	21713.3
W3	25.0	200.0	-285010.9	6.6	217182.2	39220.1
W4	30.0	190.0	-284634.6	7.9	217182.2	39229.9
W5	32.0	1300.0	-230796.6	62.9	14356.9	21719.5
W6	126.7	1300.0	-222020.6	87.5	14356.9	22038.7
W7	104.2	1300.0	-55230.4	159.0	3869.5	20614.8
W8	37.0	1300.0	-271521.7	59.2	11485.5	5862.2
W9	37.3	120.0	-271521.7	59.2	11485.5	5857.8
W10	34.0	1300.0	-66320.8	83.9	2871.4	16224.7
W11	-24.5	1300.0	-71072.1	66.7	2871.4	16241.2
W12	-29.6	120.0	-71072.1	66.9	2871.4	16239.0
W13	-29.5	120.0	-54214.6	136.1	2871.4	16062.3
W14	154.9	1300.0	-248032.3	87.1	14754.1	12917.7
W15	25.0	200.0	-285010.9	6.6	164951.3	29787.9
W16	30.0	190.0	-284634.6	7.9	164951.3	29795.4
W17	45.5	1300.0	-45883.0	150.3	2871.4	16253.6

Stream	Temperature (°C)	Pressure (kPa)	Molar enthalpy (kJ/kmol)	Molar entropy (kJ/kmol °C)	Mass flow (kg/h)	Exergy (kW)
W18	173.9	1300.0	-260433.7	88.7	11485.5	6268.0
W19	-29.3	120.0	-49463.3	155.6	2871.4	16012.6

Table 3-2 Characteristics of the main stream compositions in the ABR-based scenario (%)

Stream	CH_4	C_2H_6	n-Butane	H_2	N_2	C_3H_8	He	n-Pentane	Refrig-14	Ethylene	Ne	H_2O
L1	0.17	0.07	0.02	0.01	0.16	0.18	0.00	0.15	0.08	0.16	0.00	0.00
L2	0.19	0.08	0.02	0.01	0.17	0.18	0.00	0.09	0.09	0.17	0.00	0.00
L3	0.01	0.02	0.04	0.00	0.00	0.13	0.00	0.77	0.01	0.03	0.00	0.00
L4	0.19	0.08	0.02	0.01	0.17	0.18	0.00	0.09	0.09	0.17	0.00	0.00
L5	0.19	0.08	0.02	0.01	0.17	0.18	0.00	0.09	0.09	0.17	0.00	0.00
L6	0.01	0.02	0.04	0.00	0.00	0.13	0.00	0.77	0.01	0.03	0.00	0.00
L7	0.17	0.07	0.02	0.01	0.16	0.18	0.00	0.15	0.08	0.16	0.00	0.00
L8	0.21	0.08	0.01	0.01	0.20	0.17	0.00	0.04	0.10	0.19	0.00	0.00
L9	0.02	0.03	0.05	0.00	0.01	0.23	0.00	0.59	0.01	0.06	0.00	0.00
L10	0.21	0.08	0.01	0.01	0.20	0.17	0.00	0.04	0.10	0.19	0.00	0.00
L11	0.29	0.06	0.00	0.02	0.29	0.04	0.00	0.00	0.12	0.18	0.00	0.00
L12-14	0.05	0.12	0.03	0.00	0.01	0.42	0.00	0.12	0.05	0.20	0.00	0.00
L15-18	0.29	0.06	0.00	0.02	0.29	0.04	0.00	0.00	0.12	0.18	0.00	0.00
L19	0.21	0.08	0.01	0.01	0.20	0.17	0.00	0.04	0.10	0.19	0.00	0.00
L20	0.21	0.08	0.01	0.01	0.20	0.17	0.00	0.04	0.10	0.19	0.00	0.00
L21	0.02	0.03	0.05	0.00	0.01	0.23	0.00	0.59	0.01	0.06	0.00	0.00
L22	0.02	0.03	0.05	0.00	0.01	0.23	0.00	0.59	0.01	0.06	0.00	0.00
L23-25	0.17	0.07	0.02	0.01	0.16	0.18	0.00	0.15	0.08	0.16	0.00	0.00
L26-45	0.00	0.00	0.00	0.06	0.00	0.00	0.84	0.00	0.00	0.00	0.10	0.00
L46	0.00	0.00	0.00	0.02	0.00	0.00	0.61	0.00	0.00	0.00	0.37	0.00
L47	0.00	0.00	0.00	0.06	0.00	0.00	0.84	0.00	0.00	0.00	0.10	0.00
L48-57	0.00	0.00	0.00	0.00	0.00	0.00	0.00	0.00	0.00	0.00	0.00	1.00

Table 3-3 Characteristics of the main stream compositions in the ABR-based scenario (%)

Stream	Hydrogen	p-Hydrogen	H_2O	Ammonia
H1-4	1.00	0.00	0.00	0.00
H5-9	0.72	0.28	0.00	0.00
H10-16	0.00	1.00	0.00	0.00
W1	0.00	0.00	0.74	0.26
W2	0.00	0.00	0.74	0.26
W3	0.00	0.00	1.00	0.00
W4	0.00	0.00	1.00	0.00
W5	0.00	0.00	0.75	0.25
W6	0.00	0.00	0.75	0.25
W7	0.00	0.00	0.06	0.94
W8	0.00	0.00	0.93	0.07
W9	0.00	0.00	0.93	0.07
W10-13	0.00	0.00	0.00	1.00
W14	0.00	0.00	0.87	0.13
W15	0.00	0.00	1.00	0.00
W16	0.00	0.00	1.00	0.00
W17	0.00	0.00	0.00	1.00
W18	0.00	0.00	0.93	0.07
W19	0.00	0.00	0.00	1.00

Table 3-4 Characteristics of the main equipment used in the ABR-based scenario

Equipment	Pressure head [m]	Velocity head [m]	Total Power [kW]	Delta P [kPa]	Pressure ratio
P1	151.93	0.00	6.38	900.00	2.29
P2	138.09	0.00	6.35	1180.00	10.83

Equipment	Valve Opening [%]	Delta P [kPa]	Flow Rate [kg/h]	Inlet Pressure [bar]	Molecular Weight
V1	50.00	1180.00	2871.38	13.00	17.03
V2	50.00	1180.00	11485.49	13.00	17.95

Equipment	Isentropic Efficiency [%]	Polytropic Efficiency [%]	Power Produced [kW]	Delta P [kPa]	Pressure ratio
T1	90.00	89.81	20.52	1400.00	0.13
T2	90.00	89.78	17.39	1400.00	0.13

Equipment	Isentropic Efficiency [%]	Polytropic Efficiency [%]	Power Produced [kW]	Delta P [kPa]	Pressure ratio
T3	90.00	89.77	25.24	1400.00	0.13
T4	90.00	84.84	362.86	900.00	0.10
T5	90.00	84.84	620.19	900.00	0.10
T6	90.00	87.34	218.29	900.00	0.10
T7	90.00	89.88	28.24	1970.00	0.06

Equipment	Adiabatic Efficiency [%]	Polytropic Efficiency [%]	Power Consumed [kW]	Delta P [kPa]	Pressure ratio
C1	90.00	90.80	2398.90	500.00	3.50
C2	90.00	90.61	1430.62	900.00	2.29
C3	90.00	91.35	5150.43	115.44	2.15
C4	90.00	91.35	5176.67	248.72	2.15
C5	90.00	91.35	5176.89	535.84	2.15

Equipment	Vessel Volume [m3]	Vessel Diameter [m]	Height [m]	Liq. Volume Percent [%]	Vessel Pressure [bar]
D1	0.98	0.61	3.35	50.00	7.00
D2	0.98	0.61	3.35	50.00	16.00
D3	0.98	0.61	3.35	50.00	16.00

Equipment	Number of stages	Reb/Cond. Pressure [bar]	Tray/Packed Space [m]	Tray/Packed Volume [m3]	Diameter [m]
DT	6.00	13.00	0.55	0.97	1.50

Equipment	UA [MJ/^{0}Ch]	Min. Approach	LMTD [^{0}C]	Duty [kW]	Cold Pinch Temp. [^{0}C]
HX1	1748.55	1.00	10.47	5084.22	24.00
HX2	1715.56	1.00	10.87	5179.10	24.00
HX3	1722.16	1.00	10.83	5181.87	24.00
HX4	4571.54	1.00	2.67	3388.29	24.00
HX5	2967.33	1.00	3.62	2979.94	24.00
HX6	5637.63	1.18	4.65	7282.84	-46.18
HX7	8742.86	1.09	1.95	4739.74	-106.09
HX8	4615.16	1.38	3.17	4060.85	-196.38
HX9	196.36	1.53	6.39	348.57	-196.53

Equipment	UA [MJ/^{0}Ch]	Min. Approach	LMTD [^{0}C]	Duty [kW]	Cold Pinch Temp. [^{0}C]
HX10	3374.40	1.83	2.04	1912.92	23.17
HX11	1127.93	0.80	1.88	588.23	-229.88
HX12	10282.42	1.64	1.90	5417.05	23.36
HX13	128.07	2.00	5.78	205.74	-255.00
HX14	335.10	6.91	13.54	1260.24	25.00
HX15	335.10	6.91	13.54	1260.24	25.00
HX16	476.41	5.14	7.23	957.16	29.00
HX17	34.04	5.00	23.53	222.51	-29.50
HX18	447.27	5.00	15.86	1970.82	32.00

Equipment	Duty [kW]	Liquid level [%]	Feed Delta P [kPa]	Vessel Pressure [bar]	Reaction Heat [kJ/kgmole]
CR1	-165.09	50.00	0.00	21.00	58.00
CR2		50.00	0.00	21.00	58.00

3.3 Diffusion-Absorption Refrigeration Cycle (Second Scenario)

In this scenario, a Diffusion-Absorption Refrigeration Cycle (DAR) is utilized to support the precooling stage of the hydrogen liquefaction process. The DAR cycle operates based on the principle of absorption refrigeration, enhanced by a diffusion process. In this design, the refrigerant gas—helium—diffuses through a porous medium to mix with an absorbent solution, typically water-ammonia. The diffusion process facilitates the absorption of the refrigerant into the solution, enhancing the system's overall efficiency.

The Block Flow Diagram (BFD) and the Process Flow Diagram (PFD) for this DAR process are illustrated in, Figure 3-4 and Figure 3-5 respectively. In this design, the DAR system uses water, ammonia, and helium as working fluids and includes two critical subsystems: DT1 and DT2 distillation columns, which serve as the core components for heat management in the process.

The DT2 column acts as the generator, reservoir, and bubble pump. The system operates without mechanical pumps due to a single-pressure configuration, relying on the thermosyphon effect, significantly improving energy efficiency and system reliability. This setup assumes that 2000 kW of waste heat, recovered from an external source, is used to drive the generator in DT2.

Process Description

- Heat Exchange and Vaporization:

Stream B15, a concentrated ammonia-water solution, enters the DT2 column, where it is pre-heated by a weaker ammonia-water solution from the bubble pump output. The heat input vaporizes the ammonia, producing a vapor mixture of ammonia and water.

- Separation in the Rectifier:

The rectifier in DT2 condenses the ammonia vapor, separating it into pure ammonia vapor (Stream B1), while water condensate is returned to the generator via gravity. This ammonia vapor undergoes a phase change to liquid, releasing heat through an exothermic process.

- Precooling with Helium:

After cooling to 2.0 °C via heat exchangers HX17 and HX15, the liquid ammonia (Stream B1) is mixed with helium (Stream B4). The mixture (Stream B7) enters the HX6 heat exchanger at -31.7 °C and 25.0 bar, providing 978.9 kW of cooling to precool the hydrogen during liquefaction. Stream B8 leaves HX6 at -5.85 °C and then passes through HX15 before entering DT1 at 24.05 °C.

- Absorption in DT1:

The absorber in DT1 receives Stream B10 (a pre-heated ammonia-helium mixture from HX15) and mixes it with Stream B9 (a pre-cooled weak ammonia-water solution from HX16). This forms a strong ammonia-water liquid solution (Stream B12), which exits the absorber while releasing heat to the environment.

- Helium Recovery:

Helium is extracted from the top of DT1 and the D5 drum (Streams B11 and B14), and these are collected in the M8 mixer for recirculation in the cycle.

Summary of Equipment and Stream Characteristics

The detailed characteristics of the streams and equipment involved in this DAR-based process are presented in Table 3-5, Table 3-6, Table 3-7, and Table 3-8. The system is simulated using the Peng-Robinson equation of state in Aspen HYSYS V10 to determine the thermodynamic properties of the streams, ensuring accurate modeling of the hydrogen liquefaction process. These streams and equipment are presented in the Figure 3-5. Like for example, HX6 is the heat exchanger number 6 that precool the hydrogen by DAR cycle.

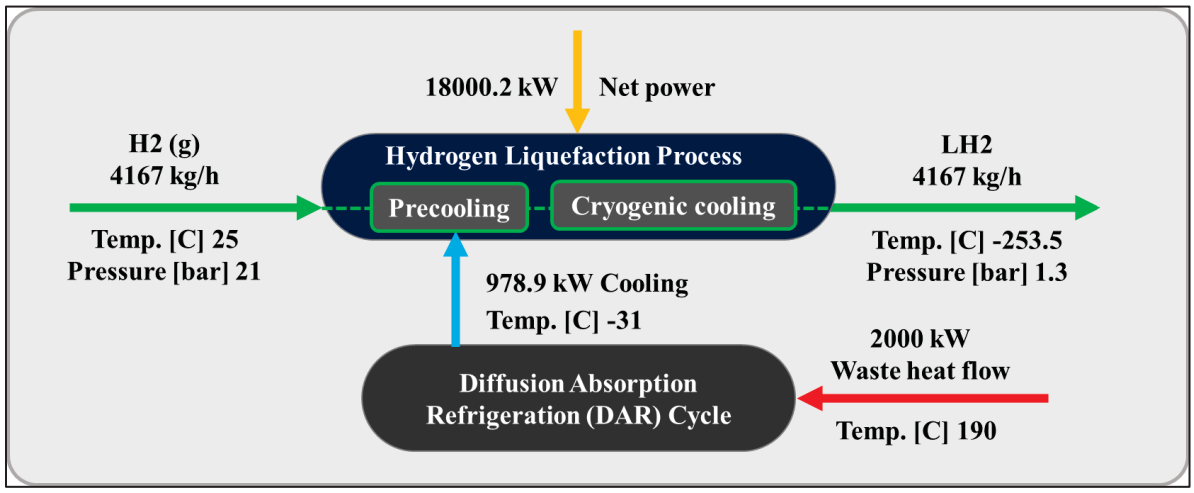

Figure 3-4 Block Flow Diagram (BFD) of the hydrogen liquefaction process by the implementation of the Diffusion Absorption Refrigeration Cycle

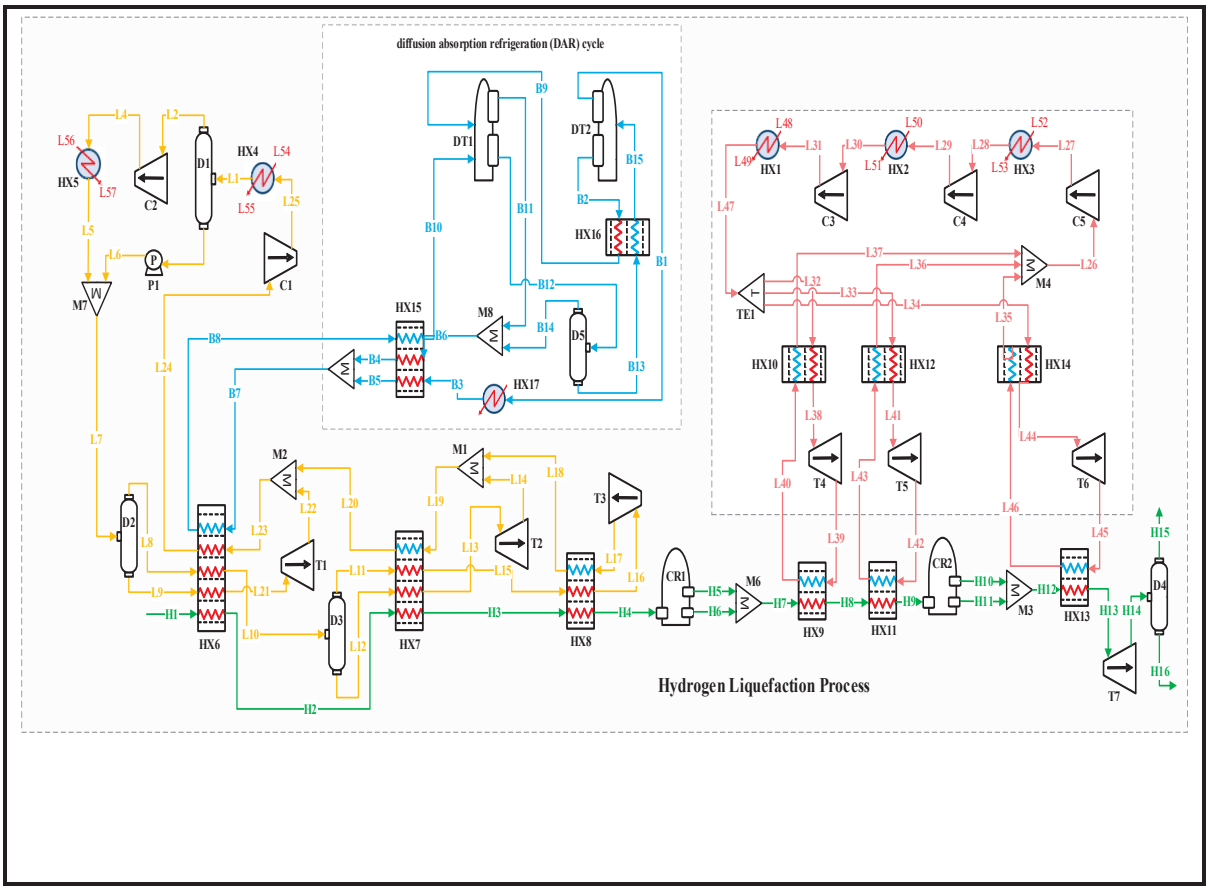

Figure 3-5 Process Flow Diagram (PFD) of the hydrogen liquefaction process by the implementation of the Diffusion Absorption Refrigeration Cycle

Table 3-5 Characteristics of the main stream characteristics in the DAR-based scenario

Stream	Temperature (°C)	Pressure (kPa)	Molar enthalpy (kJ/kmol)	Molar entropy (kJ/kmol °C)	Mass flow (kg/h)	Exergy (kW)
L1	25.0	700.0	-124459.3	163.8	100833.3	994814.1
L2	25.0	700.0	-121010.2	171.1	86958.8	810201.2
L3	25.0	700.0	-161438.5	85.0	13874.6	184612.9
L4	69.6	1600.0	-118732.6	171.8	86958.8	811506.7
L5	25.0	1600.0	-123476.7	156.8	86958.8	811340.6
L6	25.4	1600.0	-161329.6	85.0	13874.6	184618.4
L7	27.0	1600.0	-126706.1	150.7	100833.3	995946.4
L8	27.0	1600.0	-120790.4	164.5	71711.5	613094.1
L9	27.0	1600.0	-150858.4	94.4	29121.8	382852.2
L10	-43.0	1600.0	-129599.4	130.9	71711.5	613756.7
L11	-43.0	1600.0	-128504.1	152.8	42051.9	250363.8

Stream	Temperature (°C)	Pressure (kPa)	Molar enthalpy (kJ/kmol)	Molar entropy (kJ/kmol °C)	Mass flow (kg/h)	Exergy (kW)
L12	-43.0	1600.0	-131716.1	88.7	29659.6	363392.9
L13	-105.0	1600.0	-137147.2	61.3	29659.6	363906.3
L14	-107.7	200.0	-137239.7	61.4	29659.6	363885.4
L15	-105.0	1600.0	-136127.8	113.8	42051.9	251820.4
L16	-195.0	1600.0	-143755.2	52.1	42051.9	255726.0
L17	-196.4	200.0	-143824.7	52.2	42051.9	255689.9
L18	-110.5	200.0	-132654.2	146.3	42051.9	249559.1
L19	-106.1	200.0	-134217.7	117.5	71711.5	613411.0
L20	-47.5	200.0	-125625.4	161.8	71711.5	610877.4
L21	-45.0	1600.0	-160283.0	58.6	29121.8	383018.5
L22	-49.3	200.0	-160434.8	58.7	29121.8	382995.0
L23	-46.2	200.0	-132474.0	141.5	100833.3	993864.8
L24	6.4	200.0	-123294.4	177.5	100833.3	992809.5
L25	65.8	700.0	-119860.8	178.5	100833.3	994958.8
L26	23.1	100.0	-40.1	92.8	41804.6	87029.3
L27	138.3	215.4	2410.0	93.4	41804.6	91795.5
L28	25.0	215.4	-1.0	86.5	41804.6	91024.2
L29	140.8	464.2	2464.3	87.1	41804.6	95822.7
L30	25.0	464.2	-2.2	80.1	41804.6	95019.3
L31	140.8	1000.0	2463.3	80.7	41804.6	99818.1
L32	25.0	1000.0	-4.6	73.7	8151.9	19307.8
L33	25.0	1000.0	-4.6	73.7	20693.3	49012.2
L34	25.0	1000.0	-4.6	73.7	12959.4	30694.5
L35	23.9	100.0	-23.8	92.8	12959.4	26979.0
L36	22.6	100.0	-50.5	92.7	20693.3	43079.6
L37	23.2	100.0	-39.5	92.8	8151.9	16970.7
L38	-194.0	1000.0	-4676.4	45.4	8151.9	20851.9
L39	-236.5	100.0	-5562.7	48.3	8151.9	20138.5
L40	-196.5	100.0	-4711.3	64.0	8151.9	18569.2
L41	-219.0	1000.0	-5216.4	37.2	20693.3	54912.1
L42	-248.2	100.0	-5813.1	40.0	20693.3	53412.2
L43	-222.4	100.0	-5262.3	55.2	20693.3	49283.9
L44	-245.0	1000.0	-5792.6	22.7	12959.4	36835.8
L45	-255.0	100.0	-6128.0	24.8	12959.4	36208.0
L46	-248.2	100.0	-5811.9	40.1	12959.4	33441.6
L47	25.0	1000.0	-4.6	73.7	41804.6	99014.6
L48	24.0	101.1	-285672.3	55.2	59897.8	10815.0
L49	99.0	101.1	-280190.8	71.6	59897.8	11349.3

Stream	Temperature (°C)	Pressure (kPa)	Molar enthalpy (kJ/kmol)	Molar entropy (kJ/kmol °C)	Mass flow (kg/h)	Exergy (kW)
L50	24.0	101.1	-285672.3	55.2	61276.5	11064.0
L51	99.0	101.1	-280190.8	71.6	61276.5	11610.6
L52	24.0	101.1	-285672.3	55.2	61309.3	11069.9
L53	99.0	101.1	-280190.8	71.6	61309.3	11616.8
L54	24.0	101.1	-285672.3	55.2	133990.4	24193.1
L55	45.0	101.1	-284143.8	60.2	133990.4	24289.3
L56	24.0	101.1	-285672.3	55.2	102123.8	18439.3
L57	50.0	101.1	-283779.9	61.3	102123.8	18552.8
H1	25.0	2100.0	8475.5	116.9	4166.7	141251.6
H2	-45.0	2100.0	6472.0	109.2	4166.7	141411.6
H3	-105.0	2100.0	4822.9	100.9	4166.7	141898.4
H4	-195.0	2100.0	2579.5	81.9	4166.7	143853.9
H5	-195.0	2100.0	2291.9	81.8	4166.6	143156.1
H7	-195.0	2100.0	2291.9	81.8	4166.6	143156.2
H8	-219.0	2100.0	1684.8	72.5	4166.6	144402.0
H9	-239.0	2100.0	687.7	48.1	4166.6	147995.2
H10	-240.0	2100.0	-82.8	30.3	4166.4	147737.2
H12	-240.0	2100.0	-82.8	30.4	4166.4	149242.0
H13	-253.0	2100.0	-441.2	17.1	4166.4	151299.8
H14	-253.5	130.0	-490.4	17.4	4166.4	151223.5
H16	-253.5	130.0	-490.4	17.4	4166.4	151223.5
B1	65.3	2500.0	-45671.5	145.8	2999.3	17038.4
B2	188.5	2500.0	-243856.7	93.8	8927.4	8217.1
B3	35.0	2500.0	-66040.8	84.1	2999.3	16941.9
B4	-3.1	2500.0	-1574.4	57.3	10285.3	29030.7
B5	2.0	2500.0	-68794.1	74.7	2999.3	16945.0
B6	22.3	2500.0	-992.8	59.3	10285.3	29009.3
B7	-31.7	2500.0	-6108.0	58.8	13284.7	45900.9
B8	-5.8	2500.0	-4761.2	64.2	13284.7	45717.0
B9	43.0	2500.0	-255907.2	62.6	8927.4	7837.3
B10	24.1	2500.0	-4033.1	66.8	13284.7	45686.8
B11	22.3	2500.0	-992.8	59.3	10285.2	29008.8
B12	25.3	2500.0	-209227.5	63.6	11927.4	24492.9
B13	21.8	2500.0	-209511.7	62.7	11927.3	24492.7
B14	21.8	2500.0	-3383.5	65.3	0.2	0.5
B15	128.0	2500.0	-200608.3	88.3	11927.3	24728.0

Table 3-6 Characteristics of the main stream compositions in the DAR-based scenario (%)

Stream	CH_4	C_2H_6	n-Butane	H_2	N_2	C_3H_8	He	n-Pentane	Refrig-14	Ethylene	Ne	H_2O
L1	0.17	0.07	0.02	0.01	0.16	0.18	0.00	0.15	0.08	0.16	0.00	0.00
L2	0.19	0.08	0.02	0.01	0.17	0.18	0.00	0.09	0.09	0.17	0.00	0.00
L3	0.01	0.02	0.04	0.00	0.00	0.13	0.00	0.77	0.01	0.03	0.00	0.00
L4	0.19	0.08	0.02	0.01	0.17	0.18	0.00	0.09	0.09	0.17	0.00	0.00
L5	0.19	0.08	0.02	0.01	0.17	0.18	0.00	0.09	0.09	0.17	0.00	0.00
L6	0.01	0.02	0.04	0.00	0.00	0.13	0.00	0.77	0.01	0.03	0.00	0.00
L7	0.17	0.07	0.02	0.01	0.16	0.18	0.00	0.15	0.08	0.16	0.00	0.00
L8	0.21	0.08	0.01	0.01	0.20	0.17	0.00	0.04	0.10	0.19	0.00	0.00
L9	0.02	0.03	0.05	0.00	0.01	0.23	0.00	0.59	0.01	0.06	0.00	0.00
L10	0.21	0.08	0.01	0.01	0.20	0.17	0.00	0.04	0.10	0.19	0.00	0.00
L11	0.29	0.06	0.00	0.02	0.29	0.04	0.00	0.00	0.12	0.18	0.00	0.00
L12-14	0.05	0.12	0.03	0.00	0.01	0.42	0.00	0.12	0.05	0.20	0.00	0.00
L15-18	0.29	0.06	0.00	0.02	0.29	0.04	0.00	0.00	0.12	0.18	0.00	0.00
L19	0.21	0.08	0.01	0.01	0.20	0.17	0.00	0.04	0.10	0.19	0.00	0.00
L20	0.21	0.08	0.01	0.01	0.20	0.17	0.00	0.04	0.10	0.19	0.00	0.00
L21	0.02	0.03	0.05	0.00	0.01	0.23	0.00	0.59	0.01	0.06	0.00	0.00
L22	0.02	0.03	0.05	0.00	0.01	0.23	0.00	0.59	0.01	0.06	0.00	0.00
L23-25	0.17	0.07	0.02	0.01	0.16	0.18	0.00	0.15	0.08	0.16	0.00	0.00
L26-45	0.00	0.00	0.00	0.06	0.00	0.00	0.84	0.00	0.00	0.00	0.10	0.00
L46	0.00	0.00	0.00	0.02	0.00	0.00	0.61	0.00	0.00	0.00	0.37	0.00
L47	0.00	0.00	0.00	0.06	0.00	0.00	0.84	0.00	0.00	0.00	0.10	0.00
L48-57	0.00	0.00	0.00	0.00	0.00	0.00	0.00	0.00	0.00	0.00	0.00	1.00

Table 3-7 Characteristics of the main stream compositions in the DAR-based scenario (%)

Stream	Hydrogen	p-Hydrogen	Helium	Ammonia	H2O
B1	0.00	0.00	0.00	1.00	0.00
B2	0.00	0.00	0.00	0.14	0.86
B3	0.00	0.00	0.00	1.00	0.00
B4	0.00	0.00	0.98	0.02	0.00
B5	0.00	0.00	0.00	1.00	0.00

Stream	Hydrogen	p-Hydrogen	Helium	Ammonia	H2O
B6	0.00	0.00	0.98	0.02	0.00
B7	0.00	0.00	0.92	0.08	0.00
B8	0.00	0.00	0.92	0.08	0.00
B9	0.00	0.00	0.00	0.14	0.86
B10	0.00	0.00	0.92	0.08	0.00
B11	0.00	0.00	0.98	0.02	0.00
B12	0.00	0.00	0.00	0.36	0.64
B13	0.00	0.00	0.00	0.36	0.64
B14	0.00	0.00	0.93	0.07	0.00
B15	0.00	0.00	0.00	0.36	0.64
H1-4	1.00	0.00	0.00	0.00	0.00
H5-9	0.72	0.28	0.00	0.00	0.00
H10-16	0.04	0.96	0.00	0.00	0.00

Table 3-8 Characteristics of the main equipment used in the DAR-based scenario

Equipment	UA [MJ/Ch]	Min. Approach	LMTD [^{0}C]	Duty [kW]	Cold Pinch Temp. [^{0}C]
HX1	1757.41	1.00	10.37	5062.57	24.00
HX2	1715.56	1.00	10.87	5179.10	24.00
HX3	1722.16	1.00	10.83	5181.87	24.00
HX4	5788.40	1.00	1.96	3157.95	24.00
HX5	2967.33	1.00	3.62	2979.94	24.00
HX6	5834.60	1.18	4.49	7282.84	-46.18
HX7	8742.23	1.09	1.95	4739.74	-106.09
HX8	4615.07	1.38	3.17	4060.85	-196.38
HX9	196.36	1.53	6.39	348.57	-196.53
HX10	3374.40	1.83	2.04	1912.92	23.17
HX11	740.52	1.52	2.78	572.43	-230.36
HX12	7444.56	2.35	2.62	5417.05	22.65
HX13	128.07	2.00	5.78	205.74	-255.00
HX14	9580.95	1.10	1.42	3767.58	23.90
HX15	784.60	1.16	2.43	529.17	21.22
HX16	160.73	21.17	37.44	1671.42	21.83

Equipment	Number of stages	Reb./Cond. Pressure [bar]	Tray/Packed Space [m]	Tray/Packed Volume [m^3]	Diameter [m]
DT1	4.00	25.00	0.50	0.88	1.50

Equipment	Number of stages	Reb./Cond. Pressure [bar]	Tray/Packed Space [m]	Tray/Packed Volume [m^3]	Diameter [m]
DT2	4.00	25.00	0.55	0.97	1.50

Equipment	Pressure head [m]	Velocity head [m]	Total Power [kW]	Delta P [kPa]	Pressure ratio
P1	151.93	0.00	6.38	900.00	2.29

Equipment	Vessel Volume [m^3]	Vessel Diameter [m]	Height [m]	Liq. Volume [%]	Vessel Pressure [bar]
D1	0.98	0.61	3.35	50.00	7.00
D2	0.98	0.61	3.35	50.00	16.00
D3	0.98	0.61	3.35	50.00	16.00

Equipment	Adiabatic Efficiency [%]	Polytropic Efficiency [%]	Power Consumed [kW]	Delta P [kPa]	Pressure ratio
C1	90.00	90.81	2358.28	500.00	3.50
C2	90.00	90.61	1430.62	900.00	2.29
C3	90.00	91.35	5144.37	115.44	2.15
C4	90.00	91.35	5176.67	248.72	2.15
C5	90.00	91.35	5176.89	535.84	2.15

Equipment	Isentropic Efficiency [%]	Polytropic Efficiency [%]	Power Produced [kW]	Delta P [kPa]	Pressure ratio
T1	90.00	89.81	20.52	1400.00	0.13
T2	90.00	89.78	17.39	1400.00	0.13
T3	90.00	89.77	25.24	1400.00	0.13
T4	90.00	84.84	362.86	900.00	0.10
T5	90.00	84.84	620.19	900.00	0.10
T6	90.00	87.34	218.29	900.00	0.10
T7	90.00	89.88	28.24	1970.00	0.06

3.4 Combination of Organic Rankine Cycle and Kalina power cycle (Third Scenario)

In this scenario, the Organic Rankine Cycle (ORC) and Kalina Power Cycle are integrated into the hydrogen liquefaction process to recover 2000 kW of waste heat, which generates power for the precooling stage. These two thermodynamic cycles efficiently convert the recovered heat into mechanical work, which is then converted into electrical energy to supply part of the energy required for liquefaction. The Block Flow Diagram (BFD) and Process Flow Diagram (PFD) of the ORC and Kalina Power Cycle process are illustrated in Figure 3-6 and Figure 3-7, respectively.

Organic Rankine Cycle (ORC) Description

The Organic Rankine Cycle (ORC) utilizes Refrig-290 as the working fluid. ORC systems are adequate for recovering energy from low- to medium-temperature heat sources because they use organic fluids with lower boiling points than water.

- Heat Absorption:

In this process, the stream R1, at a temperature of 30.0°C and a pressure of 25.0 bar, enters the HX16 heat exchanger and absorbs 2000 kW of heat, leaving at a temperature of 178.7°C (stream R2).

- Power Generation:

The stream R2 is split into R3 and R5, which enter turbines T8 and T9, respectively, for power generation. Turbine T8 decreases the pressure of the stream to 15.0 bar, generating 220.1 kW of power. Similarly, Turbine T9 generates 21.77 kW of power by reducing the pressure of stream R5.

- Heat Transfer to Kalina Cycle:

The external stream R4 transfers 1786.17 kW of heat to the Kalina Cycle through HX15 heat exchanger, cooling from 125.1°C to 7.23°C (stream R7).

Kalina Power Cycle Description

The Kalina Power Cycle is a variation of the Rankine Cycle, using a mixture of water and ammonia as the working fluid. This allows for better heat energy utilization, especially in cases where heat source temperatures vary.

- Ammonia-Water Solution Heating:

A rich ammonia-water solution (Stream K12) enters the D5 drum at 96.66°C and 22.9 bar. The ammonia vapor is separated and enters T10 turbine for power production.

- Power Generation:

Turbine T10 reduces the pressure from 22.8 bar (stream K13) to 4.5 bar (stream K15), generating 245.2 kW of power.

- Absorption and Pressure Recovery:

After the turbine, the ammonia vapor is absorbed into the weak ammonia-water solution (Stream K17) in the M9 mixer, forming stream K18. This stream is pumped to the working pressure of 23 bar by the P3 pump, which consumes 6.14 kW of electrical power to complete the cycle.

Energy Integration

The total net electrical power produced in this scenario partially supplies the electricity required for the precooling stage in the hydrogen liquefaction process. This integration improves the system's overall efficiency by utilizing waste heat to generate a portion of the energy needed.

Summary of Equipment and Stream Characteristics

The characteristics of the streams and equipment involved in this process are provided in Table 3-9, Table 3-10, Table 3-11, and Table 3-12. The simulation is performed using Aspen HYSYS V10 with the Peng-Robinson equation of state, ensuring accurate thermodynamic property calculations for the ORC and Kalina systems. These streams and equipment are presented in the Figure 3-7. Like for example, HX6 is the heat exchanger number 6 that precool the hydrogen.

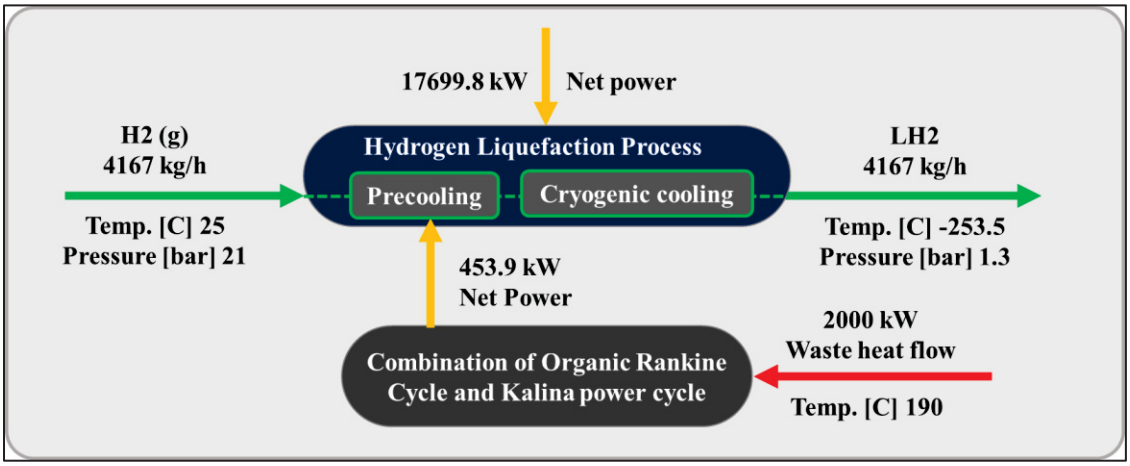

Figure 3-6 Block Flow Diagram (BFD) of the hydrogen liquefaction process by using the combination of ORC and Kalina power generation cycle

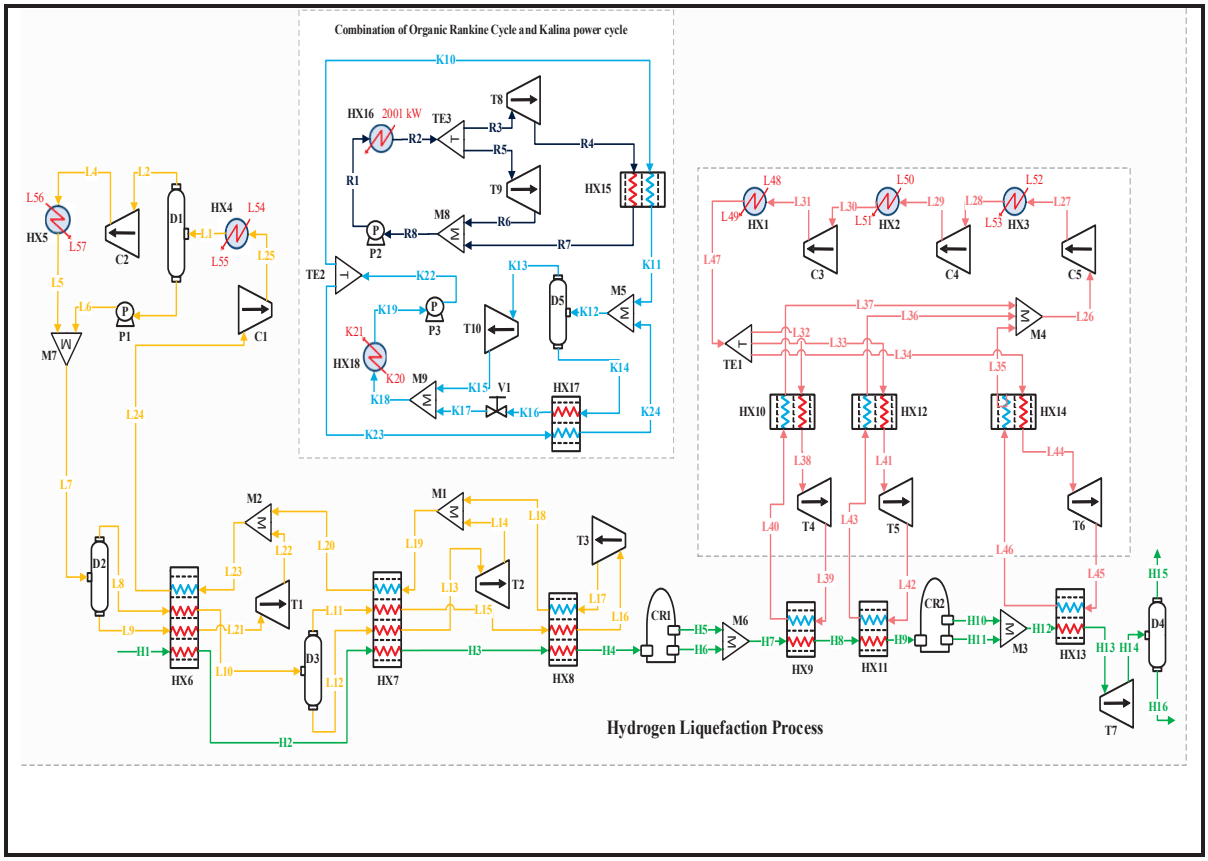

Figure 3-7 Process Flow Diagram (PFD) of the hydrogen liquefaction process by using the combination of ORC and Kalina power generation cycle

Table 3-9 Characteristics of the main stream characteristics in the ORC/Kalina-based process

Stream	Temperature (°C)	Pressure (kPa)	Molar enthalpy (kJ/kmol)	Molar entropy (kJ/kmol °C)	Mass flow (kg/h)	Exergy (kW)
L1	25.0	700.0	-124459.3	163.8	106775.5	1053439.5
L2	25.0	700.0	-121010.2	171.1	92083.3	857947.2
L3	25.0	700.0	-161438.5	85.0	14692.2	195492.3
L4	69.6	1600.0	-118732.6	171.8	92083.3	859329.6
L5	25.0	1600.0	-123476.7	156.8	92083.3	859153.7
L6	25.4	1600.0	-161329.6	85.0	14692.2	195498.2
L7	27.0	1600.0	-126706.1	150.7	106775.5	1054638.5
L8	27.0	1600.0	-120790.4	164.5	75937.5	649224.4
L9	27.0	1600.0	-150858.4	94.4	30838.0	405414.1
L10	-45.0	1600.0	-129863.2	129.8	75937.5	649972.4
L11	-45.0	1600.0	-128689.4	152.3	43520.3	254850.5

Stream	Temperature (°C)	Pressure (kPa)	Molar enthalpy (kJ/kmol)	Molar entropy (kJ/kmol °C)	Mass flow (kg/h)	Exergy (kW)
L12	-45.0	1600.0	-132006.7	88.7	32417.2	395122.0
L13	-105.0	1600.0	-137225.8	62.3	32417.2	395672.0
L14	-108.0	200.0	-137319.3	62.3	32417.2	395648.8
L15	-105.0	1600.0	-136037.8	114.5	43520.3	256329.9
L16	-195.0	1600.0	-143727.0	52.4	43520.3	260408.2
L17	-196.4	200.0	-143796.7	52.5	43520.3	260370.6
L18	-111.4	200.0	-132695.0	146.4	43520.3	253998.0
L19	-106.8	200.0	-134331.3	116.9	75937.5	649612.2
L20	-51.6	200.0	-126115.6	159.6	75937.5	646972.6
L21	-45.0	1600.0	-160283.0	58.6	30838.0	405590.1
L22	-49.3	200.0	-160434.8	58.7	30838.0	405565.2
L23	-48.8	200.0	-132867.7	139.8	106775.5	1052526.3
L24	25.7	200.0	-122144.0	181.4	106775.5	1051290.8
L25	86.1	700.0	-118468.1	182.5	106775.5	1053740.4
L26	23.1	100.0	-40.1	92.8	41804.6	87029.3
L27	138.3	215.4	2410.0	93.4	41804.6	91795.5
L28	25.0	215.4	-1.0	86.5	41804.6	91024.2
L29	140.8	464.2	2464.3	87.1	41804.6	95822.7
L30	25.0	464.2	-2.2	80.1	41804.6	95019.3
L31	140.8	1000.0	2463.3	80.7	41804.6	99818.1
L32	25.0	1000.0	-4.6	73.7	8151.9	19307.8
L33	25.0	1000.0	-4.6	73.7	20693.3	49012.2
L34	25.0	1000.0	-4.6	73.7	12959.4	30694.5
L35	23.9	100.0	-23.8	92.8	12959.4	26979.0
L36	22.6	100.0	-50.5	92.7	20693.3	43079.6
L37	23.2	100.0	-39.5	92.8	8151.9	16970.7
L38	-194.0	1000.0	-4676.4	45.4	8151.9	20851.9
L39	-236.5	100.0	-5562.7	48.3	8151.9	20138.5
L40	-196.5	100.0	-4711.3	64.0	8151.9	18569.2
L41	-219.0	1000.0	-5216.4	37.2	20693.3	54912.1
L42	-248.2	100.0	-5813.1	40.0	20693.3	53412.2
L43	-222.4	100.0	-5262.3	55.2	20693.3	49283.9
L44	-245.0	1000.0	-5792.6	22.7	12959.4	36835.8
L45	-255.0	100.0	-6128.0	24.8	12959.4	36208.0
L46	-248.2	100.0	-5811.9	40.1	12959.4	33441.6
L47	25.0	1000.0	-4.6	73.7	41804.6	99014.6
L48	24.0	101.1	-285672.3	55.2	59897.8	10815.0
L49	99.0	101.1	-280190.8	71.6	59897.8	11349.3

Stream	Temperature (°C)	Pressure (kPa)	Molar enthalpy (kJ/kmol)	Molar entropy (kJ/kmol °C)	Mass flow (kg/h)	Exergy (kW)
L50	24.0	101.1	-285672.3	55.2	61276.5	11064.0
L51	99.0	101.1	-280190.8	71.6	61276.5	11610.6
L52	24.0	101.1	-285672.3	55.2	61309.3	11069.9
L53	99.0	101.1	-280190.8	71.6	61309.3	11616.8
L54	24.0	101.1	-285672.3	55.2	149309.7	26959.1
L55	50.0	101.1	-283779.9	61.3	149309.7	27125.1
L56	24.0	101.1	-285672.3	55.2	108142.1	19526.0
L57	50.0	101.1	-283779.9	61.3	108142.1	19646.2
H1	25.0	2100.0	8475.5	116.9	4166.7	141251.6
H2	-45.0	2100.0	6472.0	109.2	4166.7	141411.6
H3	-105.0	2100.0	4822.9	100.9	4166.7	141898.4
H4	-195.0	2100.0	2579.5	81.9	4166.7	143853.9
H5	-195.0	2100.0	2291.9	81.8	4166.6	143156.1
H7	-195.0	2100.0	2291.9	81.8	4166.6	143156.2
H8	-219.0	2100.0	1684.8	72.5	4166.6	144402.0
H9	-239.0	2100.0	687.7	48.1	4166.6	147995.2
H10	-240.0	2100.0	-82.8	30.3	4166.4	147737.2
H12	-240.0	2100.0	-82.8	30.4	4166.4	149242.0
H13	-253.0	2100.0	-441.2	17.1	4166.4	151299.8
H14	-253.5	130.0	-490.4	17.4	4166.4	151223.5
H16	-253.5	130.0	-490.4	17.4	4166.4	151223.5
R1	30.0	5000.0	-120789.5	208.4	12258.7	167476.4
R2	178.7	5000.0	-94877.3	277.9	12258.7	167879.0
R3	178.7	5000.0	-94877.3	277.9	11155.4	152769.9
R4	125.1	1500.0	-98009.3	278.7	11155.4	152531.4
R5	178.7	5000.0	-94877.3	277.9	1103.3	15109.1
R6	125.1	1500.0	-98009.3	278.7	1103.3	15085.5
R7	7.2	1500.0	-123427.3	200.4	11155.4	152386.9
R8	26.6	1500.0	-121139.7	208.3	12258.7	167453.3
K1	100.0	2300.0	-89095.0	130.3	5609.0	25966.3
K2	96.7	2290.0	-89701.4	128.7	6469.2	30051.1
K3	96.5	2280.0	-47712.7	151.4	4207.0	23495.6
K4	96.5	2280.0	-169886.9	85.3	2262.2	6554.8
K5	19.5	450.0	-51289.0	152.8	4207.0	23222.4
K6	21.3	2270.0	-175754.5	67.5	2262.2	6533.9
K7	21.7	450.0	-175754.5	67.7	2262.2	6532.3
K8	28.2	450.0	-94065.1	123.6	6469.2	29753.4
K9	6.8	440.0	-108878.4	72.0	6469.2	29812.6

Stream	Temperature (°C)	Pressure (kPa)	Molar enthalpy (kJ/kmol)	Molar entropy (kJ/kmol °C)	Mass flow (kg/h)	Exergy (kW)
K10	5.5	101.3	-287022.6	50.5	70504.8	12783.3
K11	25.0	101.3	-285599.5	55.4	70504.8	12730.3
K12	7.2	2300.0	-108819.6	72.0	6469.2	29817.9
K13	7.2	2300.0	-108819.6	72.0	860.3	3965.1
K14	80.0	2290.0	-93655.0	117.7	860.3	3983.4
K15	7.2	2300.0	-108819.6	72.0	5609.0	25852.7

Table 3-10 Characteristics of the main stream compositions in the ORC/Kalina-based process (%)

Stream	CH_4	C_2H_6	n-Butane	H_2	N_2	C_3H_8	He	n-Pentane	Refrig-14	Ethylene	Ne	H_2O
L1	0.17	0.07	0.02	0.01	0.16	0.18	0.00	0.15	0.08	0.16	0.00	0.00
L2	0.19	0.08	0.02	0.01	0.17	0.18	0.00	0.09	0.09	0.17	0.00	0.00
L3	0.01	0.02	0.04	0.00	0.00	0.13	0.00	0.77	0.01	0.03	0.00	0.00
L4	0.19	0.08	0.02	0.01	0.17	0.18	0.00	0.09	0.09	0.17	0.00	0.00
L5	0.19	0.08	0.02	0.01	0.17	0.18	0.00	0.09	0.09	0.17	0.00	0.00
L6	0.01	0.02	0.04	0.00	0.00	0.13	0.00	0.77	0.01	0.03	0.00	0.00
L7	0.17	0.07	0.02	0.01	0.16	0.18	0.00	0.15	0.08	0.16	0.00	0.00
L8	0.21	0.08	0.01	0.01	0.20	0.17	0.00	0.04	0.10	0.19	0.00	0.00
L9	0.02	0.03	0.05	0.00	0.01	0.23	0.00	0.59	0.01	0.06	0.00	0.00
L10	0.21	0.08	0.01	0.01	0.20	0.17	0.00	0.04	0.10	0.19	0.00	0.00
L11	0.29	0.06	0.00	0.02	0.30	0.03	0.00	0.00	0.12	0.18	0.00	0.00
L12-14	0.05	0.12	0.03	0.00	0.01	0.41	0.00	0.12	0.05	0.20	0.00	0.00
L15-18	0.29	0.06	0.00	0.02	0.30	0.03	0.00	0.00	0.12	0.18	0.00	0.00
L19	0.21	0.08	0.01	0.01	0.20	0.17	0.00	0.04	0.10	0.19	0.00	0.00
L20	0.21	0.08	0.01	0.01	0.20	0.17	0.00	0.04	0.10	0.19	0.00	0.00
L21	0.02	0.03	0.05	0.00	0.01	0.23	0.00	0.59	0.01	0.06	0.00	0.00
L22	0.02	0.03	0.05	0.00	0.01	0.23	0.00	0.59	0.01	0.06	0.00	0.00
L23-25	0.17	0.07	0.02	0.01	0.16	0.18	0.00	0.15	0.08	0.16	0.00	0.00
L26-28	0.00	0.00	0.00	0.06	0.00	0.00	0.84	0.00	0.00	0.00	0.10	0.00
L29-45	0.00	0.00	0.00	0.06	0.00	0.00	0.84	0.00	0.00	0.00	0.10	0.00
L46	0.00	0.00	0.00	0.02	0.00	0.00	0.61	0.00	0.00	0.00	0.37	0.00
L47	0.00	0.00	0.00	0.06	0.00	0.00	0.84	0.00	0.00	0.00	0.10	0.00
L48-57	0.00	0.00	0.00	0.00	0.00	0.00	0.00	0.00	0.00	0.00	0.00	1.00

Table 3-11 Characteristics of the main stream compositions in the ORC/Kalina-based process (%)

Stream	Hydrogen	p-Hydrogen	Ammonia	H2O	Refrig-290
H1-4	1.00	0.00	0.00	0.00	0.00
H5-9	0.72	0.28	0.00	0.00	0.00
H10-16	0.04	0.96	0.00	0.00	0.00
K1	0.00	0.00	0.82	0.18	0.00
K2	0.00	0.00	0.81	0.19	0.00
K3	0.00	0.00	0.98	0.02	0.00
K4	0.00	0.00	0.52	0.48	0.00
K5	0.00	0.00	0.98	0.02	0.00
K6	0.00	0.00	0.52	0.48	0.00
K7	0.00	0.00	0.52	0.48	0.00
K8	0.00	0.00	0.82	0.18	0.00
K9	0.00	0.00	0.82	0.18	0.00
K10	0.00	0.00	0.00	1.00	0.00
K11	0.00	0.00	0.00	1.00	0.00
K12-15	0.00	0.00	0.82	0.18	0.00
R1-8	0.00	0.00	0.00	0.00	1.00

Table 3-12 Characteristics of the Equipment characteristics used in the ORC/Kalina-based process

Equipment	Adiabatic Efficiency [%]	Polytropic Efficiency [%]	Power Consumed [kW]	Delta P [kPa]	Pressure ratio
C1	90.00	90.77	2673.09	500.00	3.50
C2	90.00	90.61	1514.93	900.00	2.29
C3	90.00	91.35	5144.37	115.44	2.15
C4	90.00	91.35	5176.67	248.72	2.15
C5	90.00	91.35	5176.89	535.84	2.15

Equipment	Pressure head [m]	Velocity head [m]	Total Power [kW]	Delta P [kPa]	Pressure ratio
P1	151.93	0.00	6.76	900.00	2.29
P2	726.18	-0.02	26.94	3500.00	3.33
P3	278.79	0.00	6.14	1860.00	5.23

Equipment	Vessel Volume [m^3]	Vessel Diameter [m]	Height [m]	Liq Volume [%]	Vessel Pressure [bar]
D1	0.98	0.61	3.35	50.00	7.00
D2	0.98	0.61	3.35	50.00	16.00
D3	0.98	0.61	3.35	50.00	16.00

Equipment	Duty [kW]	Liquid level [%]	Feed Delta P [kPa]	Vessel Pressure [bar]	Reaction Heat [kJ/kgmole]
CR1	-165.09	50.00	0.00	21.00	58.00
CR2	-442.37	50.00	0.00	21.00	58.00

Equipment	Isentropic Efficiency [%]	Polytropic Efficiency [%]	Power Produced [kW]	Delta P [kPa]	Pressure ratio
T1	90.00	89.81	21.73	1400.00	0.13
T2	90.00	89.78	19.33	1400.00	0.13
T3	90.00	89.77	26.31	1400.00	0.13
T4	90.00	84.84	362.86	900.00	0.10
T5	90.00	84.84	620.19	900.00	0.10
T6	90.00	87.34	218.29	900.00	0.10
T7	90.00	89.88	28.24	1970.00	0.06
T8	90.00	89.43	220.09	3500.00	0.30
T9	90.00	89.43	21.77	3500.00	0.30
T10	90.00	88.85	245.15	1830.00	0.20

Equipment	Valve Opening [%]	Delta P [kPa]	Flow Rate [kg/h]	Inlet Pressure [bar]	Molecular Weight
V1	50.00	1820.00	2262.21	22.70	17.51

Equipment	UA [MJ/Ch]	Min. Approach	LMTD [^{0}C]	Duty [kW]	Cold Pinch Temp. [^{0}C]
HX1	1757.41	1.00	10.37	5062.57	24.00
HX2	1715.56	1.00	10.87	5179.10	24.00
HX3	1722.16	1.00	10.83	5181.87	24.00
HX4	5221.53	1.00	3.00	4356.81	24.00
HX5	3142.20	1.00	3.62	3155.55	24.00
HX6	8274.79	1.35	3.39	7798.37	25.70
HX7	5552.46	1.83	3.11	4799.07	-106.83

Equipment	UA [MJ/Ch]	Min. Approach	LMTD [^{0}C]	Duty [kW]	Cold Pinch Temp. [^{0}C]
HX8	3918.86	1.40	3.85	4190.24	-196.40
HX9	196.36	1.53	6.39	348.57	-196.53
HX10	3374.40	1.83	2.04	1912.92	23.17
HX11	741.38	1.52	2.78	572.43	-230.36
HX12	7444.56	2.35	2.62	5417.05	22.65
HX13	128.07	2.00	5.78	205.74	-255.00
HX14	9580.95	1.10	1.42	3767.58	23.90
HX15	1474.14	0.06	4.36	1786.18	7.17
HX17	49.64	14.10	15.27	210.62	7.17
HX18	2639.24	1.30	2.11	1547.17	5.50

CHAPTER 4

METHODOLOGY

4.1 Introduction to the methodology chapter

To simulate the three scenarios for the hydrogen liquefaction process, Aspen HYSYS V10 is integrated with MATLAB m-file programming. This coupling allows for the design of the complex, integrated process and enables the performance of the necessary analyses, including energy and exergy evaluations. These analyses are essential for assessing the overall process performance and its subsystems.

The Peng-Robinson equation of state is employed within Aspen HYSYS V10 to accurately determine the thermodynamic properties of the process streams, ensuring a robust representation of phase behavior and property calculations.

Assumptions in the Simulation:

1. Neglecting Kinetic and Potential Energies:
   - Kinetic and potential energy changes in the process streams are considered negligible.
   - This simplification assumes that these energy contributions are insignificant compared to the thermal and mechanical energy flows involved in the process.
2. Steady-State Heat Transfer and Stream Conditions:
   - All streams are assumed to be in a steady-state condition, meaning their properties (temperature, pressure, flow rates) remain constant over time.
3. Neglecting Pressure Drops and Heat Losses in Heat Exchangers:
   - Pressure drops and heat losses in the heat exchangers are ignored.
   - This assumes ideal behavior in heat exchangers, focusing on their thermal performance without accounting for inefficiencies due to pressure losses or external heat leakage.
4. Isentropic Efficiency for Pumps and Turbines:

- The pumps and turbines in the system are modeled using isentropic efficiency, representing the ratio of actual work to the ideal (isentropic) work.
- This ensures realistic performance modeling while simplifying mechanical work and heat interaction calculation.

4.2 Energy analysis

Energy analysis involves quantitatively assessing the inflow and outflow of energy within a system. It relies on the principles outlined in the first law of thermodynamics. The equation for steady-state control volume energy and mass balance, derived from the first law of thermodynamics, is as follows (Hutter & Wang, 2016):

$$\dot{Q}_{Cv} - \dot{W}_{Cv} + \sum \dot{m}_i \left(h_i + \frac{1}{2} v_i^2 + g z_i \right) - \sum \dot{m}_o \left(h_o + \frac{1}{2} v_o^2 + g z_o \right) = 0 \tag{4.1}$$

$$\sum \dot{m}_{in} = \sum \dot{m}_{out}$$

In which $\dot{W}_{Cv}$ is the total work, $\dot{m}$ is the mass flow rate, $\dot{Q}_{Cv}$ is the net heat transfer rate, z is the elevation from a reference position, h is the specific enthalpy, v is the stream velocity of the working fluid, and g is the gravitational acceleration. Equation (2) presents the equations delineating the energy balance in heat exchangers.

$$\dot{m}_{in,i}\left(h_{in1,i} - h_{in2,i}\right) = \dot{m}_{out,i}\left(h_{out1,i} - h_{out2,i}\right) \tag{4.2}$$

$$T_{in1,i} = T_{out1,i} + \Delta\ T_{in,HXi}$$

Isentropic efficiency is presumed within the energy balance equations governing compressors, turbines, and pumps, disregarding heat loss. Thus, the energy balance for such equipment types is formulated as follows (4.3 for compressors and pumps; 4.4 for turbines):

$$h_{out} = \frac{h_{out}^{S} - h_{in}}{\eta_s} + h_{in} \tag{4.3}$$

$$h_{out} = (h_{out}^{S} - h_{in})\eta_s + h_{in} \tag{4.4}$$

Within the mixer, energy balance and mass conservation equations are delineated as follows:

$$\dot{m}_{in,1}h_{in,1} + \dot{m}_{in,2}h_{in,2} = \dot{m}_{out}h_{out} \tag{4.5}$$

$$\dot{m}_{in,1} + \dot{m}_{in,2} = \dot{m}_{out} \tag{4.6}$$

$$h_{out} = \frac{\dot{m}_{in,1}h_{in,1} + \dot{m}_{in,2}h_{in,2}}{\dot{m}_{in,1} + \dot{m}_{in,2}} \tag{4.7}$$

In separators and flash drums, the same procedure as for the mixer can be considered:

$$\dot{m}_{in}h_{in} = \dot{m}_{out,1}h_{out,1} + \dot{m}_{out,2}h_{out,2} \tag{4.8}$$

$$\dot{m}_{in} = \dot{m}_{out,1} + \dot{m}_{out,2} \tag{4.9}$$

According to the first law of thermodynamics, the enthalpy remains unchanged during the throttling process within valves. Consequently:

$$h_{in} = h_{out} \tag{4.10}$$

The specific power consumption (SPC) and the coefficient of performance (COP) are important design parameters for assessing system performance quality. The specific power consumption of the system is calculated as follows:

$$SPC = \frac{W_{net}(kW)}{\dot{m}(kg\ hydrogen/h)} \tag{4.11}$$

The overall coefficient of performance measures the amount of cooling generated per unit of system power consumption, articulated as follows:

$$COP = \frac{\dot{m}_{feed}.h_{feed} - \dot{m}_{product}.h_{product}}{W_{net}} \quad (4.12)$$

In this equation W_{net} is the total net power used in the process, $\dot{m}_{feed}$ is feed hydrogen gas, $\dot{m}_{product}$ is the mass flow rate of the liquid hydrogen, h_{feed} is the mass enthalpy of feed gas hydrogen and $h_{product}$ is the mass enthalpy of produced liquid hydrogen.

Figure 4-1 depicts the comprehensive balance within one of its stages, used to model the distillation columns applicable across various design configurations. Each tray sees the entry and exit of both vapor and liquid streams, facilitating the representation of towers featuring multiple feeds, products, and auxiliary heat exchangers. Regarding Figure 4-1, MESH equations can be written as follows (Ebrahimi & Ziabasharhagh, 2017):

$$L_{j-1}\ x_{i,j-1} + V_{j+1}\ y_{i,j+1} + F_j\ Z_{i,j} - (L_j + U_j)\ x_{i,j} - (V_j + W_j)\ y_{i,j} = 0 \quad (4.13)$$

In this equation, j is the tray number, and i is the component number. W represents the vapor side stream, F represents the feed, L represents the liquid fraction, V represents vapor stream, and U represents the vapor fraction. The equilibrium equation for every segment within a tray of the tower is as follows:

$$y_{i,j} - k_{i,j}x_{i,j} = 0 \quad (4.14)$$

The equation representing the total for every tray is:

$$\sum_{i=1}^{NC} y_{i,j} - 1 = 0\ ,\sum_{i=1}^{NC} x_{i,j} - 1 = 0 \quad (4.15)$$

The equation describing the thermal energy balance for each tray is:

$$L_{j-1}\ H^{L}{}_{j-1} + V_{j+1}\ H^{V}{}_{j+1} + F_j\ H^{F}{}_j - (L_j + U_j)\ H^{L}{}_j - (V_j + W_j)\ H^{V}{}_j - Q_j = 0 \quad (4.16)$$

In this context, H signifies enthalpy, while Q_j is calculated according to the temperature of the heat source, denoted as T_0.

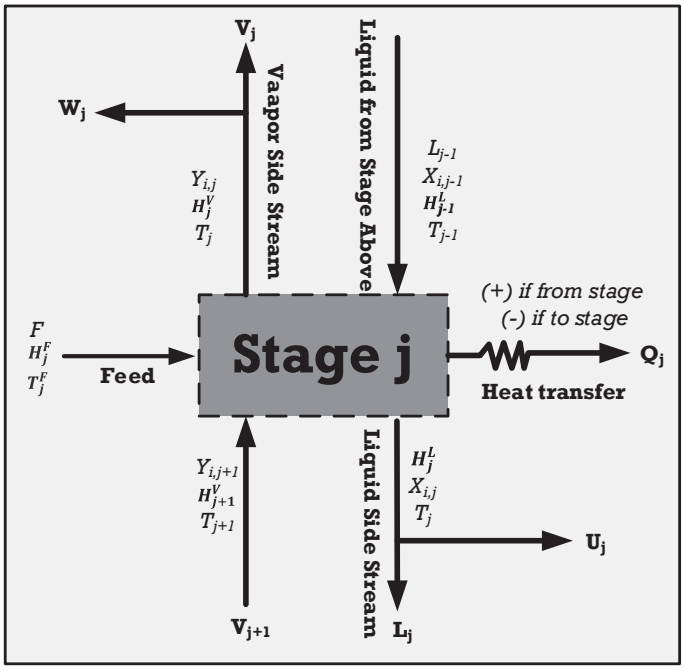

Figure 4-1 The overall balance in one of the stages of the tower, modified
Taken from Ebrahimi et al. (2017)

4.3 Exergy analysis

Exergy indicates the capacity of a unit or apparatus to generate useful work and offers valuable insights into improving system efficiency. It's utilized to gauge the conversion of energy input from equipment or a stream into useful work and the amount consumed. Exergy represents the work obtained by transitioning a system from a specific state to ambient conditions, typically defined as 25°C and 1 atm pressure in a reversible process (Ahmadi et al., 2017).

Exergy can be seen as synonymous with reversible work. Put differently, reversible work represents the maximum amount of usable work (the minimum work consumed in power-consuming equipment) during a process between initial and final conditions. Identifying exergy destruction and its locations are the primary goals of exergy analysis. The amount of exergy consumed is also termed irreversibility or exergy destruction. Hence, the exergy destruction rate is directly proportional to the entropy generated (Kotas, 2013).

$$Ex_{destroyed} = T_0 S_{gen} \geq 0 \tag{4.17}$$

It's important to highlight that exergy destruction is always positive for real systems and zero for reversible systems. When kinetic energies, potentials, nuclei, electrical, magnetic, and surface tension effects are absent, the exergy rate of an entire system can be viewed as the sum of the subsequent components (Kotas, 2013) :

$$\dot{Ex} = \dot{Ex}_{ph} + \dot{Ex}_{ch} \tag{4.18}$$

$\dot{Ex}_{ch}$ is the sum of chemical exergy rate, $\dot{Ex}$ is the exergy rate of the fluid flow, $\dot{Ex}_{ph}$ is the sum of the physical exergy rate. The rates of physical exergy and chemical exergy are determined using the following equations (Kotas, 2013) :

$$\dot{Ex}_{ph} = \sum_i \dot{n}_i \left(\left(\bar{h}_i - \bar{h}_0 \right) - T_0 (\bar{s}_i - \bar{s}_0) \right) \tag{4.19}$$

$$\dot{Ex}_{ch} = \dot{n} \left(\sum_i x_i \, \overline{ex}_i^{ch,0} + \bar{R} T_0 \sum_i x_i \ln(x_i \gamma_i) \right) \tag{4.20}$$

Here, γ_i represents the activity coefficient of the ith component, which can exceed or fall below one, being zero for an ideal mixture of various compounds. $\bar{h}_0$ and $\bar{s}_0$ denote the enthalpy and entropy of the flow at ambient temperature and pressure. In an ideal mixture, interactions between molecules are negligible, and the mixture's properties can be computed solely based on the properties of individual components and their respective proportions.

Calculating the chemical exergy of such a nonideal mixture of various compounds becomes intricate due to the presence of the activity coefficient.

It can be demonstrated that the second component of Equation (20) represents the Gibbs free energy alteration caused by the blending of diverse compounds and the creation of a solution under ambient temperature and pressure conditions. Ultimately, the chemical exergy equation undergoes the following transformation (Pourfayaz et al., 2019):

$$\dot{E}x_{ch} = \dot{n}\left(\sum_i x_i \, \overline{ex}_i^{ch,0}\right) + \Delta G^{mix} \tag{4.21}$$

ΔG^{mix} signifies the Gibbs free energy alteration of the mixture under ambient temperature and pressure conditions. Identifying the distribution and magnitude of irreversibility across different processes within a thermodynamic system is the key objective of conducting exergy analysis. This analysis aids in assessing the extent of inefficiencies and devising strategies for enhancing system performance. The exergy balance equation can be expressed as follows (Ebrahimi & Ziabasharhagh, 2017):

$$Ex_i + Ex_{Qi} = Ex_o + Ex_{Qo} + W_{sh} + I \tag{4.22}$$

This equation serves to compute irreversibility or exergy destruction, where Ex_i and Ex_o represent the input and output exergies of flows, Ex_{Qo} denote output exergies of energy flows, W_{sh} signifies the shaft work on or by the system Ex_{Qi} is input exergy of energy flows and, and I indicates irreversibility or exergy destruction (Ebrahimi & Ziabasharhagh, 2017):

$$I_{p,c} = Ex_i - Ex_o = \sum(\dot{m}ex)_i + W - \sum(\dot{m}ex)_o \tag{4.23}$$

The equations used for calculating the exergy efficiency and exergy destruction of each equipment and the total process in different scenarios for the liquefaction of hydrogen are provided in Table 4-1.

Table 4-1 Exergy efficiency and destruction formulas of different equipment used in the design

Components	Exergy efficiency	Exergy destruction
Heat exchangers	$\eta_{ex} = 1 - \left(\frac{\sum \dot{m}.\Delta ex}{\sum \dot{m}.\Delta h}\right)_{ht} + \left(\frac{\sum \dot{m}.\Delta ex}{\sum \dot{m}.\Delta h}\right)_{cd}$	$\dot{I} = \sum (\dot{m}ex)_{in} - \sum (\dot{m}ex)_{out}$
Compressors	$\eta_{ex} = \frac{\sum (\dot{m}ex)_{in} - \sum (\dot{m}ex)_{out}}{\dot{W}}$	$\dot{I} = \dot{W} + \sum (\dot{m}ex)_{in} - \sum (\dot{m}ex)_{out}$
Expanders	$\eta_{ex} = \frac{\dot{W}}{\sum (\dot{m}ex)_{in} - \sum (\dot{m}ex)_{out}}$	$\dot{I} = \sum (\dot{m}ex)_{in} - \sum (\dot{m}ex)_{out} - \dot{W}$
Towers and flash drums	$\eta_{ex} = \frac{\sum (\dot{m}ex)_{out}}{\sum (\dot{m}ex)_{in}}$	$\dot{I} = \sum (\dot{m}ex)_{in} - \sum (\dot{m}ex)_{out}$
Pumps	$\eta_{ex} = \frac{\sum (\dot{m}e)_{in} - \sum (\dot{m}e)_{out}}{\dot{W}}$	$\dot{I} = \sum (\dot{m}e)_{in} + \dot{W} - \sum (\dot{m}e)_{out}$
Reactors	$\eta_{ex} = \frac{\sum (\dot{m}ex)_{out}}{\sum (\dot{m}ex)_{in}}$	$\dot{I} = \sum (\dot{m}ex)_{in} - \sum (\dot{m}ex)_{out}$

Components	Exergy efficiency	Exergy destruction
Cycle/process	$\eta_{ex} = \frac{(\dot{E}_x)_{Product} - (\dot{E}_x)_{Feed}}{W_{net}}$	$\dot{I} = \sum(\dot{m}ex)_{in} - \sum(\dot{m}ex)_{out}$

CHAPTER 5

RESULTS AND DISCUSSION

5.1 Introduction

This chapter presents the findings from our energy simulations and exergy analyses of the three proposed scenarios for integrating waste heat into the hydrogen liquefaction process. The pinch, exergy, and energy analysis results are presented in this chapter. The performance of each scenario was evaluated based on specific power consumption, coefficients of performance, and exergy efficiency. The results highlight the comparative advantages and potential of these waste heat recovery systems in optimizing hydrogen liquefaction processes.

5.2 Pinch Analysis Result

Pinch analysis is a powerful method for minimizing energy consumption in thermodynamic processes and heat recovery systems, creating an optimal design for the heat exchanger that reduces the need for heating and cooling (Linnhoff, 1993). There are always temperature gaps between cold and hot streams in multi-stream heat exchangers. The closer the hot and cold diagrams in multi-flow heat exchangers are, the lower the power consumption of the refrigeration cycle and the higher the efficiency of the whole system. The pinch technology can modify energy consumption and determine the required utility using its critical hot and cold composite curves (CC) tools. In this study, Aspen HYSYS V10.0 software is used to determine the pinch point, and MATLAB V10.0 software, in connection with Aspen HYSYS V10.0, is used to draw the composite curves. Figure 5-1, Figure 5-2, and Figure 5-3 depict both hot and cold composite curves of the complex heat exchanger network designed for the liquefaction process of hydrogen. Based on these figures, the minor temperature differences between the hot and cold curves over a range of more than 260 degrees prove the high performance of the heat exchanger network in all three scenarios.

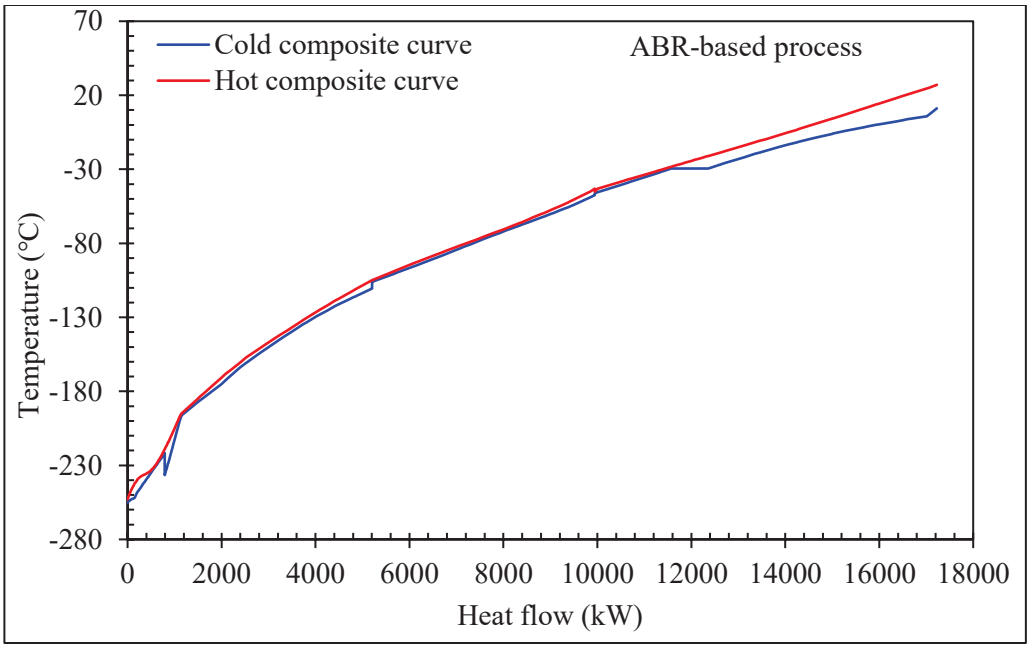

Figure 5-1 Cold and hot composite curves for the process based on the Ammonia-Water Absorption Refrigeration Cycle

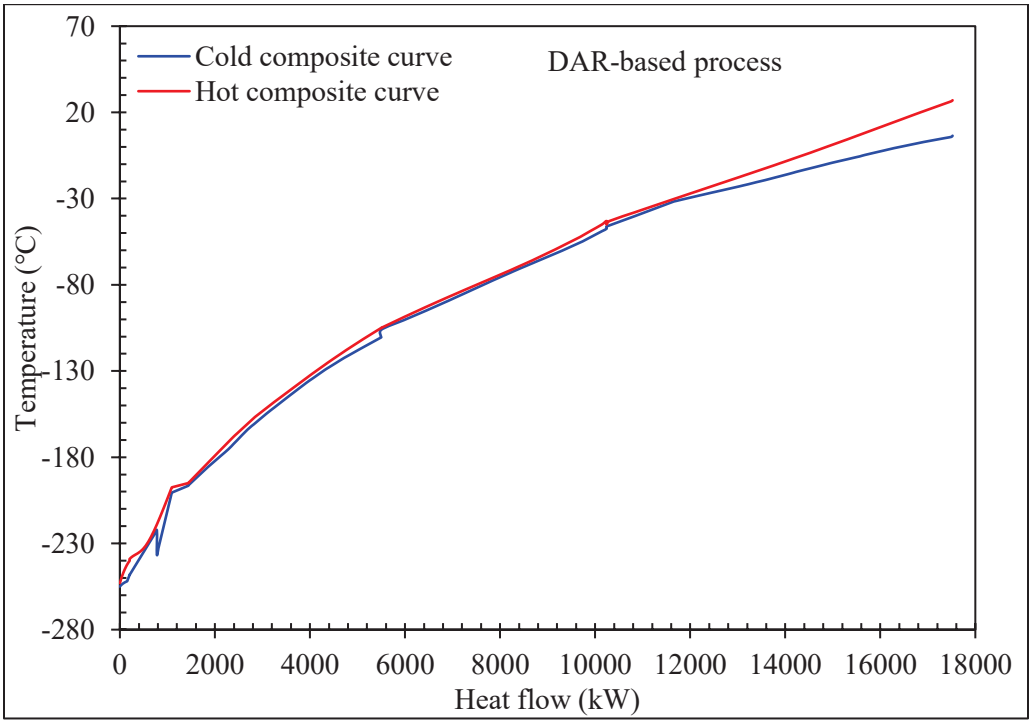

Figure 5-2 Cold and hot composite curves for the process based on the Diffusion Absorption Refrigeration Cycle

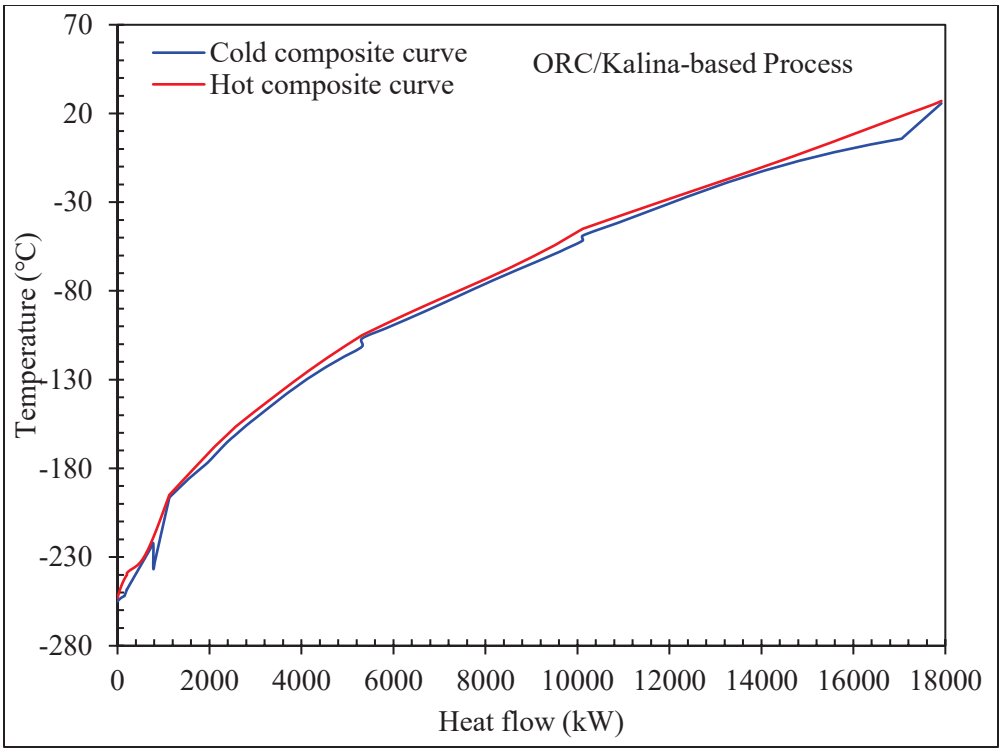

Figure 5-3 Cold and hot composite curves for the process based on the combination of ORC and Kalina power generation cycle

5.3 Exergy Analysis Results

The first stage of exergy analysis involves computing the exergy of streams within processes and assessing each stream's exergy loss. Applying the exergy balance to individual equipment components makes it possible to compute their destruction and efficiency. Table 5-1, Table 5-2, and Table 5-3 provide data on the input and output exergies, exergy destruction, and exergy efficiency of different equipment used in each scenario. Based on these tables, in all three scenarios, turbines and pumps are among the equipment with the lowest exergy efficiencies, while conversion reactors, distillation columns, and heat exchangers are among the equipment with the highest calculated exergy efficiencies. Figure 5-4, Figure 5-5, and Figure 5-6 show the share of each equipment group in the total exergy destruction of the process in different scenarios. Heat exchangers take the lion’s share of exergy destruction in all three scenarios, with 48 percent for the DAR-based and the ORC/Kalina-based scenarios

and 47 percent for the ABR-based process. After heat exchangers, turbines, with around 22 percent, take second place in the equipment contributing to the maximum exergy destruction share. In all three scenarios, pumps contribute the lowest exergy destruction.

Table 5-1 Input and output exergies, exergy destruction, and exergy efficiency of different equipment used in the ABR-based scenario

Equipment	Input exergy (kW)	Output exergy (kW)	Exergy destruction (kW)	Exergy efficiency
HX1	102662.7	102422.0	240.7	0.953
HX2	106886.7	106629.9	256.8	0.950
HX3	110888.0	110631.4	256.6	0.950
HX4	1020945.7	1020875.1	70.6	0.979
HX5	829946.0	829893.4	52.6	0.982
HX6	2147301.8	2147047.6	254.2	0.796
HX7	1368579.2	1368502.6	76.7	0.970
HX8	649408.7	649139.0	269.8	0.956
HX9	163294.7	162971.1	323.6	0.794
HX10	37877.0	37822.6	54.4	0.966
HX11	197814.2	197325.8	488.4	0.884
HX12	98219.7	97991.6	228.1	0.963
HX13	185691.1	184982.5	708.6	0.744
HX14	64136.2	63814.8	321.4	0.950
HX15	61004.0	60943.2	60.7	0.952
HX16	46041.5	46020.0	21.5	0.978
HX17	32286.9	32253.8	33.2	0.851
T1	383018.5	383015.5	3.0	0.872
T2	363906.3	363902.8	3.5	0.834
T3	255726.0	255715.2	10.8	0.700
T4	20851.9	20501.4	350.6	0.509

Equipment	Input exergy (kW)	Output exergy (kW)	Exergy destruction (kW)	Exergy efficiency
T5	54912.1	54032.4	879.7	0.413
T6	36835.8	36426.3	409.4	0.348
T7	151540.9	151492.7	48.1	0.370
C1	995197.5	994987.9	209.6	0.913
C2	811631.8	811506.7	125.1	0.913
C3	92179.6	91801.5	378.1	0.927
C4	96200.8	95822.7	378.1	0.927
C5	100196.2	99818.1	378.2	0.927
P1	184619.3	184618.4	0.8	0.869
CR1	143853.9	143158.8	695.0	0.995
CR2	148118.3	147983.2	135.1	0.999
D1	994814.1	994814.1	0.0	1.000
D2	995946.4	995946.4	0.0	1.000
D3	613756.7	613756.7	0.0	1.000
D4	151464.5	151464.5	0.0	1.000
DT	22778.9	22521.6	257.3	0.989
V1	16241.2	16239.0	2.1	0.679
HX18	27987.5	27900.9	86.6	0.956
P2	21719.7	21719.5	0.2	0.969

Table 5-2 Input and output exergies, exergy destruction, and exergy efficiency of different equipment used in the DAR-based scenario

Equipment	Input exergy (kW)	Output exergy (kW)	Exergy destruction (kW)	Exergy efficiency
HX1	102610.5	102373.5	237.0	0.953
HX2	106886.7	106629.9	256.8	0.950
HX3	110888.0	110631.4	256.6	0.950
HX4	1019151.9	1019103.4	48.5	0.985
HX5	829946.0	829893.4	52.6	0.982
HX6	2176963.7	2176713.3	250.4	0.798
HX7	1368579.2	1368502.6	76.7	0.970
HX8	649408.7	649139.0	269.8	0.956
HX9	163294.7	162971.1	323.6	0.794
HX10	37877.0	37822.6	54.4	0.966
HX11	197814.2	197279.1	535.1	0.870
HX12	98296.1	97991.7	304.5	0.951
HX13	185450.1	184741.5	708.6	0.744
HX14	64136.2	63814.8	321.4	0.950
HX15	91668.2	91662.5	5.7	0.811
HX16	32709.8	32565.2	144.6	0.619
HX17	17038.4	16941.9	96.5	0.994
T1	383018.5	383015.5	3.0	0.872
T2	363906.3	363902.8	3.5	0.834
T3	255726.0	255715.2	10.8	0.700
T4	20851.9	20501.4	350.6	0.509
T5	54912.1	54032.4	879.7	0.413
T6	36835.8	36426.3	409.4	0.348
T7	151299.8	151251.7	48.1	0.370
C1	995167.8	994958.8	209.0	0.911
C2	811631.8	811506.7	125.1	0.913
C3	92173.6	91795.5	378.1	0.926
C4	96200.8	95822.7	378.1	0.927
C5	100196.2	99818.1	378.1	0.927
P1	184619.3	184618.4	0.8	0.869
CR1	143853.9	143158.8	695.0	0.995
CR2	147995.2	147744.5	250.7	0.998
D1	994814.1	994814.1	0.0	1.000
D2	995946.4	995946.4	0.0	1.000
D3	613756.7	613756.7	0.0	1.000

Equipment	Input exergy (kW)	Output exergy (kW)	Exergy destruction (kW)	Exergy efficiency
D4	151223.5	151223.5	0.0	1.000
DT1	53524.1	53501.7	22.4	1.000
DT2	25468.1	25255.5	212.6	0.992

Table 5-3 Input and output exergies, exergy destruction, and exergy efficiency of different equipment used in the ORC/Kalina-based scenario

Equipment	Input exergy (kW)	Output exergy (kW)	Exergy destruction (kW)	Exergy efficiency
HX1	102610.5	102373.5	237.0	0.953
HX2	106886.7	106629.9	256.8	0.950
HX3	110888.0	110631.4	256.6	0.950
HX4	1080699.5	1080564.5	135.0	0.969
HX5	878855.6	878799.9	55.7	0.982
HX6	2248416.3	2248264.9	151.4	0.877
HX7	1440996.2	1440872.9	123.3	0.953
HX8	658599.0	658260.1	338.9	0.947
HX9	163294.7	162971.1	323.6	0.794
HX10	37877.0	37822.6	54.4	0.966
HX11	197814.2	197279.1	535.1	0.870
HX12	98296.1	97991.7	304.5	0.951
HX13	185450.1	184741.5	708.6	0.744
HX14	64136.2	63814.8	321.4	0.950
HX15	178384.1	178353.2	30.9	0.983
HX16	168216.8	167879.0	1.0	0.998
HX17	10520.0	10517.2	2.7	0.987
T1	405590.1	405586.9	3.2	0.872
T2	395672.0	395668.1	3.8	0.834
T3	260408.2	260396.9	11.3	0.700
T4	20851.9	20501.4	350.6	0.509
T5	54912.1	54032.4	879.7	0.413
T6	36835.8	36426.3	409.4	0.348
T7	151299.8	151251.7	48.1	0.370
C1	1053963.9	1053740.4	223.5	0.916
C2	859462.1	859329.6	132.5	0.913
C3	92173.6	91795.5	378.1	0.926
C4	96200.8	95822.7	378.1	0.927
C5	100196.2	99818.1	378.1	0.927

Equipment	Input exergy (kW)	Output exergy (kW)	Exergy destruction (kW)	Exergy efficiency
P1	195499.0	195498.2	0.9	0.869
CR1	143853.9	143158.8	695.0	0.995
CR2	147995.2	147744.5	250.7	0.998
D1	1053439.5	1053439.5	0.0	1.000
D2	1054638.5	1054638.5	0.0	1.000
D3	649972.4	649972.4	0.0	1.000
D4	151223.5	151223.5	0.0	1.000
T8	152769.9	152751.5	18.4	0.923
T9	15109.1	15107.3	1.8	0.923
T10	23495.6	23467.6	28.0	0.898
P2	167503.4	167453.3	3.8	0.860
P3	29818.7	29817.9	0.9	0.856

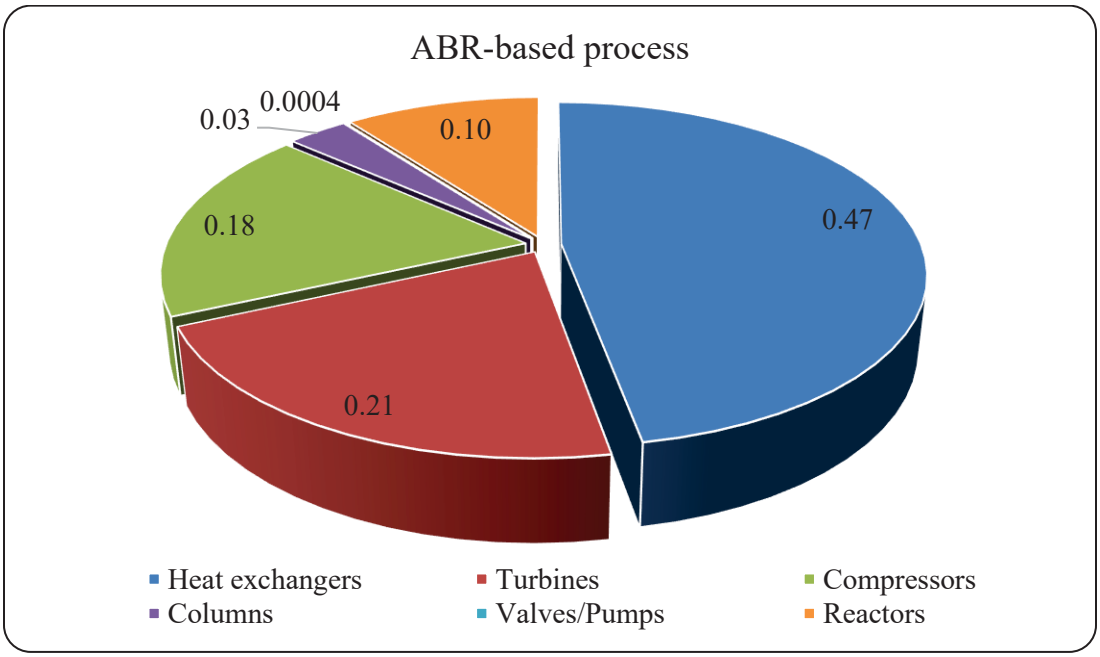

Figure 5-4 The share of each equipment in the total exergy destruction in the ABR-based scenario

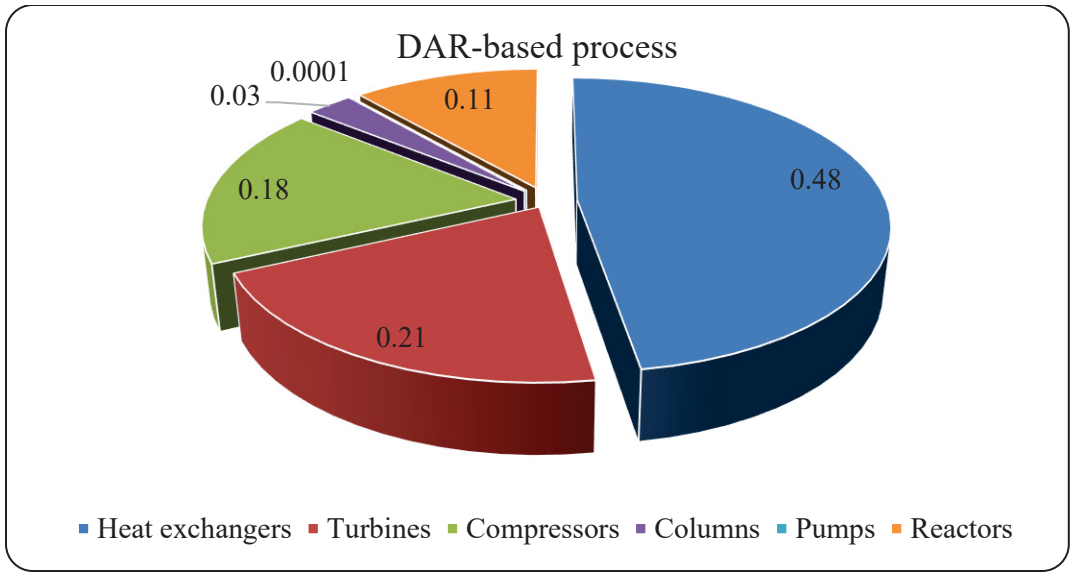

Figure 5-5 The share of each equipment in the total exergy destruction in the DAR-based scenario

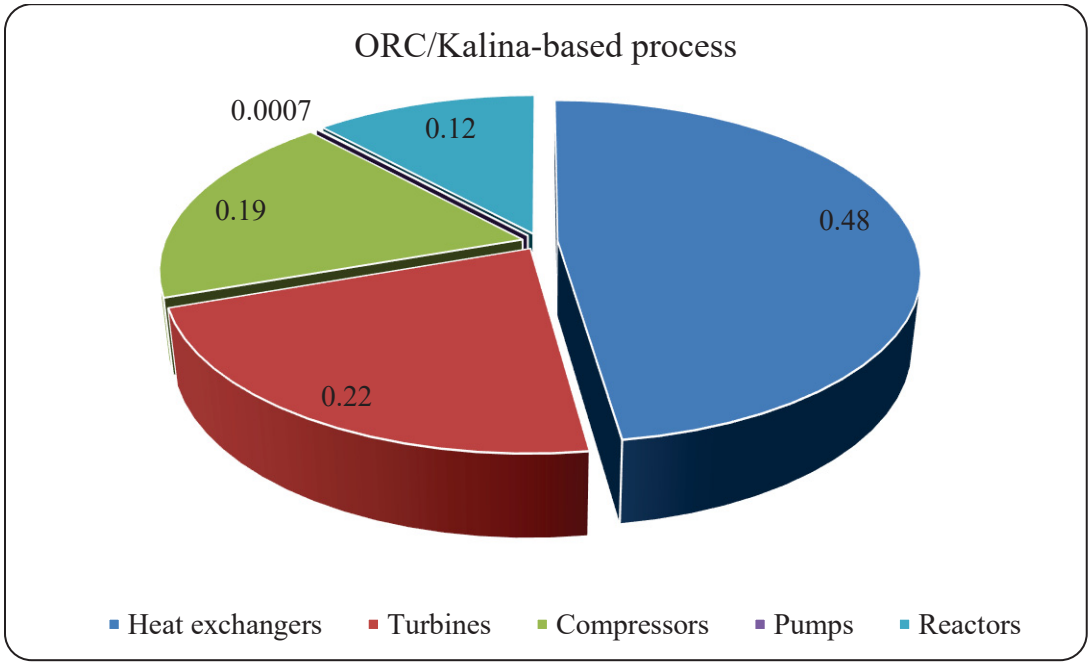

Figure 5-6 The share of each equipment in the total exergy destruction in the ORC/Kalina-based scenario

Table 5-4 shows the total exergy efficiency and destruction of the different scenarios and their subsystems. Based on the information in this table, it should be deduced that the exergy efficiency of the total integrated process and the exergy efficiency of H_2 pre-cooling process in all three scenarios are improved compared to the basic cycle. ABR-based cycle proved the maximum total exergy efficiency with 52.47%, followed by the ORC/Kalina-based cycle with 51.45%. The total exergy efficiency of the DAR-based cycle is calculated to be 51.28%, the lowest efficiency among the three scenarios. On the other hand, the maximum exergy efficiency of H_2 pre-cooling process belongs to the ORC/Kalina-based scenario with 70.84%, followed by the DAR-based and ABR-based cycles with 69.72% and 68.85%, respectively. The exergy efficiency of H_2 cryogenic unit is equal for the ORC/Kalina-based and DAR-based scenarios, with 51.65% equal to the basic process. However, the exergy efficiency of H_2 cryogenic unit for the ABR-based cycle with 53.31% is higher than the other two scenarios. It should be mentioned that the exergy efficiency of the diffusion-absorption refrigeration subsystem is 24.85% in the DAR-based scenario, and the exergy efficiency of the absorption refrigeration subsystem in the ABR-based scenario is 23.69%. Regarding the exergy destruction, the ORC/Kalina-based scenario proves the lowest exergy destruction with 8.03 MW, followed by ABR-based and DAR-based scenarios with 8.07 and 8.30 MW of exergy destruction.

Table 5-4 Comparison between the key parameters related to the performance of different scenarios considered in the hydrogen liquefaction process

Specifications	ORC/Kalina-based	Basic cycle	DAR-based cycle	ABR-based cycle
Liquid hydrogen flow rate (kg/h)	4166.4	4166.4	4166.4	4166.4
SPC of H_2 liquefaction system (kWh/kgLH_2)	4.306	4.415	4.320	4.333
Exergy efficiency of the hybrid process	0.5145	0.5018	0.5128	0.5247
Required power consumption (kW)	17941.8	18395.7	18000.4	18053.5
Exergy destruction of integrated system (kW)	8032.7	7946.2	8297.7	8069.1

Specifications	ORC/Kalina-based	Basic cycle	DAR-based cycle	ABR-based cycle
SPC of H_2 pre-cooling process (kWh/kgLH_2)	0.8816	0.9906	0.8957	0.9070
SPC of H_2 cryogenic system (kWh/kgLH_2)	3.424	3.424	3.424	3.426
Exergy efficiency of H_2 pre-cooling process	0.7084	0.6304	0.6972	0.6885
Exergy efficiency of H_2 cryogenic unit	0.5165	0.5165	0.5165	0.5331
COP of diffusion-absorption refrigeration	-	-	0.4893	-
COP of absorption refrigeration		-	-	0.3934
Exergy of diffusion-absorption refrigeration	-	-	0.2485	-
Exergy of absorption refrigeration	-	-	-	0.2369

5.4 Energy Analysis Results

Based on the simulation performed by linking the Aspen HYSYS software and MATLAB m-file coding, Figure 5-7, Figure 5-8, Figure 5-9, and Table 5-4 demonstrate the comparison between the specific power consumptions, the coefficient of performance of the liquefaction process, the required power consumptions of the process and its subsystems in the different scenarios considered for the liquefaction process of hydrogen. Based on the results, it is found that the ORC/Kalina-based scenario achieved the lowest specific power consumption by 4.306 kWh/kg LH_2, slightly lower than that of the DAR-based scenario (4.320 kWh/kg LH_2) and ABR-based scenario (4.333 kWh/kg LH_2).

These differences in SPCs are due to the differences in the specific power consumptions in the multi-component refrigeration process employed in the precooling stage. While the specific power consumption of the cascaded Joule-Briton subsystem for all three scenarios is almost the same, with 3.425 and 4.320 kWh/kg LH_2, the SPC of the multi-component refrigeration unit follows the same trend as the total SPC calculated for different scenarios. As a result, the

SPC of the mixed refrigerant refrigeration cycle for the ORC/Kalina-based scenario is the lowest value among all scenarios, with 0.882 kWh/kg LH_2, lower than that of the DAR-based scenario and ABR-based scenario with 0.896 and 0.907 kWh/kg LH_2, respectively. The coefficient of performance associated with all scenarios is almost the same, with 0.286, which is 2 percent higher than the basic unit and nearly 60 percent higher than that of the reference paper (Sadaghiani & Mehrpooya, 2017). It should be mentioned that the total power consumption for the designed processes in different scenarios for the liquefaction of hydrogen with a rate of 4167 kg/h are 17.94 MW, 18.00 MW, and 18.05 MW for the ORC/Kalina-based, DAR-based, and ABR-based scenarios, respectively.

Figure 5-11 and Figure 5-12 illustrate the validation results of the different scenarios with reference papers (Taghavi & Lee, 2024). It can be noticed that the simulations performed in this study have an acceptable concordance with the critical design parameters in the reference papers.

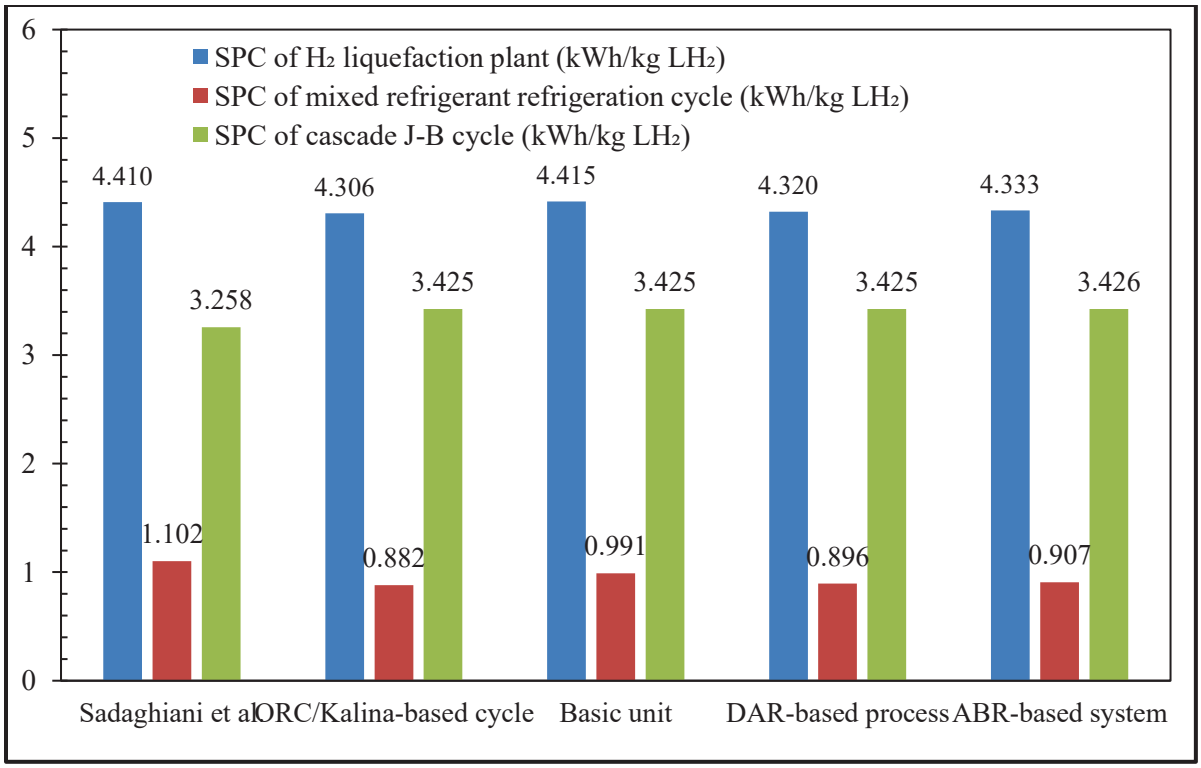

Figure 5-7 The comparison between the SPCs of the process and its subsystems for the different scenarios under study

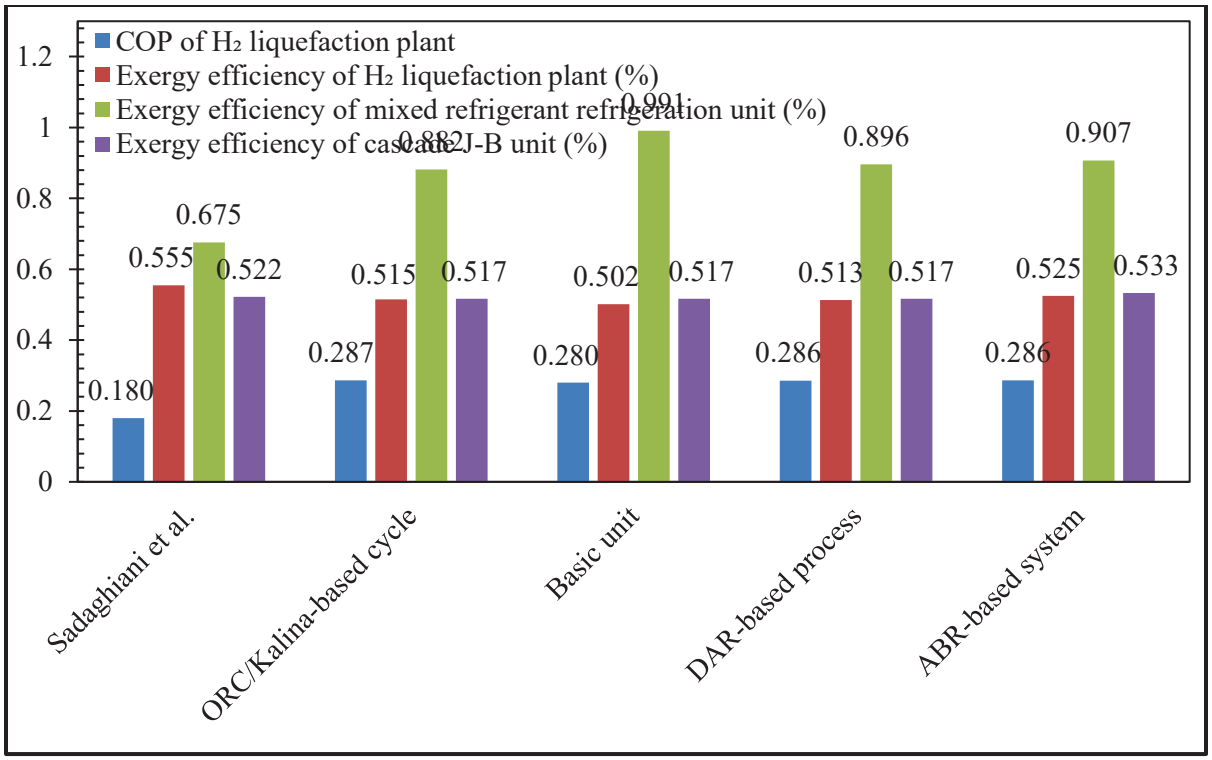

Figure 5-8 The comparison between the COP of the liquefaction process and exergy efficiencies of its subsystems in the different scenarios under study and the reference paper Taken from Sadaghiani et al. (2017)

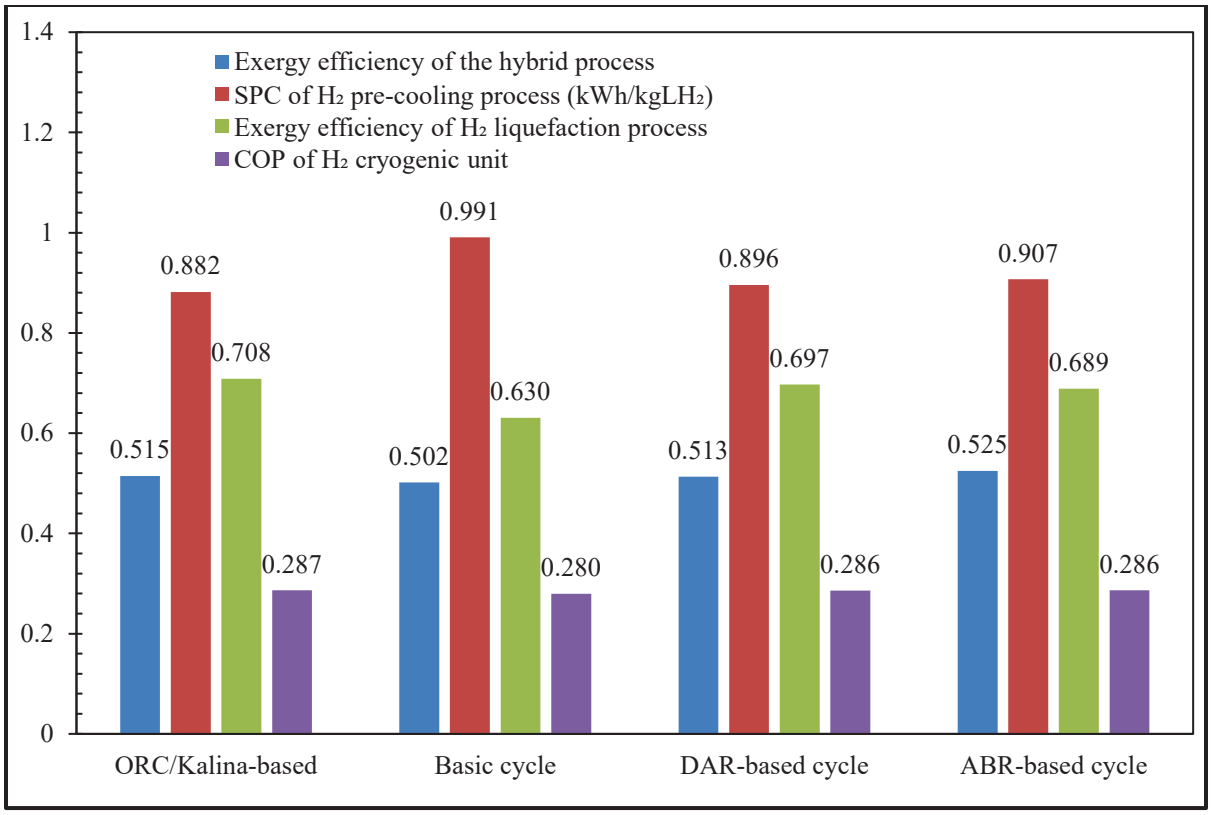

Figure 5-9 The comparison between the COP of the cryogenic unit, SPC of the precooling process, and exergy efficiencies of the whole and the liquefaction processes in the different scenarios under study

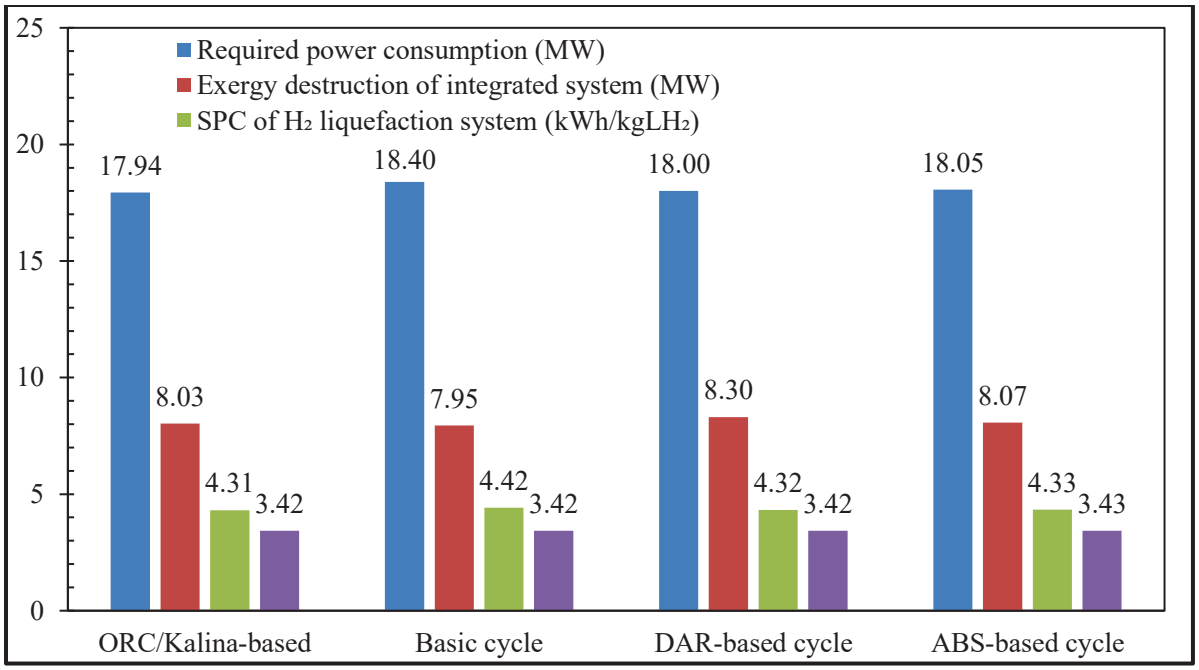

Figure 5-10 The comparison between the required power consumptions, exergy destructions, and SPCs of the hydrogen liquefaction system in the different scenarios under study

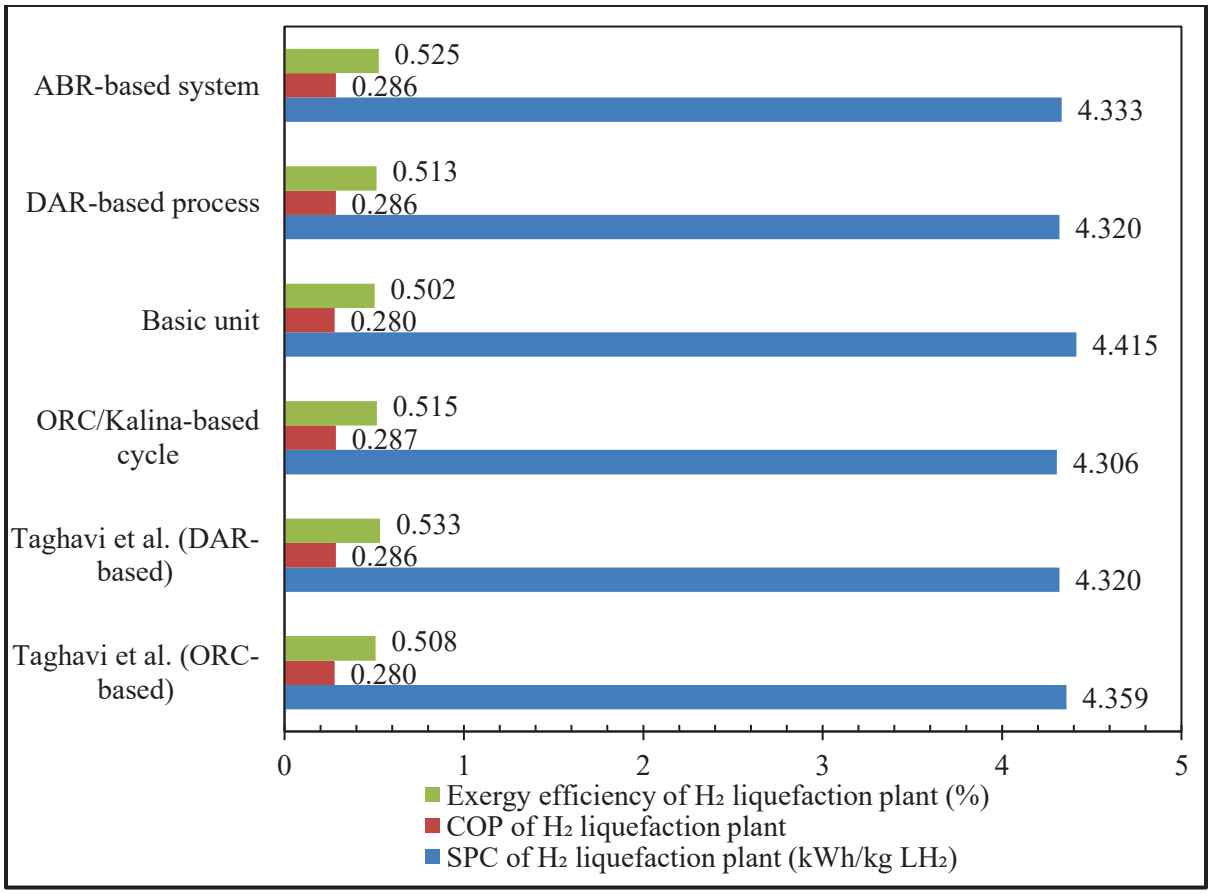

Figure 5-11 The validation results of the different scenarios with reference paper Taken from Taghavi et al. (2024)

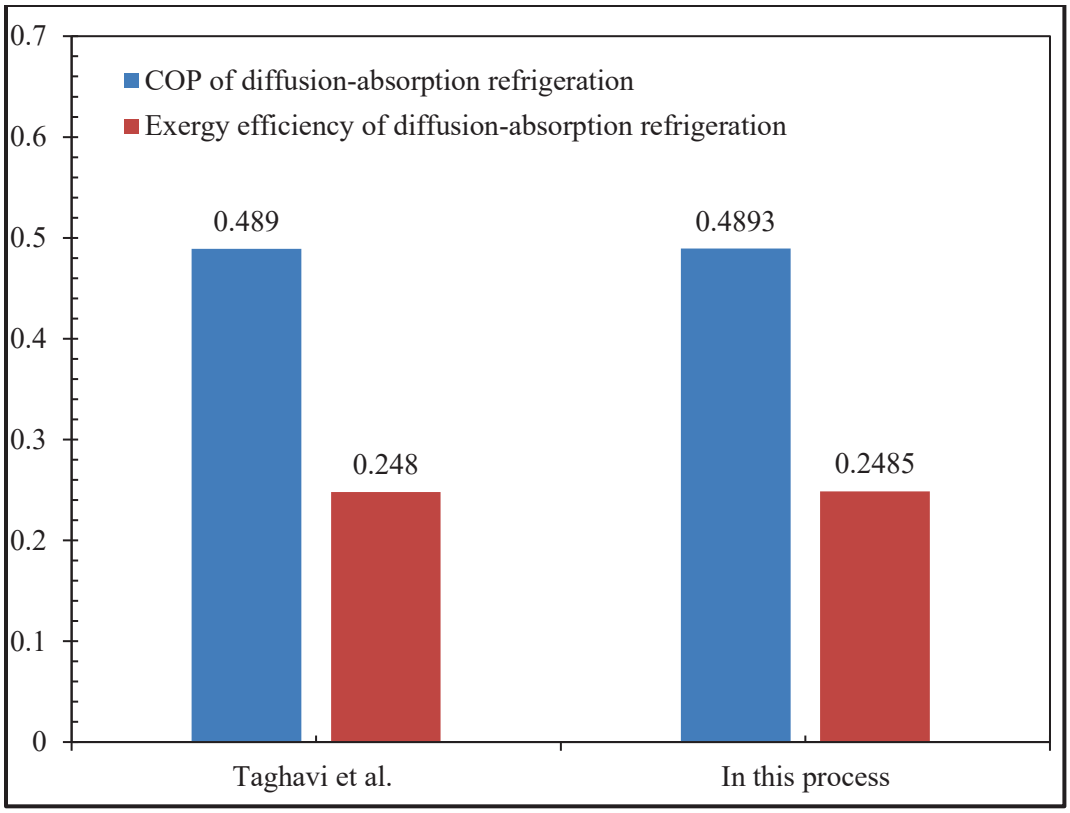

Figure 5-12 Validation result of the DAR-based scenario compared to the reference paper
Taken from Taghavi et al. (2024)

CONCLUSION

Renewable energy sources present a viable and sustainable solution to the challenges of fossil fuels, such as pollution and increasing energy demand. Among these renewable options, hydrogen has emerged as a particularly promising alternative, capturing the interest of researchers and industry alike. Various methods for hydrogen production have been suggested, each with distinct energy consumption characteristics and to improve the process's thermodynamic and exergy efficiency. One approach involves using waste heat from power plants or other industrial units. This thesis examines three novel scenarios utilizing 2000 kilowatts of excess heat in a hydrogen liquefaction cycle:

- An Ammonia-Water Absorption Refrigeration Cycle absorbs the waste heat to provide part of the precooling needed for liquefaction, integrated via a multi-stream heat exchanger.
- A Diffusion-Absorption Refrigeration Cycle uses the waste heat to assist in hydrogen precooling.
- A combination of the Organic Rankine Cycle and Kalina Cycle converts the waste heat into electrical power, supplying part of the energy needed for liquefaction.

The simulation and analysis results and the conclusion can be categorized as follows:

1- Energy simulations indicated that the ORC/Kalina-based scenario achieved the lowest specific power consumption at 4.306 kWh/kg LH_2, marginally better than the DAR-based and ABR-based scenarios. All scenarios exhibited similar coefficients of performance, approximately 2% higher than the baseline and significantly better than reference values. The total power consumption for hydrogen liquefaction was slightly lower in the ORC/Kalina-based scenario compared to the others. Pinch analysis, conducted using Aspen HYSYS and MATLAB, showed high performance of the heat exchanger network across all three scenarios.

The minimal temperature differences between hot and cold curves, spanning over 260 degrees, indicate efficient energy utilization.

2- The exergy analysis revealed that heat exchangers are the primary contributors to exergy destruction, accounting for nearly half of the total in each scenario. Turbines also contributed significantly, while pumps had the lowest impact. The ABR-based cycle demonstrated the highest total exergy efficiency at 52.47%, followed closely by the ORC/Kalina-based and DAR-based cycles. However, the ORC/Kalina-based scenario had the highest exergy efficiency for the H_2 pre-cooling process at 70.84%. The lowest exergy destruction was observed in the ORC/Kalina-based scenario.

3- The ORC/Kalina-based scenario emerged as the most efficient in terms of specific power consumption and exergy destruction. The ABR-based cycle, on the other hand, achieved the highest overall exergy efficiency. These results demonstrate the potential benefits of integrating waste heat recovery systems to enhance the efficiency of hydrogen liquefaction processes. The findings underscore that using waste heat can significantly reduce specific power consumption and improve overall system efficiency.

4- For further investigation, an economic analysis along with sensitivity analyses could be conducted on these processes to assess the economic viability and compare the attractiveness of these scenarios. This would help determine whether the added equipment and complexity are justified by the improvements in efficiency and reductions in specific energy consumption (SEC).

BIBLIOGRAPHY

Aasadnia, M., & Mehrpooya, M. (2018a). Conceptual design and analysis of a novel process for hydrogen liquefaction assisted by absorption precooling system. Journal of Cleaner Production, 205, 565–588. https://doi.org/10.1016/j.jclepro.2018.09.001

Aasadnia, M., & Mehrpooya, M. (2018b). Large-scale liquid hydrogen production methods and approaches: A review. Applied Energy, 212, 57–83. https://doi.org/10.1016/j.apenergy.2017.12.033

Aasadnia, M., Mehrpooya, M., & Ansarinasab, H. (2019). A 3E evaluation on the interaction between environmental impacts and costs in a hydrogen liquefier combined with absorption refrigeration systems. Applied Thermal Engineering, 159, 113798. https://doi.org/10.1016/j.applthermaleng.2019.113798

Abbas, H. F., & Wan Daud, W. M. A. (2010). Hydrogen production by methane decomposition: A review. International Journal of Hydrogen Energy, 35(3), 1160–1190. https://doi.org/10.1016/j.ijhydene.2009.11.036

Ahmadi, M. H., Ahmadi, M.-A., Maleki, A., Pourfayaz, F., Bidi, M., & Açıkkalp, E. (2017). Exergetic sustainability evaluation and multi-objective optimization of performance of an irreversible nanoscale Stirling refrigeration cycle operating with Maxwell–Boltzmann gas. Renewable and Sustainable Energy Reviews, 78, 80–92. https://doi.org/10.1016/j.rser.2017.04.097

Al Ghafri, S. Zs., Munro, S., Cardella, U., Funke, T., Notardonato, W., Trusler, J. P. M., Leachman, J., Span, R., Kamiya, S., Pearce, G., Swanger, A., Rodriguez, E. D., Bajada, P., Jiao, F., Peng, K., Siahvashi, A., Johns, M. L., & May, E. F. (2022a). Hydrogen liquefaction: A review of the fundamental physics, engineering practice and future opportunities. Energy & Environmental Science, 15(7), 2690–2731. https://doi.org/10.1039/D2EE00099G

Amirhaeri, Y., Hadavi, H., & Kasaeian, A. (2024). Exergy and energy analysis of a hybrid natural Gas/Hydrogen liquefaction cycle combined with methanol production plant. Energy Conversion and Management, 299, 117834. https://doi.org/10.1016/j.enconman.2023.117834

Azarpour, A., Mohammadzadeh, O., Rezaei, N., & Zendehboudi, S. (2022). Current status and future prospects of renewable and sustainable energy in North America: Progress and challenges. Energy Conversion and Management, 269, 115945. https://doi.org/10.1016/j.enconman.2022.115945

Bénard, P., Chahine, R., Chandonia, P. A., Cossement, D., Dorval-Douville, G., Lafi, L., Lachance, P., Paggiaro, R., & Poirier, E. (2007). Comparison of hydrogen adsorption on nanoporous materials. Journal of Alloys and Compounds, 446–447, 380–384. https://doi.org/10.1016/j.jallcom.2006.11.192

Ebrahimi, A., Ghorbani, B., & Ziabasharhagh, M. (2022). Exergy and economic analyses of an innovative integrated system for cogeneration of treated biogas and liquid carbon dioxide using absorption–compression refrigeration system and ORC/Kalina power cycles through geothermal energy. Process Safety and Environmental Protection, 158, 257–281. https://doi.org/10.1016/j.psep.2021.12.011

Ebrahimi, A., & Ziabasharhagh, M. (2017). Optimal design and integration of a cryogenic Air Separation Unit (ASU) with Liquefied Natural Gas (LNG) as heat sink, thermodynamic and economic analyses. Energy, 126, 868–885. https://doi.org/10.1016/j.energy.2017.02.145

Elberry, A. M., Thakur, J., Santasalo-Aarnio, A., & Larmi, M. (2021). Large-scale compressed hydrogen storage as part of renewable electricity storage systems. International Journal of Hydrogen Energy, 46(29), 15671–15690. https://doi.org/10.1016/j.ijhydene.2021.02.080

Felderhoff, M., Weidenthaler, C., Von Helmolt, R., & Eberle, U. (2007). Hydrogen storage: The remaining scientific and technological challenges. Physical Chemistry Chemical Physics, 9(21), 2643. https://doi.org/10.1039/b701563c

Ghazvini, M., Sadeghzadeh, M., Ahmadi, M. H., Moosavi, S., & Pourfayaz, F. (2019). Geothermal energy use in hydrogen production: A review. International Journal of Energy Research, er.4778. https://doi.org/10.1002/er.4778

Ghorbani, B., Ebrahimi, A., Rooholamini, S., & Ziabasharhagh, M. (2021). Integrated Fischer-Tropsch synthesis process with hydrogen liquefaction cycle. Journal of Cleaner Production, 283, 124592. https://doi.org/10.1016/j.jclepro.2020.124592

Ghorbani, B., Mehrpooya, M., Aasadnia, M., & Niasar, M. S. (2019). Hydrogen liquefaction process using solar energy and organic Rankine cycle power system. Journal of Cleaner Production, 235, 1465–1482. https://doi.org/10.1016/j.jclepro.2019.06.227

Ghorbani, B., Zendehboudi, S., & Moradi, M. (2021). Development of an integrated structure of hydrogen and oxygen liquefaction cycle using wind turbines, Kalina power generation cycle, and electrolyzer. Energy, 221, 119653. https://doi.org/10.1016/j.energy.2020.119653

Ghorbani, B., Zendehboudi, S., Saady, N. M. C., Duan, X., & Albayati, T. M. (2023a). Strategies To Improve the Performance of Hydrogen Storage Systems by Liquefaction Methods: A Comprehensive Review. ACS Omega, 8(21), 18358–18399. https://doi.org/10.1021/acsomega.3c01072

Ghorbani, B., Zendehboudi, S., Saady, N. M. C., & Dusseault, M. B. (2023a). Hydrogen storage in North America: Status, prospects, and challenges. Journal of Environmental Chemical Engineering, 11(3), 109957. https://doi.org/10.1016/j.jece.2023.109957

Gielen, D., Boshell, F., Saygin, D., Bazilian, M. D., Wagner, N., & Gorini, R. (2019). The role of renewable energy in the global energy transformation. Energy Strategy Reviews, 24, 38–50. https://doi.org/10.1016/j.esr.2019.01.006

Hassan, I. A., Ramadan, H. S., Saleh, M. A., & Hissel, D. (2021). Hydrogen storage technologies for stationary and mobile applications: Review, analysis and perspectives. Renewable and Sustainable Energy Reviews, 149, 111311. https://doi.org/10.1016/j.rser.2021.111311

Hutter, K., & Wang, Y. (2016). Thermodynamics—Fundamentals. In Fluid and Thermodynamics: Vol. 2: Advanced Fluid Mechanics and Thermodynamic Fundamentals (pp. 317–420). Springer International Publishing. https://doi.org/10.1007/978-3-319-33636-7

Jouybari, A. K., Ilinca, A., Ghorbani, B., & Rooholamini, S. (2022). Thermodynamic and exergy evaluation of an innovative hydrogen liquefaction structure based on ejector-compression refrigeration unit, cascade multi-component refrigerant system, and Kalina power plant. International Journal of Hydrogen Energy, 47(62), 26369–26393. https://doi.org/10.1016/j.ijhydene.2022.01.190

Kanoglu, M., Dincer, I., & Rosen, M. (2007). Geothermal energy use in hydrogen liquefaction. International Journal of Hydrogen Energy, 32(17), 4250–4257. https://doi.org/10.1016/j.ijhydene.2007.06.006

Kanoglu, M., Yilmaz, C., & Abusoglu, A. (2016). Geothermal energy use in absorption precooling for Claude hydrogen liquefaction cycle. International Journal of Hydrogen Energy, 41(26), 11185–11200. https://doi.org/10.1016/j.ijhydene.2016.04.068

Kharel, S., & Shabani, B. (2018). Hydrogen as a Long-Term Large-Scale Energy Storage Solution to Support Renewables. Energies, 11(10), 2825. https://doi.org/10.3390/en11102825

Kotas, T. J. (2013). The Exergy Method of Thermal Plant Analysis: Elsevier.

Leonzio, G. (2018). Methanol Synthesis: Optimal Solution for a Better Efficiency of the Process. Processes, 6(3), 20. https://doi.org/10.3390/pr6030020

Linnhoff, B. (1993). Pinch analysis—A state-of-the-art overview. Chemical Engineering Research & Design, 71, 503–522.

Liu, X., Hu, G., & Zeng, Z. (2023). Performance characterization and multi-objective optimization of integrating a biomass-fueled brayton cycle, a kalina cycle, and an organic rankine cycle with a claude hydrogen liquefaction cycle. Energy, 263, 125535. https://doi.org/10.1016/j.energy.2022.125535

Madadi Avargani, V., Zendehboudi, S., Cata Saady, N. M., & Dusseault, M. B. (2022). A comprehensive review on hydrogen production and utilization in North America: Prospects and challenges. Energy Conversion and Management, 269, 115927. https://doi.org/10.1016/j.enconman.2022.115927

Manisalidis, I., Stavropoulou, E., Stavropoulos, A., & Bezirtzoglou, E. (2020). Environmental and Health Impacts of Air Pollution: A Review. Frontiers in Public Health, 8, 14. https://doi.org/10.3389/fpubh.2020.00014

Mehrpooya, M., Amirhaeri, Y., & Hadavi, H. (2022). Proposal and investigation of a novel small-scale natural gas liquefaction process using diffusion absorption refrigeration technology. Chemical Papers, 76(9), 5901–5927. https://doi.org/10.1007/s11696-022-02294-x

Mehrpooya, M., Mousavi, S. A., Asadnia, M., Zaitsev, A., & Sanavbarov, R. (2021). Conceptual design and evaluation of an innovative hydrogen purification process applying diffusion-absorption refrigeration cycle (Exergoeconomic and exergy analyses). Journal of Cleaner Production, 316, 128271. https://doi.org/10.1016/j.jclepro.2021.128271

Mehrpooya, M., Mousavi, S. A., Delpisheh, M., Zaitsev, A., & Nikitin, A. (2022). 4E assessment and 3D parametric analysis of an innovative liquefied natural gas production process assisted by a diffusion–absorption refrigeration unit. Chemical Papers, 76(8), 5231–5252. https://doi.org/10.1007/s11696-022-02227-8

Moradi, M., Ghorbani, B., Ebrahimi, A., & Ziabasharhagh, M. (2021). Process integration, energy and exergy analyses of a novel integrated system for cogeneration of liquid ammonia and power using liquefied natural gas regasification, CO2 capture unit and solar dish collectors. Journal of Environmental Chemical Engineering, 9(6), 106374. https://doi.org/10.1016/j.jece.2021.106374

Moreno-Blanco, J., Petitpas, G., Espinosa-Loza, F., Elizalde-Blancas, F., Martinez-Frias, J., & Aceves, S. M. (2019). The storage performance of automotive cryo-compressed hydrogen vessels. International Journal of Hydrogen Energy, 44(31), 16841–16851. https://doi.org/10.1016/j.ijhydene.2019.04.189

Mousavi, S. A., Mehrpooya, M., & Delpisheh, M. (2022). Development and life cycle assessment of a novel solar-based cogeneration configuration comprised of diffusion-absorption refrigeration and organic Rankine cycle in remote areas. Process Safety and Environmental Protection, 159, 1019–1038. https://doi.org/10.1016/j.psep.2022.01.067

Mukherjee, S., Devaguptapu, S. V., Sviripa, A., Lund, C. R. F., & Wu, G. (2018). Low-temperature ammonia decomposition catalysts for hydrogen generation. Applied Catalysis B: Environmental, 226, 162–181. https://doi.org/10.1016/j.apcatb.2017.12.039

Naquash, A., Qyyum, M. A., Islam, M., Sial, N. R., Min, S., Lee, S., & Lee, M. (2022). Performance enhancement of hydrogen liquefaction process via absorption refrigeration and organic Rankine cycle-assisted liquid air energy system. Energy Conversion and Management, 254, 115200. https://doi.org/10.1016/j.enconman.2021.115200

Nemati, A., Nami, H., Ranjbar, F., & Yari, M. (2017). A comparative thermodynamic analysis of ORC and Kalina cycles for waste heat recovery: A case study for CGAM cogeneration system. Case Studies in Thermal Engineering, 9, 1–13. https://doi.org/10.1016/j.csite.2016.11.003

Ni, M. (2006). An Overview of Hydrogen Storage Technologies. 24(3).

Olabi, A. G., Bahri, A. S., Abdelghafar, A. A., Baroutaji, A., Sayed, E. T., Alami, A. H., Rezk, H., & Abdelkareem, M. A. (2021). Large-vscale hydrogen production and storage technologies: Current status and future directions. International Journal of Hydrogen Energy, 46(45), 23498–23528. https://doi.org/10.1016/j.ijhydene.2020.10.110

Orr, Jr., F. M. (2009). CO2 capture and storage: Are we ready? Energy & Environmental Science, 2(5), 449. https://doi.org/10.1039/b822107n

Pourfayaz, F., Imani, M., Mehrpooya, M., & Shirmohammadi, R. (2019). Process development and exergy analysis of a novel hybrid fuel cell-absorption refrigeration system utilizing nanofluid as the absorbent liquid. International Journal of Refrigeration, 97, 31–41. https://doi.org/10.1016/j.ijrefrig.2018.09.011

Preuster, P., Alekseev, A., & Wasserscheid, P. (2017). Hydrogen Storage Technologies for Future Energy Systems. Annual Review of Chemical and Biomolecular Engineering, 8(1), 445–471. https://doi.org/10.1146/annurev-chembioeng-060816-101334

Quack, H. (2002). Conceptual design of a high efficiency large capacity hydrogen liquefier. AIP Conference Proceedings, 613, 255–263. https://doi.org/10.1063/1.1472029

Rastegari, A. A., Yadav, A. N., & Gupta, A. (Eds.). (2019). Prospects of Renewable Bioprocessing in Future Energy Systems (Vol. 10). Springer International Publishing. https://doi.org/10.1007/978-3-030-14463-0

Ratlamwala, T. A. H., Dincer, I., & Gadalla, M. A. (2012). Thermodynamic analysis of a novel integrated geothermal based power generation-quadruple effect absorption cooling-hydrogen liquefaction system. International Journal of Hydrogen Energy, 37(7), 5840–5849. https://doi.org/10.1016/j.ijhydene.2011.12.119

Ratlamwala, T. A. H., Dincer, I., Gadalla, M. A., & Kanoglu, M. (2012). Thermodynamic analysis of a new renewable energy based hybrid system for hydrogen liquefaction. International Journal of Hydrogen Energy, 37(23), 18108–18117. https://doi.org/10.1016/j.ijhydene.2012.09.036

Rezaie Azizabadi, H., Ziabasharhagh, M., & Mafi, M. (2021). Introducing a proper hydrogen liquefaction concept for using wasted heat of thermal power plants-case study: Parand gas power plant. Chinese Journal of Chemical Engineering, 40, 187–196. https://doi.org/10.1016/j.cjche.2021.02.023

Rusman, N. A. A., & Dahari, M. (2016). A review on the current progress of metal hydrides material for solid-state hydrogen storage applications. International Journal of Hydrogen Energy, 41(28), 12108–12126. https://doi.org/10.1016/j.ijhydene.2016.05.244

Sadaghiani, M. S., & Mehrpooya, M. (2017). Introducing and energy analysis of a novel cryogenic hydrogen liquefaction process configuration. International Journal of Hydrogen Energy, 42(9), 6033–6050. https://doi.org/10.1016/j.ijhydene.2017.01.136

Srikhirin, P., Aphornratana, S., & Chungpaibulpatana, S. (2001). A review of absorption refrigeration technologies. Renewable and Sustainable Energy Reviews, 5(4), 343–372. https://doi.org/10.1016/S1364-0321(01)00003-X

Taghavi, M., & Lee, C.-J. (2024). Development of novel hydrogen liquefaction structures based on waste heat recovery in diffusion-absorption refrigeration and power generation units. Energy Conversion and Management, 302, 118056. https://doi.org/10.1016/j.enconman.2023.118056

Taghavi, M., Salarian, H., & Ghorbani, B. (2022). Economic Evaluation of a Hybrid Hydrogen Liquefaction System Utilizing Liquid Air Cold Recovery and Renewable Energies. Renewable Energy Research and Applications, Online First. https://doi.org/10.22044/rera.2022.11899.1122

Teichmann, D., Stark, K., Müller, K., Zöttl, G., Wasserscheid, P., & Arlt, W. (2012). Energy storage in residential and commercial buildings via Liquid Organic Hydrogen Carriers (LOHC). Energy & Environmental Science, 5(10), 9044. https://doi.org/10.1039/c2ee22070a

Yanxing, Z., Maoqiong, G., Yuan, Z., Xueqiang, D., & Jun, S. (2019). Thermodynamics analysis of hydrogen storage based on compressed gaseous hydrogen, liquid hydrogen and cryo-compressed hydrogen. International Journal of Hydrogen Energy, 44(31), 16833–16840. https://doi.org/10.1016/j.ijhydene.2019.04.207

Yildiz, A. (2016). Thermoeconomic analysis of diffusion absorption refrigeration systems. Applied Thermal Engineering, 99, 23–31. https://doi.org/10.1016/j.applthermaleng.2016.01.041

Yildiz, A., Ersöz, M. A., & Gözmen, B. (2014). Effect of insulation on the energy and exergy performances in Diffusion Absorption Refrigeration (DAR) systems. International Journal of Refrigeration, 44, 161–167. https://doi.org/10.1016/j.ijrefrig.2014.04.021

Yilmaz, C. (2018). A case study: Exergoeconomic analysis and genetic algorithm optimization of performance of a hydrogen liquefaction cycle assisted by geothermal absorption precooling cycle. Renewable Energy, 128, 68–80. https://doi.org/10.1016/j.renene.2018.05.063

Yilmaz, C., & Kaska, O. (2018). Performance analysis and optimization of a hydrogen liquefaction system assisted by geothermal absorption precooling refrigeration cycle. International Journal of Hydrogen Energy, 43(44), 20203–20213. https://doi.org/10.1016/j.ijhydene.2018.08.019

Zhang, F., Zhao, P., Niu, M., & Maddy, J. (2016). The survey of key technologies in hydrogen energy storage. International Journal of Hydrogen Energy, 41(33), 14535–14552. https://doi.org/10.1016/j.ijhydene.2016.05.293

Zhang, J., Fisher, T. S., Ramachandran, P. V., Gore, J. P., & Mudawar, I. (2005). A Review of Heat Transfer Issues in Hydrogen Storage Technologies. Journal of Heat Transfer, 127(12), 1391–1399. https://doi.org/10.1115/1.2098875

Zhang, S., Li, K., & Liu, G. (2023). An efficient hydrogen liquefaction process integrated with a solar power tower and absorption precooling system. Clean Technologies and Environmental Policy, 25(3), 1015–1041. https://doi.org/10.1007/s10098-022-02423-w

Zhang, Y., Campana, P. E., Lundblad, A., & Yan, J. (2017). Comparative study of hydrogen storage and battery storage in grid connected photovoltaic system: Storage sizing and rule-based operation. Applied Energy, 201, 397–411. https://doi.org/10.1016/j.apenergy.2017.03.123

Zhou, L. (2005). Progress and problems in hydrogen storage methods. Renewable and Sustainable Energy Reviews, 9(4), 395–408. https://doi.org/10.1016/j.rser.2004.05.005

Züttel, A., Remhof, A., Borgschulte, A., & Friedrichs, O. (2010). Hydrogen: The future energy carrier. Philosophical Transactions of the Royal Society A: Mathematical, Physical and Engineering Sciences, 368(1923), 3329–3342. https://doi.org/10.1098/rsta.2010.0113